On the Impact of Thermal Radiation and Turbulence on Drizzle Development

Mares Alexander Barekzai

Munich 2020

look outside

On the Impact of Thermal Radiation and Turbulence on Drizzle Development

Mares Alexander Barekzai

Dissertation
at the Faculty of Physics
Ludwig-Maximilians-University
Munich

submitted by
Mares Alexander Barekzai

Munich
13.09.2020

Primary Reviewer: Prof. Dr. Bernhard Mayer
Secondary Reviewer: Prof. Dr. George Craig
Primary Investigator: Prof. Dr. Harald Lesch
Secondary Investigator: Prof. Dr. Andreas Burkert
Date of Examination: 22.10.2020

Contents

Zusammenfassung

Obwohl die Qualität der Vorhersage von Regen große Fortschritte gemacht hat, so ist das Verständnis der Regenentwicklung noch lückenhaft. Auf mikrophysikalischer Ebene bilden sich die Tropfen an Aerosolen und wachsen über Diffusion von Wasserdampf. Nachdem die Tropfen eine gewisse Größe erreicht haben (schätzungsweise 20 μm), beginnen sie zu kollidieren und die Wachstumsrate beschleunigt sich stark. Auch wenn die numerische Beschreibung der Tropfenkollisionen noch eine Herausforderung darstellt, so ist man sich einig, dass diese das Tropfenwachstum stark beschleunigen und in kurzer Zeit Regentropfen entstehen lassen. Noch schlecht verstanden ist jedoch der Übergang dieser beiden Wachstumsprozesse. Die aktuellen Prozesse schaffen es nicht, die kurzen beobachteten Zeitskalen der Regenentwicklung zu reproduzieren. Das diffusive Wachstum verlangsamt sich derart, dass Tropfen über 15 μm nicht ausreichend und nicht in realistischen Zeitskalen enstehen. Um diese Lücke zu schließen, wird in dieser Arbeit mit einer, um thermische Abstrahlung erweiterten, Beschreibung des Diffusivenwachstums experimentiert. Die freiwerdende latente Wärme wird neben der Wärmediffusion auch über thermische Strahlung verteilt. In Kombination mit einer neuen Beschreibung von Turbulenz, welche die lokalen, nicht aufgelösten Schwankungen im Feuchtefeld für jeden Tropfen beschreibt, wurden einfache Luftpaket- und darauf aufbauend umfassendere Strömungs-Simulationen (LES) durchgeführt. Die verwendete Beschreibung des mikrophysikalischen Modells löst dabei die Orte und Bewegungen, sowie das diffusive Wachstum der Tropfenpopulation explizit auf. Die Ergebnisse der Luftpaketsimulationen zeigen, dass die Kühlung am Tropfen durch thermische Strahlung grössere Tropfen hervorbringt und dies auf kürzeren Zeitskalen. Das veränderte Wachstum kann hier zu einer leichten Untersättigung im Luftpaket führen, wodurch die kleinsten Tropfen zu verdunsten beginnen können. Dieser Effekt wird am deutlichsten in der Kombination mit Fluktuationen im Feuchtefeld. Auch wenn die Fluktuationen bereits alleine einen beschleunigenden Einfluss auf die Kollisionszeitskala haben, so ist die Beschleunigung am deutlichsten in der Kombination. Es werden mehr kleine Tropfen durch Feuchtefluktuationen erzeugt und diese verdunsten häufig in dem durch thermische Strahlung untersättigten Luftpaket. Die Sensitivitätsstudien zeigen, dass langsamere Aufwinde die Verbreiterung der Tropfenverteilung und die Beschleunigung des Kollisionsbeginns, durch thermische Strahlung und durch Feuchtefluktuationen, deutlich voran treiben. Der Einfluss der Aerosolverteilung hat den grössten Effekte für wenige und kleine Aerosole. Die LES Simulationen einer nächtlichen stratus Wolke zeigen, dass die Menge der kollisionsaktiven Tropfen an der Wolkenoberkante durch thermische Strahlung zunimmt. In besonderem Maße wirken sich Die Feuchteflukuationen führen zu einer Zunahme von größeren Tropfen an der Wolkenoberkante, aber auch an der Wolkenunterkante. In den LES Strömungs-Simulationen nimmt der Effekt durch die Kombination von thermischer Strahlung und Turbulenz ab, denn im Vergleich zu den Luftpaketsimulationen sind hier Feuchtefeld und Tropfenposition weniger stark gekoppelt. Die untersuchten mathematischen Beschreibungen tragen zum Schliessen der Lücke zwischen den Wachstumsprozessen bei. Für eine detailliertere Aussage, sollten diese aber mit expliziten Kollisionen auf diversen Wolkentypen untersucht werden.

Despite impressive advances in rain forecasts over the past decades, our understanding of rain formation on a microphysical scale is still poor. Droplet growth initially occurs through diffusion and, for sufficiently large radii, through the collision of droplets. However, there is no consensus on the mechanism to bridge between the two growth processes. The analysis of prior methods is extended by including Radiatively enhAnced Diffusional growth (RAD) to a Markovian turbulence parameterization. This addition increases the diffusional growth efficiency by allowing for emission and absorption of thermal radiation. Specifically, an upper estimate for the radiative effect is quantified by focusing on droplets close to the cloud boundary. The strength of the parcel model approach is that it determines growth rate dependencies on a number of parameters, like updraft speed and the radiative effect, in a deterministic way. Realistic calculations with a cloud resolving model are sensitive to parameter changes, which may cause completely different cloud realizations and thus it requires considerable computational power to obtain statistically significant results. The simulations suggest that the addition of radiative cooling can lead to a doubling of the standard deviation for the droplet size distributrion. However, the magnitude of the increase depends strongly on the broadening established by turbulence, due to an increase in the maximum droplet size, which accelerates the production of drizzle. Furthermore, the broadening caused by the combination of turbulence and thermal radiation is largest for small updrafts and the impact of radiation increases with time, which is most pronounced for slow synoptic updrafts.

The second part of the thesis treats more realistic and complex large eddy simulations (LES) conducted with the model PALM. LES resolve large laminar and turbulent motions and the associated mixing process of dry and wet air. The parametrizations of the unresolved subgrid scales (SGS) include the prognostic equation for the SGS kinetic energy, which is coupled to the investigated SGS Markovian turbulence parametrization. Furthermore, the superdroplet microphysics resolves the positions of the cloud droplets, including their individual sedimentation movements. Therefore, the evolution of water vapor and liquid water is decoupled in comparison to the parcel model simulations and as a result the impact of radiation decreases. The radiative heating rates are calculated for each model column independently. The simulations were initialized with atmospheric profiles from the first nocturnal measurements of the DYCOMS campaign. After a spin up period of 30 minutes the simulations show a stratocumulus cloud deck between 600 and 900 m. The statistical analysis of the clouds show that the drizzle water content increases due to both radiation and turbulence, with a larger contribution from turbulence. Turbulence also introduces a significant amount of drizzle water at the cloud bottom. In contrast, thermal radiation increases drizzle formation mainly at the cloud top. The impact of RAD on the amount of drizzle is similar to that of coupling radiative heating rates to the temperature field. The radiative impact increases slightly in combination with turbulence. Both, thermal radiation and turbulence speed up the production of drizzle and to verify that the gap between diffusional and collisional growth is bridged simulations with explicit droplet collisions should be compared to warm rain observations.

Chapter 1

Introduction

The Intergovernmental Panel on Climate Change IPCC (2013) considers the representation of clouds as the greatest source of uncertainty in current climate models. Furthermore, the World Economic Forum considers water scarcity as one of the 10 most pressing global problems, in their current Global Risk Report WEF (2019). Precipitation is the ultimate source of fresh water. Without rain, life as we know it, would not be possible. Those are only two international organizations pointing at the importance of expanding our understanding of clouds and the process of rain formation to improve the predictions of weather and climate models.

Two thirds of the earth's surface are covered with clouds. Clouds are made of condensed and/or frozen water and appear generally in rising air, which cools and saturates with respect to water. The transported water vapor and aerosols (e.g. sea salt, soot, dust particles) are essential to create clouds. In typical atmospheric conditions, water vapor condenses on aerosol particles, which lowers the necessary saturation pressure. Clouds can be distinguished in terms of shape, between sheet like, homogeneous stratus clouds and heap like, inhomogeneous cumulus clouds. Furthermore, the transitional regime between the two is termed: stratocumulus clouds. Stratus clouds are generally larger then cumulus clouds, with and extent of several hundred kilometers. They are easier to predict, compared to cumulus clouds, because they are generated from large scale motions, which are better represented in global models. Cumulus clouds, of a few hundred meters evolve according to the local, small scale atmospheric dynamics with large spatial and temporal variability. Finally, the frequent stratocumulus clouds evolve due to a mixture of small and large scale dynamics. Current climate models run on 100 km and weather models on 3 km resolution, both are far from capturing the small scales required to develop cumulus clouds. Furthermore, not only that the range of spatial scales limit the representation of clouds, but also the knowledge gaps in microphysical cloud processes. Even now, ice free clouds, that contain only liquid droplets, are not sufficiently well understood to represent the formation of rain with confidence.

Here we focus on the knowledge gap concerning the formation of rain in clouds, that do not contain ice. How do droplets become big enough to form rain like droplets of several mm? The current understanding of the growth mechanisms has the following shortcoming: the initial droplet growth by condensation becomes very slow, when the growth by collision has not started yet. This gap is called the Condensation-Collision Bottleneck and happens around a droplet radius of r$\sim$15 μm. We need to bridge this gap, in order to understand the formation of rain in realistic timescales. Several attempts have been made, including the role of giant aerosol particles, turbulence and radiation. Here, we investigate the combination of unresolved turbulence and thermal radiation and their impact on bridging the gap between the growth processes. Furthermore, a recently developed microphysics is applied, which resolves positions, motions and explicitly models the growth process for so called superdroplets. One superdroplet is representing several normal droplets of the same size. The research question of the current thesis can be formulated as:

Can thermal radiation in combination with unresolved turbulence explain the formation of rain in ice free clouds?

Thermal radiation and unresolved turbulence are two of the most promising candidates to complete the understanding of warm rain formation. To this end, two experimental setups, a simple parcel model and a complex Large Eddy Model are expanded by parametrizations for thermal radiation and turbulence and evaluated.

The following paragraph focuses on the parcel model approach, which is published in Barekzai and Mayer (2020).

Warm rain plays an important role for tropical precipitation (Hou et al., 2014; Lau and Wu, 2003; Liu and Zipser, 2009), but the precise processes that convert cloud droplets to rain are not well understood. The formation of warm rain begins with the condensation of water on Cloud Condensation Nuclei (CCN) to form haze droplets. If the environment reaches a critical saturation, the haze particle nucleates and grows freely by condensation. The droplets grow until they are sufficiently large to collide, at that point the collision and coalescence process dominates the growth and creates drizzle and eventually rain drops. Although there is agreement on these principal steps the details of drizzle formation remain an open question. Drizzle is defined as hydrometeors with a radius between 20 and 250 μm (Feingold et al., 1999; Hudson and Yum, 2001; Rasmussen et al., 2002) and its formation cannot be explained solely by diffusional growth and subsequent collisions (Illingworth, 1988; Beard and Ochs III, 1993; Laird et al., 2000). The classical diffusional growth process is proportional to the inverse of the droplet radius ($dr/dt \propto 1/r$) which results in very slow growth speeds for droplets larger than 15 μm. Collision is generally considered efficient for radii larger than 20 μm (Brenguier and Chaumat (2000)). Furthermore, diffusional growth decreases the standard deviation of the droplet size distribution, which slows down the onset of collisions by narrowing the fall speed spectrum. The classical approaches to growth by diffusion and collision are therefore insufficient to explain the formation of drizzle in realistic timescales and also to reproduce the observed, broad and multi-modal droplet

distributions (Warner, 1969a,b). The aforementioned problem is called "the Condensation Coalescence Bottleneck" (Brewster, 2015; Wang and Grabowski, 2009). Previous attempts to pass the bottleneck and simulate more realistic droplet distributions investigated the role of Giant Cloud Condensation Nuclei (GCCN) (Feingold et al., 1999; Houghton, 1938; Johnson, 1982; Yin et al., 2000), turbulence (Fouxon and Stepanov, 2002; Grabowski and Wang, 2013; Pinsky and Khain, 1997) and radiation (Brewster, 2015; Guzzi and Rizzi, 1980; Klinger et al., 2019; Lebo et al., 2008; Marquis and Harrington, 2005; Rasmussen et al., 2002; Roach, 1976). Here, the often underrepresented role of radiation in the diffusional growth process in combination with turbulence is highlighted. The key idea is that both heat diffusion and thermal radiation allow the droplet to dissipate latent heat released during condensation. Radiative cooling can reduce the temperature of the droplet below the temperature of the surrounding air. Consequently, droplets can continue to grow even in slightly subsaturated environments. This process will be referred to as the "Radiatively enhAnced Diffusional" growth (RAD), which is not considered in the classical diffusional growth theory and which is not included in the current microphysical parametrizations, despite being already proposed by Roach (1976). (Harrington et al., 2000; Hartman and Harrington, 2005a,b) investigated the impact of RAD on the formation of drizzle in arctic stratus clouds. They applied LES simulations and a Trajectory model to compare the effects of radiation using a bin microphysics. Radiative fog simulations have also been conducted as proposed in the fundamental paper of Roach (1976) (Brown and Roach, 1975; Duynkerke, 1991; Roach et al., 1976). Here, a parcel model with Lagrangian microphysics is used to investigate RAD in combination with turbulence induced saturation fluctuations, which can serve as a foundation for the interpretation of more elaborated LES simulations. The Lagrangian microphysics representation applies so-called superdroplets, each representing a group of droplets with the same aerosol properties throughout the parcel (Cooper et al., 2013; Shima et al., 2009; Vaillancourt et al., 2002). In contrast to passive tracers, the superdroplets nucleate and subsequently grow and shrink by interacting with the surrounding moisture field. The advantage of this approach is that it allows the explicit treatment of the growth by diffusion and the implementation of a turbulence parametrization, resulting in different growth histories for each superdroplet. The thermal radiative cooling is only relevant near the cloud edges, because at the cloud center the emitted radiation is in balance with the absorbed radiation. The distance from the cloud edges at which cooling is relevant depends on the liquid water content and ranges from 50 to 100 m (Klinger and Mayer (2016)). The implementation details of the parcel model are based on Grabowski and Abade (2017a). The current parcel model investigation can be understood as a continuation of that study.

In contrast to the parcel simulations, more realistic, yet complex simulations are done and presented in the Chapter 5 with the large eddy model PALM-LES. LES simulations solve the Navier-Stokes equations for the large, energy containing eddies and parametrize the smaller, subgrid scale (SGS) eddies. In contrast to the prescribed development of the parcel model, the LES develops its turbulent and dynamic state autonomously. Prescribed is only

the initial state of the atmosphere, by the temperature, pressure and humidity profiles. In the spin up period of approximately 20 minutes, the model develops its stationary state. In this section, the measurements from the first nocturnal research flight (RF01) of the Dynamics and Chemistry of Marine Stratocumulus field study (DYCOMS-II), presented in Stevens et al. (2005), are used to initialize the LES Model and as a result a warm stratus cloud develops.

The LES simulations are evaluated on a 3 dimensional grid. Therefore, the water vapor and water droplets change grid cells and are less tightly coupled, compared to the parcel simulations. Superdroplets change grid cells, due to sedimentation or turbulence and may leave the flow of air in which they were formed. Furthermore, the mixing process of dry and wet air, at the cloud bottom and top, is included in LES simulations, which further attenuates the connection between the water vapor and the condensed water. The mixing of dry and wet air is considered to be very important for the formation of rain, because droplets need to experience large supersaturations, in combination with only a low droplets concentration, to become rain. This condition is most likely found at the continuously evolving cloud edges.

Collision is the most potent droplet growth process and is known to effectively produce rain. However, collisions are difficult to parametrize and still considered experimental for the superdroplet microphysics. Droplets, that collide must be aware of their neighboring superdroplets and in the process of colliding, new superdroplet are created, which becomes computationally demanding. Therefore, the process of collisions is not included in this study. Instead, the focus lies on the production of smaller drizzle droplets, starting at a droplet radius of about 20 μm, which are known to initiate collisions. In LES simulations, radiation is evaluated at the grid layers for each column independently. This is called: independent column approximation, and neglects the influence of the other columns with the focus on the thermal spectral range.

Chapter 2

Scientific Background

2.1 The Atmosphere

The earth system may be split into three parts: atmosphere, ocean and land. All parts are coupled in a complex way. In the context of this thesis, only the atmosphere is explicitly considered and the coupling to the land surface is neglected. The ocean is considered by the initial conditions of the simulations, which are based on measurements from research flights over the ocean. The atmosphere is a gaseous shell around the planet. It is made up of approximately 78% N_2, 21% O_2 and 1% Argon. The surface continuously introduces aerosol particles into the atmosphere, which plays an important role in the formation of clouds (Andreae and Rosenfeld, 2008; Fan et al., 2016). In the context of this thesis, the considered aerosol is sea salt, which is introduced into the atmosphere by sea spray. Furthermore, the atmosphere contains water vapor as well as liquid and frozen water, in the form of so called warm, ice and mixed clouds.

A summarizing table of the variables and constants, used in the following chapters, can be found in the Tables (6.1) and (6.2).

The description of atmospheric gases starts with randomly moving molecules, idealized as point particles, which are interacting via elastic collisions. The resulting description is termed the ideal gas law:

$$\mathrm{p} = \rho \, \mathrm{R_d} \mathrm{T}. \tag{2.1}$$

The equation describes the state of an gas, e.g. air, as a function of the density ρ, pressure

p and temperature T. The specific gas constant R_d can be calculated with:

$$R_d = \frac{R}{M} = \frac{N_A}{k_B M_{air}}, \tag{2.2}$$

with the universal gas constant R, the Avogadro constant N_A and the molar mass of air M_{air}. The specific gas constant of air becomes: $R_d = 287$ J K^{-1} kg^{-1}.

The average temperature profile, for the well mixed lower atmosphere, can be approximated as linear decreasing from the surface temperature T_0.

$$T(z) = T_0 - z \cdot \Gamma_d \tag{2.3}$$

The slope is given by the dry atmospheric lapse rate, which can be calculated with $\Gamma_d = g/c_p = 9.8$ K km^{-1}. The decrease in temperature with height of dry air depends on the earth's gravitational acceleration $g = 9.81$ m s^{-2} and the specific heat $c_p = 1003.5$ J kg^{-1} K^{-1}. Similar, the atmospheric lapse rate for moist air can be approximated with $\Gamma_w \approx 5$ K km^{-1}. The value is approximated, because it depends on the temperature and on the amount of released latent energy by the condensed water.

The hydrostatic pressure profile is established by the gravitational force acting on the air, approximated as motionless, and serves as the reference state for the pressure deviations, calculated from atmospheric models:

$$\frac{dp}{dz} = -\rho\, g \tag{2.4}$$

The potential temperature Θ is a useful quantity, which is describing the temperature of a dry air parcel, that is brought adiabatically to a reference pressure level p_0 (usually 1000 hPa or the earth surface pressure). It allows to easily assess the stability of the atmosphere and is the preferred way to specify atmospheric temperature profiles.

$$\Theta = T \cdot \left(\frac{p_0}{p}\right)^{R_d/c_p} \tag{2.5}$$

Furthermore, the liquid water potential temperature Θ_l accounts for the temperature increase from condensation. The exact formulation can be found in Betts (1973), a simple approximation results to:

$$\Theta_l \approx \Theta - \frac{L_v}{c_p}\, q_c, \tag{2.6}$$

with the cloud water mixing ratio q_c, which is the fraction of water mass to air mass over the considered volume.

The water vapor in the atmosphere is the basis of all fresh water on earth and the microphysical processes, involved in the formation of clouds and eventually rain, are described in the following section.

2.2 Microphysics

The amount of water vapor, that air can hold depends on temperature and pressure. The excess water vapor changes state into liquid water or ice. The amount of water vapor to saturate the air, is described with the Clausius-Clapeyron relation Rogers and Yau (1996). It describes the phase transition from water vapor to liquid water, by providing the temperature dependence of the saturation water pressure:

$$\frac{de_s}{dT} = \frac{L_v \; e_s}{R_v \; T^2}. \tag{2.7}$$

The latent heat of vaporization for water is $L_v = 2.257 \cdot 10^6$ J kg^{-1} and the specific gas constant for water vapor is $R_v = 461$ J K^{-1} kg^{-1}. The solution of Eq. (2.7) for the saturation pressure e_s can be approximated with the August-Roche-Magnus formula Alduchov and Eskridge (1996) for typical atmospheric temperatures:

$$e_s(T) = 6.1094 \cdot \exp\left(\frac{17.625 \; T}{T + 243.04}\right). \tag{2.8}$$

T is the temperature in Celsius and e_s the saturation pressure in hPa. Finally, the saturation pressure translates to the saturation water vapor mixing ratio q_{vs}, by using the ideal gas law to:

$$q_{vs} = \frac{R_v}{R_d} \frac{e_s}{p - e_s} \tag{2.9}$$

Water vapor condenses to liquid water, if the water vapor mixing ratio q_v exceeds the saturation mixing ratio q_{vs}. The mixing ratio q_v describes the ratio of the water vapor mass to the respective air mass.

Two frequently used quantities to describe water in the atmosphere, are the liquid water content and liquid water path (lwc and lwp). Both are defined for a grid or parcel volume as:

$$\text{lwc} = \frac{4\pi}{3} \rho_w \int n(r) \, r^3 \, dr \quad \text{and} \quad \text{lwp} = \int \text{lwc} \, dz, \tag{2.10}$$

with the radius dependent droplet number concentration n(r).

The condensed water appears in the form of clouds. Clouds come in different shapes and are made of liquid and/or frozen water droplets/crystals. Clouds are especially hard to predict, because their evolution depends on a broad range of length scales, that can not be resolved in current weather models. However, the correct prediction of clouds has many applications. They range from the prediction of solar irradiance at the earth's surface for renewable energy production, the impact on earth's climate evolution to the forecast of rain in a world with growing deserts. The clouds microphysical structure and optical thickness, as well as, the height of the cloud top, determine their impact on the earth radiative energy budget. In summary, high clouds warm the atmosphere due to their lower temperature and, therefore, lower thermal radiative emission. Optically thick clouds, at all altitudes, cool the atmosphere, due to their contribution to an increased albedo, which is the ratio of reflected to total incoming solar radiation IPCC (2013) (Chapter 7 Clouds and Aerosols). In total, clouds are assumed to have a cooling effect on the climate, due to the optically thick and therefore reflective, low lying stratus clouds.

The principle steps of warm (ice free) cloud development, from a droplet perspective, are called: nucleation, condensation, collision and the final stage of sedimentation, resulting in evaporating drizzle or rain.

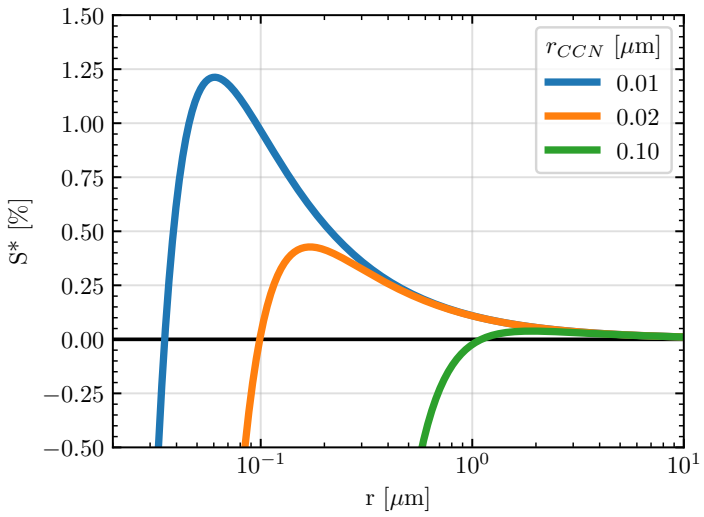

Figure 2.1: Köhler curves that show the equilibrium supersaturation S* at the droplet surface for NaCl aerosol particles of different radii r.

2.2.1 Nucleation

The first step, from water vapor to a cloud droplet, is called nucleation. Water vapor condenses at the aerosol surface and forms droplets. This is described by the Köhler process. The Köhler process is based on equilibrium thermodynamics and takes into account: the increase of saturation pressure at the droplet surface, due to the curvature of the droplet, which is called the Kelvin-Effect, and the decrease of saturation pressure, due to the mixing and dissolution of aerosol in the droplets, which is called the Raoult-Effect. The first order approximation of the resulting equations, from Rogers and Yau (1996), has the form $S^* = \frac{e}{e_s} - 1 = \frac{C_K}{r} - \frac{C_R}{r^3}$ and will be explained in Section 3.1.1. The Figure 2.1 shows the Köhler relation for different sea salt aerosols, with respect to the equilibrium supersaturation at the droplet surface. For typical atmospheric conditions, aerosols are needed to form droplets. Without aerosols, the needed saturation pressure would not be reached, which is due to the Kelvin Effect (Curvature Effect). A cloud droplet nucleates, when the environment surpasses the critical supersaturation S_{cr}, allowing the droplet to grow beyond the critical radius r_{cr} see Eq. (3.6). The critical values describe the maximum in the Köhler curve, shown in Fig. 2.1. Before the nucleation, the droplet does not grow freely, the size is determined by the saturation of the droplet environment. After surpassing r_{cr}, the droplet grows freely, as long as, the droplet environment is supersaturated.

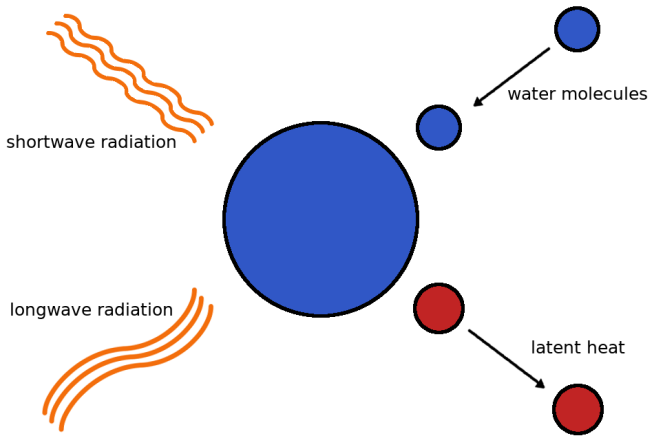

Figure 2.2: Sketch of diffusional growth. At the center is the droplet, which exchanges water molecules (blue circles) and latent heat (red circles) by diffusion with the environment, and that interacts with long and short wave radiation, which are indicated on the left side, by the short and long waves.

2.2.2 Diffusional Growth

Eq. (2.11) describes the classical diffusional growth of the droplet, which is deduced from Maxwell (1890). From the processes of water and heat diffusion, one arrives at the following equation for the droplet radius:

$$\frac{dr}{dt} = \frac{1}{A\rho_w}\left(\frac{S^*}{r}\right) \quad \text{with:} \quad \frac{A}{\rho_w} = \frac{L_v^2}{R_v T^2 \kappa} + \frac{R_v T}{e_s D_w}, \tag{2.11}$$

with the thermal conductivity of air $\kappa = 0.0243$ W m^{-1} K^{-1} and the diffusion constant of water vapor in air $D_w = 2.82 \cdot 10^{-5}$ m^2 s^{-1}.

The parameter $A = \left(\frac{L_v^2}{R_v T^2 \kappa} + \frac{R_v T}{e_s D_w}\right)$ is approximated under the assumption that $L_v/(R_v T) \gg 1$. The analytical solution of Equation (2.11), given in Rogers and Yau (1996), results in:

$$r(t) = \sqrt{\frac{2S^*}{A\rho_w} t} \tag{2.12}$$

In section 3.1.1, the radiative augmented diffusional growth (RAD) is presented, which builds upon Eq. (2.11) and is a fundamental part of this thesis.

2.2.3 Condensation-Coalescence Bottleneck

The formation of rain in warm clouds and in realistic timescales can not be explained by diffusional growth alone. It slows down significantly and it takes too long to reach droplets with radius of 15 micron, due to the square root dependence of time in Eq. (2.12). Another efficient growth mechanism, known to form rain very rapidly, is collision and coalescence between droplets. The simplest approach to collisions is the gravitational kernel method, presented by Hall (1980). It describes the probability of two colliding droplets with radii r and r$'$ as:

$$K(r, r') = \pi\ (r + r')^2\ E(r, r')\ \|v(r) - v(r')\|. \tag{2.13}$$

It is proportional to the difference in terminal fall velocity v(r), which increases with the differences in the droplet radii. $E(r, r')$ are the experimental radius dependent collision efficiencies. However, collisions become effective after some of the droplets reach the size of drizzle droplets (approximately 20 microns). This can not be reached in realistic atmospherical conditions, by sole classical diffusional growth, according to Eq. (2.11). Furthermore, collisions are not yet accurately implemented in the current Lagrangian microphysical approach Shima et al. (2009) and as a consequence: they are not included in this thesis. Therefore, we focus on the formation of drizzle droplets by diffusional growth, alone. Drizzle is expected to initiate collisions, if present in sufficiently large quantities. The current

challenge in warm cloud physics is to find and describe the processes, that bridge the bottleneck for droplets, with radius between 15 and 20 microns. Possible processes to bridge the bottleneck are unresolved scales of turbulence and their impact on saturation (Wang and Grabowski, 2009; Grabowski and Abade, 2017b), as well as, collisions Franklin et al. (2005), details about the aerosol distribution (giant aerosol particles) Feingold et al. (1999) and radiation Barekzai and Mayer (2020). Here, the focus is on saturation fluctuations due to turbulence, radiation and the combination of both processes.

2.3 Radiation

The dynamical processes on earth are fueled by energy from the sun and this energy is distributed over the atmosphere. Atmospheric radiative transport models describe the distribution of energy and in order to understand it, one has to learn the basics of radiation.

Our current understanding of light is fundamentally based on the work of Maxwell (1996) and Einstein (1905). Electromagnetic radiation propagates like a wave, but it interacts like a particle. The discrete particle nature of light is called quantum of light or photon. The energy E_ν of a photon, is proportional to its frequency ν, from the corresponding wave, it is associated with:

$$\mathrm{E}_\nu = \mathrm{h}\nu, \tag{2.14}$$

with Planck's constant $\mathrm{h} = 6.626 \cdot 10^{-34}$ J s. The wavelength λ can be derived from the frequency of light ν with $\mathrm{c} = \lambda/\nu$, where c is the universal speed of light. Furthermore, light can be described by frequency, direction of propagation and polarization.

Two fundamental quantities to describe the radiative transfer in the atmosphere are called irradiance and radiance. Both can be defined in terms of the radiant flux $\Phi_\mathrm{e} = \mathrm{dQ/dt}$, which is the radiative energy Q per unit time. The irradiance $\mathrm{E_e}$ is the radiative flux per unit area.

$$\mathrm{E_e} = \frac{\mathrm{d}\Phi_\mathrm{e}}{\mathrm{dA}}\ [\mathrm{Wm^{-2}}] \tag{2.15}$$

The radiance L is the radiative flux per solid angle per projected area:

$$\mathrm{L_e} = \frac{\mathrm{d}^2\Phi}{\cos\theta\,\mathrm{dA}\,\mathrm{d}\Omega}\ [\mathrm{Wm^{-2}sr^{-1}}], \tag{2.16}$$

with the differential of the solid angle as $\mathrm{d}\Omega = \sin\theta\,\mathrm{d}\theta\,\mathrm{d}\Phi$.

To describe the radiance emitted from a thermal source, the concept of a black body is introduced by Planck (1901). A black body absorbs all incoming radiation. Radiation

from a black body is in thermal equilibrium and as a result the photon statistics is only temperature dependent, as described by Planck's law:

$$\mathcal{B}(\lambda, \mathrm{T}) = \frac{2\mathrm{hc}^2}{\lambda^5} \frac{1}{\exp\left(\frac{\mathrm{hc}}{\lambda \mathrm{k_B T}}\right) - 1}. \tag{2.17}$$

The integral over the wavelength and the solid angle of the Planck's law is called the Stefan-Boltzmann law (2.18). It describes the radiative power per surface area of a black body, which is proportional to the fourth order in temperature:

$$\mathrm{P/A} = \sigma\, \mathrm{T}^4, \tag{2.18}$$

with $\sigma = \frac{2\pi^5 \mathrm{k_B^4}}{15\mathrm{c}^2\mathrm{h}^3}$. For real bodies Eq. (2.18) is modified by the bodies effectiveness of emission, the emissivity ϵ.

2.3.1 Emission, Absorption and Scattering

A way to think about light in terms of a photon is: that at some point, the photon gets emitted and absorbed by matter and, in between, the direction of propagation may be changed by scattering. The thermal emission of a source depends on the temperature. It is different, depending on the effectiveness of the material, the so called emissivity ϵ of the material. Kirchhoffs law (2.19) states, that at thermal equilibrium and for all wavelengths of light, the emissivity ϵ_λ equals the absorptivity α_λ for every object. In other words, the effectiveness of emission equals the effectiveness of absorption. The reference absorption comes from the idea of a black body, which absorbs and reemits all incoming radiation, corresponding to a maximal absorptivity of 1.

$$\epsilon_\lambda = \alpha_\lambda \tag{2.19}$$

The change in the direction of light, by scattering, happens with a certain probability, which is modeled for a single scattering particle, by the scattering cross section σ_{sca} and for several scattering particles, which will be present in the atmosphere, with the scattering coefficient β_{sca}:

$$\beta_{\mathrm{sca}}(\mathrm{r}) = \int_0^\infty \mathrm{n(r)}\, \sigma_{\mathrm{sca}}(\mathrm{r}) \mathrm{dr}. \tag{2.20}$$

Light is also absorbed with a certain probability, which is described by the absorption cross section $\sigma_{\mathrm{abs}}(\mathrm{r})$ or the absorption coefficient β_{abs}. For atmospheric absorption, the

integration over all atmospheric constituents is used:

$$\beta_{\text{abs}} = \int_0^\infty \text{n(r)}\, \sigma_{\text{abs}}(\text{r})\, \text{dr}. \tag{2.21}$$

The extinction is the sum of absorption and scattering:

$$\beta_{\text{ext}} = \beta_{\text{abs}} + \beta\text{sca}. \tag{2.22}$$

The cross sections, σ_{sca} and σ_{abs}, are measures for the probability of scattering or absorption of light. They can be calculated by assuming a spherical charge distribution of the target. This is called Mie theory Mie (1908). In the limit of small wavelengths, compared to the droplet size $\lambda < \text{r}$, the geometrical approximation of $\sigma(\text{r}) = 2\pi\text{r}^2$ for the scattering cross section, can be used. This is valid for short wave radiation and for long wave radiation, absorption dominates the propagation.

2.3.2 Radiative Transfer Equation

A simple approximation of the radiative transfer approach, is the Beer-Lambert-Bouguer law (Beer, 1852; Lambert, 1760; Bouguer, 1729), which describes the extinction of radiance in a medium, along its path:

$$\frac{\text{dL}_\text{e}}{\text{ds}} = -\beta_{\text{ext}}\, \text{L}_\text{e} \qquad \text{L}_\text{e}(\text{z}) = \text{L}_\text{e}(0) \exp\left(-\int_0^\text{s} \beta_{\text{ext}}\, \text{ds}\right) = \text{L}_\text{e}(0) \exp\left(-\tau\right), \tag{2.23}$$

with the optical thickness τ. The full radiative transfer equation (RTE) describes the emission, scattering and absorption of light in a medium. This integro-differential equation was introduced by Cha (1950) and has no analytical solution:

$$\frac{\text{dL}_\text{e}}{\text{ds}} = -\beta_{\text{ext}}\, \text{L}_\text{e} \;+\; \frac{\beta_{\text{sca}}}{4\pi} \int_{4\pi} \mathcal{P}_\text{e}(\Omega' \to \Omega)\, \text{L}_\text{e}(\Omega')\, \text{d}\Omega' \;+\; \beta_{\text{abs}} \mathcal{B}(\text{T}). \tag{2.24}$$

It contains, in addition to the Beer-Lambert-Bouguer term, the scattering term with the probability $\mathcal{P}_\text{e}$, that a photon is scattered from all directions Ω' into the direction Ω of propagation, and, finally, the thermal emission term according to Planck's law (2.17). Solving the RTE in the atmosphere allows to estimate the net radiative fluxes at the droplet surface and from that the impact of radiation on the droplet and cloud evolution can be investigated.

Schwarzschild Approximation

The Schwarzschild approximation to the radiative transport equation (2.24) neglects the scattering of light. This is a good approximation in the thermal spectral range, where photons are absorbed with high probability from the atmosphere, which is reflected in large values for σ_{abs}. Therefore, the scattering term with the integral of the RTE can be neglected and the resulting Eq. (2.25) becomes analytically solvable (2.26)

$$\frac{\mathrm{dL_e}}{\mathrm{ds}} = -\beta_{\mathrm{abs}}\,\mathrm{L_e} \;+\; \beta_{\mathrm{abs}}\,\mathcal{B}(\mathrm{T}) \tag{2.25}$$

The Schwarzschild approximation gives accurate results in the thermal spectral range, even though the scattering is large. If the absorption coefficient is large enough, the scattering coefficient can be neglected. The analytical solution of Eq. (2.25) becomes:

$$\mathrm{L_e}(\tau) = \mathrm{L_e}\,\exp\left(-\tau\right) + \mathcal{B}\,\left(1 - \exp\left(-\tau\right)\right) \tag{2.26}$$

2.4 Turbulence

Turbulent motions, in addition to the general motion of air, lead to local fluctuations in the temperature and the water vapor field. This is strongest for vertical velocity fluctuations, which is, in general, the direction in which the temperature and water vapor field change the most rapidly. Therefore, cloud droplets experience local, fluctuating saturation conditions and these small scale turbulent motions are not resolved in current weather models.

The general idea is that: Energy inserted at large length scales into the atmosphere turns into circular moving air, called eddies. Over time, the eddies decay into smaller eddies, which is transporting the kinetic energy to smaller scales. This part of the eddy spectrum is called the inertial subrange. The transport continues until viscosity dominates the evolution and the kinetic energy dissipates into heat. The smallest scales of turbulent motion are termed the dissipation range or Kolmogorov range. The characteristics of the energy transport, the energy cascade is visualized in Fig. 2.3.

Fig. 2.3 pictures the subgrid scale (SGS) cut-off. Small scale Eddies, below that cut-off, are not resolved by LES simulations but parametrized using a subgrid scale (SGS) turbulence scheme. The problem, of describing the unresolved scales in a model, that only resolves larger scales, in the context of the Navier-Stoked Equation, is called turbulence closure. The first LES simulations were run by (Deardorff, 1973, 1974). LES simulations can be applied to turbulent flows with large Reynolds numbers with the basic idea, that the larger motions of the flow contain the major part of the energy, therefore, smaller eddies can be neglected.

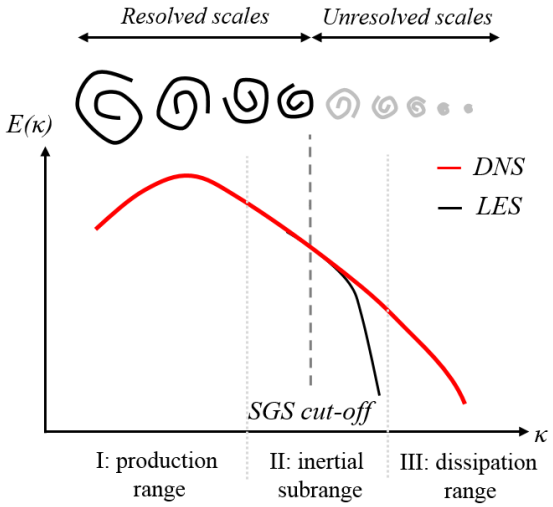

Figure 2.3: Turbulent energy spectrum, representing the kinetic energy production, inertial, and dissipation ranges. The figure is based on Ouro (2017)

2.4.1 Navier-Stokes Equation

The Navier-Stokes equations (2.27) are the fundamental equations in fluid dynamics and LES modeling. They describe the motion of a viscous fluid. It is basically Newton's second law of motion applied to continuous media. The solution is the flow velocity field in form of a vector field, that describes the direction and velocity of the flow at any point in time and space. For an incompressible fluid the Navier-Stokes equations are:

$$\rho \frac{\mathrm{D}\vec{\mathrm{u}}}{\mathrm{Dt}} = -\nabla \mathrm{p} + \mu \nabla^2 \vec{\mathrm{u}} + \rho \vec{\mathrm{g}} - 2\vec{\Omega} \times \vec{\mathrm{u}} \qquad \nabla \vec{\mathrm{u}} = 0, \tag{2.27}$$

where $\vec{\mathrm{u}}$ is the velocity field, which is divergence free, for an incompressible fluid. μ is the viscosity of the fluid and $\vec{\Omega}$ is the earth angular velocity vector.

2.4.2 Boussinesq Approximation

The Boussinesq approximation is used to simplify the Navier-Stokes equation for convective motions in the atmosphere. Density differences are ignored, except in terms concerning the gravitational acceleration. Therefore, are traveling density waves, like sound waves, not possible. Density and pressure are approximated as constant values with fluctuations (2.28).

$$\rho = \overline{\rho} + \overline{\rho}\,\alpha\,\Delta \mathrm{T} \qquad \mathrm{p} = \mathrm{p}_0 + \mathrm{p}' \tag{2.28}$$

The Boussinesq approximation cancels the hydrostatic terms from Eq. (2.4) and simplifies the Navier-Stokes Equation to:

$$\overline{\rho}\,\frac{\mathrm{D}\vec{\mathrm{u}}}{\mathrm{D}\mathrm{t}} = -\nabla \mathrm{p}' + \mu\Delta^2\vec{\mathrm{u}} - \overline{\rho}\vec{\mathrm{g}}\,\alpha\Delta\mathrm{T} - 2\,\vec{\Omega}\times\vec{\mathrm{u}}. \tag{2.29}$$

In a LES model, the separation between resolved and SGS scales is achieved by averaging over the governing equations, according to the discrete Cartesian grid Schumann (1975). The filtering length for the Navier-Stokes equation is the grid spacing used in the computations, which moves the viscosity term into the subgrid model. The resulting Navier-Stokes equations describe the dynamics of grid size eddies.

Chapter 3

Methods

In order to test the importance of radiation on the formation of rain and compare it to the effect of unresolved turbulence, numerical models have been written, selected, configured and expanded. In the following, the parcel model is presented, which is written in Python, and the PALM LES is briefly described. The LES is provided by the PALM group at the University of Hannover and selected, due to its sophisticated Lagrangian microphysics and expanded, by the Tenstream library Jakub and Mayer (2015), which is providing the radiation solver. The solver is coupled to the diffusional droplet growth implementation.

The following section, about the parcel model, is published in Barekzai and Mayer (2020).

3.1 Parcel Model

The parcel model equations for temperature (T), water vapor mixing ratio (q_v) and the pressure (p) are implemented according to (Grabowski and Abade, 2017a; Grabowski and Wang, 2009; Grabowski et al., 2011):

$$c_p \frac{dT}{dt} = -gw - L_v \frac{dq_\nu}{dt} \tag{3.1}$$

$$\frac{dp}{dt} = -\rho_0 wg \tag{3.2}$$

(see Table 6.1 for the notations used throughout the equations and text). The temperature of the parcel decreases moist adiabatically as the parcel ascends due to the coupling to the latent heat of condensation (Eq. 3.1). A constant density of air is assumed with ρ_0=1 kg m^{-3}, according to the approximation of small vertical displacement ($\sim$ 1 km). The initial conditions are T=281.7 K, p=89880 Pa and q_v=0.0077 kg kg^{-1}, which result in a relative humidity of ϕ=99%. Accordingly, the ascending parcel will rapidly begin with the development of a cloud.

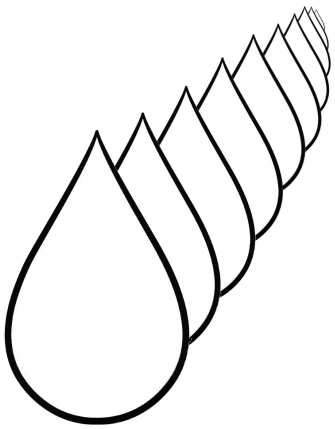

Figure 3.1: Sketch of the superdroplet parametrization, where one representative Superdroplet stands for a group of equally sized ordinary droplets

3.1.1 Microphysics

Here, the superdroplet approach is used in the context of warm clouds (Andrejczuk et al., 2008; Shima et al., 2009). It is based on Lagrangian particles, which carry information about the aerosol type in the dry radius (r_{dry}), chemical composition defaulted here to sodium chloride, droplet size after nucleation and multiplicity factor. The multiplicity factor N_i is the represented number concentration of aerosols, and after nucleation, of droplets by a superdroplet. The multiplicity factors were chosen to be the same for all superdroplets and constant over time with $N_i=10^3$ m^{-3} and can therefore be seen as a scaling factor for the liquid water mixing ratio. The maximal possible number of nucleated superdroplets is set to $N_{sd}=10^5$ m^{-3} with a total CCN number density of $n_{CCN}=100$ cm^{-3}. The droplet size starts at the dry radius and diverges after nucleation due to diffusional growth. The superdroplets grow only by condensation and the combined condensation rates of all nucleated superdroplets can be written as:

$$\frac{dq_\nu}{dt} = -\frac{d}{dt}\sum_i \frac{4}{3}\pi r_i^3 N_i \frac{\rho_w}{\rho_0} \tag{3.3}$$

The advantage of the superdroplet approach is the combination of a global representation of distributed cloud droplets with the local, explicit treatment of nucleation and diffusional growth processes.

Nucleation

The dry radius is sampled from two log-normal distributions with mean radii of 20 and 75 nm and geometric standard deviations of 1.4 and 1.6. The relative concentrations of 60

and 40 % correspond to CCN number concentrations of n_{20}=60 cm^{-3} and n_{75}=40 cm^{-3}, if n_{ccn}=100 cm^{-3} (from Grabowski and Abade (2017a)). The aerosol size information and chemical composition determine the critical supersaturation (S_{cr}) that must be reached to nucleate the corresponding aerosol. The nucleated superdroplets start to grow freely from the critical radius (r_{cr}), which are obtained by calculating the maximum of the Koehler equation (Rogers and Yau (1996))

$$S^*_{eq} = \frac{C_K}{r} - \frac{C_R}{r^3}. \tag{3.4}$$

The critical supersaturation and radius are:

$$r_{cr} = \min\left(\left(\frac{3C_R}{C_K}\right)^{1/2}, 1\mu m\right) \qquad S_{cr} = \left(\frac{4C_K}{27C_R}\right)^{1/2} \tag{3.5}$$

with the corresponding parameters:

$$C_K = \frac{2\gamma M_w}{R_V T \rho_w} \qquad C_R = \frac{2r^3_{dry}\rho_{NaCl}M_w}{\rho_w M_{NaCl}} \tag{3.6}$$

Critical radii larger than 1 μm are cut off to eliminate the impact of the aerosol distribution tail on the evolution of the droplet population. This condition allows us to isolate the effect of radiation from possible Giant Cloud Cloud Condensation Nuclei (GCCN). The resulting cut off value is a rough estimate of the average droplet embryo size after one model time step.

Diffusional Growth

After the nucleation process, the droplets begin to grow by diffusion. Classical diffusional growth considers the diffusion of water molecules and latent heat to and from the droplet. Both processes come together in the diffusion Eq.:

$$\frac{dr_i}{dt} = \frac{1}{A\rho_w}\left(\frac{S^*}{r_i}\right) \tag{3.7}$$

The subscript i denotes the i-th superdroplet. Equation (3.7) was extended by Roach (1976) to include the emission and absorption of radiation. It becomes the Radiatively enhAnced Diffusional (RAD) growth equation:

$$\frac{dr_i}{dt} = \frac{1}{A\rho_w}\left(\frac{S^*}{r_i} - D\mathcal{R}\right). \tag{3.8}$$

The parameter $\mathcal{R}$ is the radiative power per droplet surface area, defined as the difference of absorbed and emitted power. Positive $\mathcal{R}$ indicate radiative heating of the droplet and negative values indicate cooling. Equation (3.8) is obtained with the approximation of

$\frac{L_v}{R_v \cdot T} \gg 1$ and contains the temperature-dependent parameters $A = \left(\frac{L_v^2}{R_v \kappa T^2} + \frac{R_v T}{D_w e_s} \right)$ and $D = \frac{L_v}{R_v \kappa T^2}$.
An individual droplet grows with decreasing speed as it increases in size, proportional to 1/r from Eq. (3.7). This statement still holds for RAD growth if $\frac{S^*}{r} > -D\mathcal{R}$ with small droplets and large supersaturations. The differences compared to the classical diffusional growth can be seen in the asymptotic:

$$\lim_{r \to \infty} \left. \frac{dr}{dt} \right|_{classic} = 0 \tag{3.9}$$

$$\lim_{r \to \infty} \left. \frac{dr}{dt} \right|_{enhanced} = \frac{-D\mathcal{R}}{A \rho_w}. \tag{3.10}$$

Large droplet radii under classical diffusional growth show zero growth speed (Eq. (3.9)), in contrast to RAD growth, which converges to a term proportional to $\mathcal{R}$ (Eq. (3.10)). The behavior now strongly depends on the sign of $\mathcal{R}$. If only thermal radiation is considered, $\mathcal{R}$ becomes negative, and therefore large droplets continue to grow (except close to the lower cloud boundary). The additional cooling due to the emission of thermal radiation lowers the temperature of the droplet compared to the environment, effectively reducing the saturation vapor pressure at the droplet surface. For completeness it should be mentioned that thermal radiation causes considerable cooling at the cloud top and moderate warming at the cloud base. Here, the focus is on the cloud top.
It is known that the standard deviation of the droplet size distribution will decrease, because smaller droplets grow faster and catch up with larger drops under classical diffusional growth. The addition of radiative cooling to the diffusional growth is expected to cause more complex behavior: The standard deviation of the distribution will initially decrease, until the parcel becomes subsaturated. Subsequently, the subsaturated parcel will contain large droplets, which continue to grow and small droplets which start to evaporate. The radius, which separates growing from shrinking droplets is calculated with dr/dt=0 from Eq. (3.8):

$$r_{sep} = \frac{S^*}{D\mathcal{R}}. \tag{3.11}$$

Therefore, the standard deviation of the droplet distribution increases due to thermal radiation (Harrington et al., 2000; Hartman and Harrington, 2005a,b). Finally, some droplets will completely evaporate, which again decreases the standard deviation. Figure 3.2 shows the dependence of the droplet growth speed on the radius, according to Equation (3.8) with and without the radiative term. The gray lines show the solution for the droplet growth speed, under constant super or subsaturated conditions. The left panel, without radiation, shows that the growth (I) (evaporation (II)) is fastest for small droplets and symmetric with respect to dr/dt=0. The right panel, with thermal radiation, adds a third growth regime (III) in which the environment is subsaturated, but the droplets keep growing, particularly, with large droplets that grow faster than smaller ones. The zero crossings of the

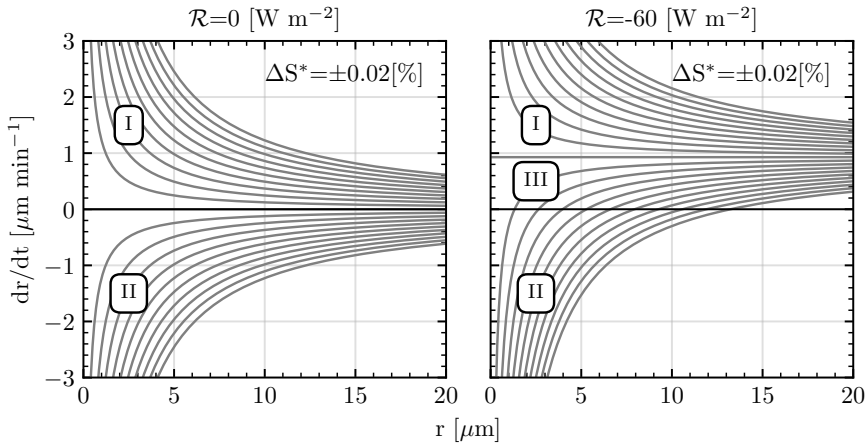

Figure 3.2: The two panels show the droplet growth speed evaluated for the RAD growth equation (Eq. 3.8). On the left, the radiative term is set to zero and on the right, according to Equation 3.14 (with f=1/6 and T=282 K from the American Standard Atmosphere at 1 km). The isosaturation lines are centered around S^*=0 and 10 times incremented and decremented by $\Delta S^* \pm 0.02$ %. The Greek numbers I, II and III indicate different droplet growth regimes: The small droplets I) grow faster, II) evaporate faster, III) grow slower than the large droplets.

isosaturation lines indicate below which radius and subsaturation the droplets evaporate. The diffusional growth equation is evaluated for a model time step of 0.2 s with the Euler forward schema.

3.1.2 Radiation

The additional term in Eq. (3.8) contains the net radiative power per droplet surface area ($\mathcal{R}$). This term could comprise solar and thermal contributions. Here, the focus is on thermal radiation only, which can be thought of as a nocturnal setting. It was shown in Roach (1976) that $\mathcal{R}$ can be directly calculated from the radiative fluxes. In particular, Eq. (11) of Roach (1976) shows that $\mathcal{R}$ is directly related to differences of the actinic flux or "average intensity" $F_{act} = \int_{4\pi} I(\lambda) d\Omega$ and the black body emission:

$$\mathcal{R} = Q_a(r) \left[\frac{1}{4} F_{act} - \sigma_{sb} T^4 \right] \tag{3.12}$$

where $Q_a(r)$ is the absorption efficiency, weighted with the spectral actinic flux and averaged over wavelength. $Q_a(r)$ is typically close to 1 for the droplet sizes under consideration. Roach (1976) further showed that the actinic flux can be approximated by the sum of the upward (E_{up}) and downward fluxes (E_{dn}) ($F_{\downarrow}$ and -$F_{\uparrow}$, in the notation of Roach (1976) where the upward component is actually negative):

$$F_{act} \approx 2 \cdot (E_{dn} + E_{up}) \tag{3.13}$$

For the parcel model the effect of radiation close to the cloud top is estimated. In the following, it is shown that the heating rate at cloud top can simply be approximated by:

$$\mathcal{R} \approx -\mathrm{f} \cdot \sigma_{\mathrm{sb}} \mathrm{T}^4. \tag{3.14}$$

It is assumed that $\mathrm{T}_{\mathrm{drop}} \approx \mathrm{T}$, because Marquis and Harrington (2005) estimated that the difference between droplet and environment temperature is $\Delta \mathrm{T} \leq 1$ K for droplets with $\mathrm{r} \leq 200$ μm and a maximum of of 3 K is reached for $\mathrm{r} \geq 1000$ μm. In the simulations, droplet radii are well below 1000 micron and show only small temperature differences. The radiative factor (f) allows for a first and simple approximation of the surrounding atmosphere and the geometry of the parcel. f=1 would describe a parcel in vacuum. For a parcel at cloud top, f reduces to 1/2, because the downward emitted radiation is balanced by the upward emitted radiation from the droplets below. Finally, only the atmospheric window regions contribute to the cooling, which adds a factor of 1/3 for shallow cumulus cloud tops. In summary, this yields f=1/6.
To check the validity of f, the actinic flux is calculated for a number of typical atmospheric profiles: pressure, temperature, water vapor, other trace gases (Anderson et al., 1986) and cloud top heights (Fig. 3.3). $\mathcal{R}$ was calculated following (3.12). More specifically, rather than using the approximated $\mathrm{Q_a(r)}$, the integral over wavelength

$$\mathcal{R} = \int \mathrm{Q_a}(\lambda) \left[\frac{1}{4} \mathrm{F_{act}}(\lambda) - \pi \mathrm{B}(\lambda, \mathrm{T}) \right] \mathrm{d}\lambda, \tag{3.15}$$

where $\mathrm{B}(\lambda, \mathrm{T})$ is the Planck function, is used. The corresponding simulations were done with the radiative transport library libRadtran (Mayer and Kylling, 2005; Emde et al., 2016) using the correlated-k distribution by Fu and Liou (1992) for the molecular absorption and assuming an optically thick cloud with an effective droplet radius of 10 μm. Cloud optical properties were calculated by Mie theory (Mie (1908)). Figure 3.3 illustrates that f=1/6 is a valid approximation for shallow cumulus clouds with top heights of approximately 2 km. f clearly depends on the amount of water vapor above the cloud: For the mid-latitude summer and tropical atmospheres with high temperature and absolute humidity f is considerably smaller than for the dry sub-arctic winter and mid-latitude winter atmospheres with low temperatures, which is due to the higher atmospheric transmission for less water vapor. For the same reason f increases with increasing cloud top height until it reaches values slightly above 0.5. For the following simulations f=1/6 is used, if not stated otherwise. This approach allows us to investigate the underlying mechanisms in a idealized way, which will serve as a interpretation basis for more elaborated LES simulations.

3.1.3 Turbulence

The turbulence parametrization is based on the work of Grabowski and Abade (2017a) and references therein, and will only be briefly summarized here. The aforementioned

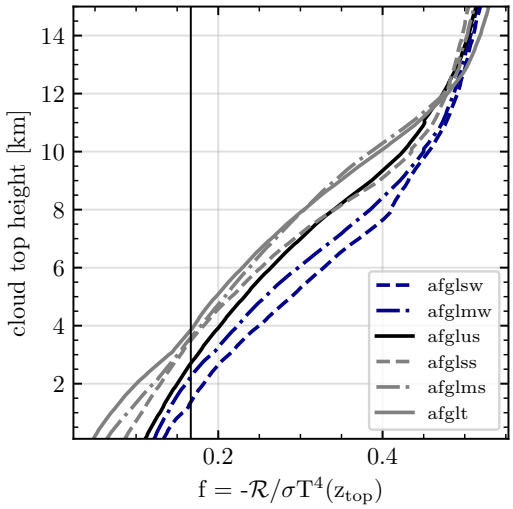

Figure 3.3: Estimation of the cloud top height dependence of f (Eq. 3.14) for an optically thick cloud and a number of typical atmospheric profiles: U.S. standard atmosphere (afglus), subarctic winter (afglsw), midlatitude winter (afglmw), subarctic summer (afglss), midlatitude summer (afglms), tropical (afglt). The vertical black line marks the reference value of f=1/6.

paper describes saturation fluctuations for isotropic homogeneous turbulence, which are implemented for each superdroplet. The evolution for the saturation fluctuations ($S_i^{*\prime}$) is given by:

$$\frac{dS_i^{*\prime}}{dt} = a_1 w_i' - \frac{S_i^{*\prime}}{\tau_{relax}} \tag{3.16}$$

The equation uses the phase relaxation time scale (τ_{relax}) from Squires (1952), which is describes the time scale the droplet distribution needs to remove the excess saturation. The fluctuations of the vertical velocity field (w_i') are described by the Gaussian stationary process (Ornstein-Uhlenbeck process):

$$w_i'(t+dt) = w_i'(t)\exp\left(-\frac{dt}{\tau}\right) + \sqrt{1-\exp\left(-\frac{2dt}{\tau}\right)}\sqrt{\frac{2}{3}E}\cdot\chi \tag{3.17}$$

The solution of the random process depends only on the standard normal distributed random variable (χ), the turbulent kinetic energy ($E(\epsilon, L)$) and the integrated turbulent timescale ($\tau(\epsilon, L)$) (Schumann, 1991; Lasher-Trapp et al., 2005). The last two quantities can be formulated as functions of the dissipation rate ϵ=50 cm^2 s^{-3} and the length scale of the adiabatic parcel L=50 m. The values for L and ϵ correspond to an adiabatic core of a cumulus cloud and are taken from the predecessor studies of (Grabowski and Abade, 2017a; Jonas, 1996; Lasher-Trapp et al., 2005). For a direct comparison between the two studies these values are adopted. Furthermore, the impact of thermal radiation should be largest at cloud edges, therefore simulations with ϵ=10 cm^2 s^{-3} are included, which is a

estimate for the turbulent dissipation rate at the stratocumulus cloud top (Moeng et al. (1996)).

3.2 Large Eddy Model

Additionally, to the parcel model, the PALM LES model from Maronga et al. (2015) is used to investigate the impact of thermal radiation and saturation fluctuations from unresolved turbulence, on the formation of drizzle. The impact is analysed with a model, that resolves the large scale dynamics of clouds. PALM solves the non-hydrostatic, incompressible Boussinesq-Approximation of the Navier-Stokes equation. Furthermore, the prognostic equations for water vapor mixing ratio, potential temperature and subgrid scale kinetic energy are solved.

3.2.1 Microphysics

In order to test for the sensitivities of radiation and saturation fluctuations on drizzle formation, the Lagrangian Cloud Model (LCM) Hoffmann et al. (2017) is expanded by the enhanced diffusion Eq. (3.8) and coupled to the Schwarzschild radiation solver Grant (2004), with saturation fluctuations from Grabowski and Abade (2017b). The superdroplets for the LES model follow the same implementation as for the parcel model, except of the following distinctions:

Superdroplets are randomly initialized, each grid cell initially contains the same number of superdroplets, which are placed at random locations inside the cell. This was not needed in the parcel model, due to the lack of spatial dimensions.

Droplet nucleation is neglected, instead droplets grow freely by diffusion according to Eq. (3.8) and, depending on the environmental conditions, from a minimal radius of $r_0 = 10^{-8}$ μm, which is the same for all droplets.

Initially, droplets grow according to the analytical diffusional growth equation (2.12), until they reached a size of 1 micron. This is done to eliminate errors, due to the stiffness of the diffusional growth equation.

Potential drizzle droplets are split, as proposed in Schwenkel et al. (2018), to improve the representation of large and therefore rare droplets. Superdroplets with radii larger then 15 μm, which have a multiplicity larger then $N_i \cdot 0.03$, are split into two separate superdroplets for each time step, with each superdroplet representing half of the ancestor multiplicity. The additional superdroplet is randomly located in the same grid box, within a radius of 1/n around the parent superdroplet location. n is the droplet number concentration in the

corresponding grid cell. As a result, superdroplets may be split in total 64 times, when growing into a drizzle droplet. The splitting parameters are set to balance the improvement in resolution with the numerical cost of increasing the superdroplet number.

3.2.2 Radiation

In contrast to the parcel simulations, which use a black body approach to parametrize radiation, the PALM LES simulations are coupled to the Tenstream library from Jakub and Mayer (2015) and run with the provided Schwarzschild solver. The resulting distributed thermal radiative energy is then separated into an atmospheric and a cloud part. Finally, the absorbed and emitted radiative energy at the cloud is distributed over the droplets.

Schwarzschild Approximation

The Schwarzschild approximation to the radiative transport equation (2.24) neglects the scattering of light. From the solution (2.26) of the radiance, the upwards and downwards irradiance are calculated, by integrating over several zenith angles θ, which appear as $\mu_\theta = \cos(\theta)$. The zenith integration of Eq. (3.18) is done with 10 sample points for each orientation.

$$\mathrm{E_{up}} = \int_0^{2\pi} \mathrm{d}\phi \int_0^1 \mu_\theta \, \mathrm{L_e}(+\mu_\theta, \phi) \, \mathrm{d}\mu_\theta \qquad \mathrm{E_{dn}} = \int_0^{2\pi} \mathrm{d}\phi \int_0^1 \mu_\theta \, \mathrm{L_e}(-\mu_\theta, \phi) \, \mathrm{d}\mu_\theta \tag{3.18}$$

It is numerically efficient to calculate the radiances according to (2.26). From that, the spectrally integrated heating rates can be calculated, using the net irradiance from each LES grid layer $\mathrm{E_{net}} = \mathrm{E_{dn}} - \mathrm{E_{up}}$, with:

$$\frac{\mathrm{dT}}{\mathrm{dt}} = -\frac{1}{\rho \mathrm{c_p}} \nabla \mathrm{E_{net}} = -\frac{1}{\rho \mathrm{c_p}} \frac{\mathrm{E_{net}}(\mathrm{z} + \Delta \mathrm{z}) - \mathrm{E_{net}}(\mathrm{z})}{\Delta \mathrm{z}} \tag{3.19}$$

In the last step, the equation simplifies due to the discrete layer nature of the LES models. The boundary conditions for the Schwarzschild solver and thermal radiation are: no incoming radiation from the top of atmosphere (toa), but black body radiation from the bottom, according to the earth surface temperature. There are other approaches to solve Eq. (2.24), which include the scattering term, but those are more numerically expensive. In case of solar radiation, scattering becomes important and the Schwarzschild approach is not a valid approximation anymore. If the experiment features approximately one dimensional stratus clouds, the discrete ordinate approach may be a good starting point. It is developed and applied by Cha (1950) and Liou (1973) and includes the scattering term in the RTE.

The spectral integration of the thermal radiation and the calculation of the optical properties is done according to the correlated-k method, presented in Fu and Liou (1992). The implementation from the radiative transfer model RRTMG is used and presented in Clough et al. (2005). In contrast to the numerically expensive line by line calculations, the correlated-k approach requires less sample points to integrate the spectrum of light and is therefore more computationally more efficient.

Furthermore, the resulting radiative flux divergence ∇E_{net} is separated into two parts, due to the atmospheric gasses and due to the cloud droplets: $\nabla E_{net} = \nabla E_{atm} + \nabla E_{cld}$. The net radiative flux at the droplet surface, for each individual cloud droplet $\mathcal{R}$ from Eq. (3.8), is calculated by distributing the radiative power in the grid box $\nabla E_{cld} \cdot V_{grid}$ over the droplets. Finally, the power for each droplet has to be distributed over the respective droplet surface.

$$\mathcal{R} = \nabla E_{cld} V_{grid} \cdot \frac{r_i^2}{\sum r^2} \frac{1}{4\pi r_i^2} = \frac{1}{4\pi} \frac{\nabla E_{cld} V_{grid}}{\sum r^2} \tag{3.20}$$

3.2.3 Turbulence

A LES like PALM solves the filtered Navier-Stokes equations. A detailed description of PALM can be found in Maronga et al. (2015). Additional, so called covariance terms arise in the filtered of the equations. The covariance terms are calculated with a subgrid scale (SGS) model. The problem is called turbulence closure. PALM runs the 1.5-oder closure with modifications, according to Deardorff (1980) and Moeng and Wyngaard (1988). The SGS model explicitly calculates the SGS kinetic energy, which is plugged into Eq. (3.17) to generate the vertical velocity fluctuations. Those are used to calculate the saturation fluctuations with Eq. (3.16). The prognostic equation for the SGS kinetic energy can be found in Maronga et al. (2015) in Eq. (16). Otherwise, the implementation of the saturation fluctuations follows the parcel model section 3.1.3.

3.2.4 Statistics

The evaluation of the LES time series data assumes a Gaussian distribution. The mean $\langle X \rangle$ values and the standard deviation σ_{sam} of the mean, for each time point, are calculated according to:

$$\langle X \rangle = \frac{1}{N_{ens}} \sum_{i=1}^{N_{ens}} X_i \qquad \sigma_{sam}^2 = \frac{1}{N_{ens}} \sum_{i=1}^{N_{ens}} (X_i - \langle X \rangle)^2 \tag{3.21}$$

If sums or differences of random values are calculated, the variances are added or subtracted, according to: $\langle \mathrm{X} - \mathrm{Y} \rangle \propto \mathcal{N}(\mu_\mathrm{X} - \mu_\mathrm{Y}, \sigma_\mathrm{X}^2 + \sigma_\mathrm{Y}^2)$. X and Y are placeholders for any atmospheric quantities.

The RMS values are calculated for the time period between 55 and 60 minutes, according to:

$$\mathrm{RMS} = \sqrt{\langle (\mathrm{X} - \mathrm{X}_\mathrm{ref})^2 \rangle_\mathrm{t}}, \tag{3.22}$$

with X_ref as the result for the reference simulation.

Chapter 4

Parcel Simulations

This chapter contains the results of the parcel model simulations. The idea of the parcel model is to keep the setup as simple as possible. It describes a single rising volume of air, with constant updraft velocity. The turbulent motions of air are included only indirectly in the saturation fluctuation parametrization from Eq. 3.16. As the initially dry parcel of air rises, droplets nucleate and grow into a population of droplets. The following results show how the development of the droplet population, especially the development of drizzle, depends on the saturation fluctuations and the thermal radiative cooling at the droplet. The parametrizations are called T and RAD in the following figures. Furthermore, several sensitivity studies are carried out with respect to the updraft speed of the parcel, the strength of the radiative cooling at the droplet and the aerosol background of the simulations. The results of the parcel simulations chapter are published in Barekzai and Mayer (2020).

4.1 Results

First, it is emphasized, that this study is a theoretical one. The nature of parcel models allows only for a limited range of scales and processes to be included. However, the parcel model reduces complexity and therefore improves the understanding of the individual processes, which might be concealed in a chaotic LES simulation. A important idealization is the neglection of cloud edge mixing, which may be included in the statistics of the saturation fluctuations in future studies. A first approach to include the process of mixing is shown in Abade et al. (2018). Furthermore, the sensitivity studies show a range in parameter space that extends beyond the values found in nature.

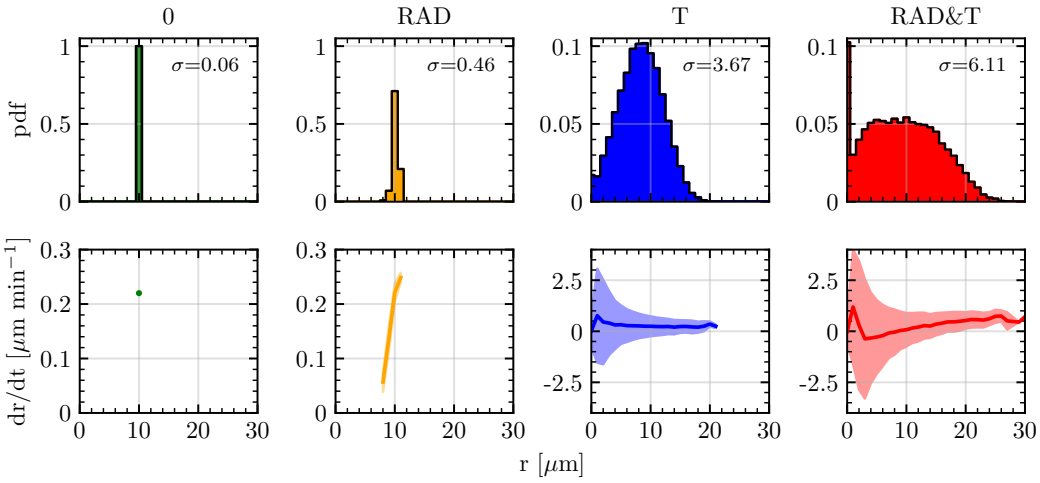

Figure 4.1: The droplet size distributions (upper panels) and corresponding mean growth speeds (lower panels), evaluated 15 min after the onset of condensation. The simulations are run with w=0.1 m s^{-1}, f=1/6 and ϵ=10 cm^2 s^{-3}. A bin-size of 1 μm centered around integer values was applied. The shaded area marks two standard deviations around the mean growth speed. The colors and labels represent: (green, 0): the reference simulation without radiation or turbulence, (yellow, RAD): the reference simulation including radiation, (blue, T): the reference simulation including turbulence and (red, RAD&T): the combination of radiation and turbulence. σ is the standard deviation of the droplet distribution.

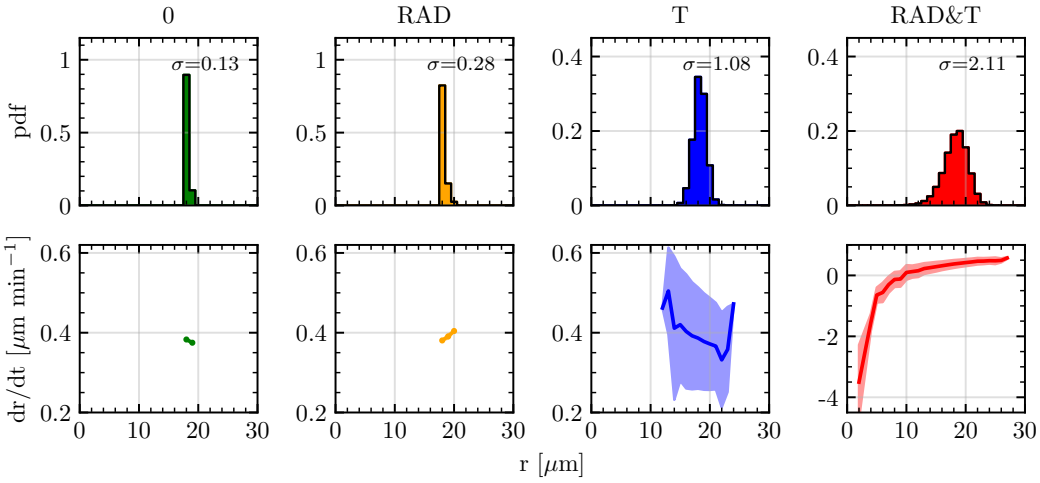

Figure 4.2: The simulations are run with w=1 m s^{-1}, f=1/6 and ϵ=50 cm^2 s^{-3} (see Fig. 4.1 for more informations).

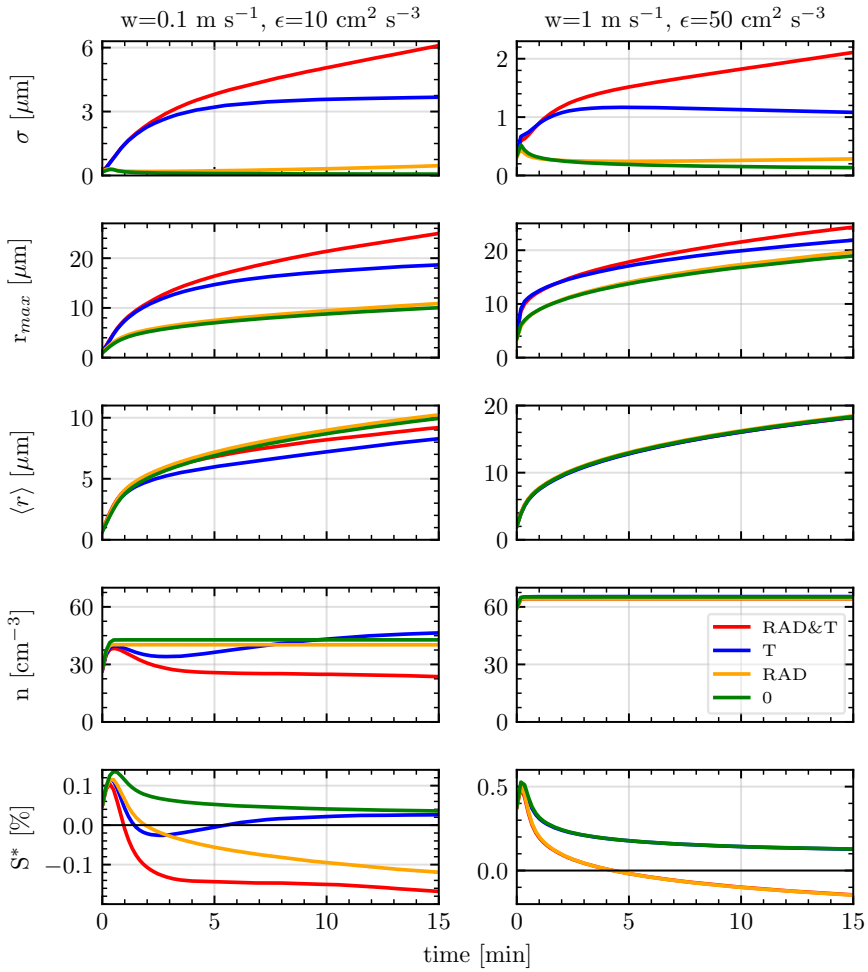

Figure 4.3: The time series of several parcel model quantities, from the onset of condensation until 15 min. The simulations are run with w=0.1 m s^{-1}, f=1/6, ϵ=10 cm^2 s^{-3} on the left panel and w=1 m s^{-1}, f=1/6, ϵ=50 cm^2 s^{-3} on the right panel. Shown are the standard deviation (σ), the mean radius of the largest droplets (r$_{max}$) (representing a number density of n$_{max}$=0.1 cm^{-3}), the mean radius ($\langle$r$\rangle$) and the supersaturation (S*). The label and color convention is the same as in the Figure 4.1.

4.1.1 Distributions and Time Series

In this section, the temporal development of the droplet distribution is compared for different parcel model setups. The first one, for a cloud edge environment, is w=1 m s^{-1}, ϵ=50 cm^2 s^{-3}, L=50 m and f=1/6, which is also used by Grabowski and Abade (2017a) and allows us to validate the results and to directly compare the impact of thermal radiation in combination with turbulence. The second one, for a cloud edge environment, is w=0.1 m s^{-1}, ϵ=10 cm^2 s^{-3}, L=50 and f=1/6. Here, the turbulent dissipation rate is taken from Moeng et al. (1996) for a stratocumulus cloud top. Furthermore, the updraft is an order of magnitude smaller. If not stated otherwise the figures have the following conventions for labels and colors: The base case applies classical diffusional growth (0, green), the turbulent parcel is identical to the setup of Grabowski and Abade (2017a) (T, blue), the simulations with radiation only (RAD, yellow) and the combination of turbulence and radiation (RAD&T, red). The histograms in Figure 4.1 and 4.2 are evaluated 15 min after the onset of condensation. The first two droplet size histograms, which evolved under classical diffusional growth or RAD (green or yellow) show sharply peaked distributions centered around radii that decrease with decreasing updraft, due to less adiabatic cooling. The standard deviation of the droplet size distribution, σ, is small and the sole addition of radiation introduces just a small amount of spread into the droplet distribution (σ<0.5 μm). The spreading is caused by the subsaturated environment, due to radiative cooling, which happens earlier for the w=0.1 m s^{-1} than for the w=1 m s^{-1} case, as can be seen in the S* panel of Fig. 4.3.

The droplet growth in a subsaturated environment changes the radius dependence of droplet growth: When classical diffusional growth in a supersaturated environment is considered, smaller droplets grow faster and catch up with larger ones, due to the 1/r dependence of Equation 3.7 (regime I in Figure 3.2). However, in a subsaturated environment, smaller droplets evaporate faster than larger droplets (regime II in Fig. 3.2). Finally, the addition of thermal radiation introduces a third growth regime with subsaturated environment, where smaller droplets grow slower than larger droplets, which causes σ to increase (regime III in Fig. 3.2). The earlier and the longer the parcel is subsaturated, the larger the increase in σ. Therefore, the radiation only simulation (yellow) with w=0.1 m s^{-1} produces larger σ values than the w=1 m s^{-1} simulations. The difference in σ is small, because the evaporation in regime II has not yet started. The two histograms on the right (blue and red) allow to estimate the impact of radiation added on top of turbulence. The histogram with turbulence (blue) shows the increase of σ due to turbulence alone, which evolves according to the balance between the spread introduced by saturation fluctuations and the narrowing of the droplet spectrum due to classical diffusional growth. The saturation fluctuations show a larger effect for small droplets, which can be seen in the diverging isosaturation lines in the regimes I and II of Figure 3.2. Therefore, the simulations with low updraft (w=0.1 m s^{-1}) show a larger spread in the droplet size distribution, despite of having a lower turbulent dissipation rate (ϵ=10 cm^2 s^{-3}). The red histograms combine the impact of turbulence with thermal radiation and show that larger

vertical motions produce larger supersaturations, which will produce larger droplets and is less sensitive to turbulence or radiation ($\sigma\sim2$ μm). In contrast, radiation with turbulence is most effective in the low updraft environment and substantially broadens the standard deviation. The addition of radiation to the simulations approximately doubles the droplet size standard deviation. Furthermore, the droplet size distribution is symmetric for w=1 m s^{-1}, in contrast to the w=0.1 m s^{-1}, where droplets are more likely to de-activate, resulting in a asymmetric droplet size distribution. The broadening of the droplet distribution is critical for the initiation of collision because a narrow droplet size spectrum also has a narrow fall-speed spectrum. Since differences in fall-speed are required to initiate the collection process, narrow spectra tend to suppress collisions.

Figure 4.3 shows the time series for the standard deviation (σ), the maximal radius (r_{max}), the mean radius ($\langle r \rangle$), the droplet number concentration (n) and the saturation (S*) of the environment. The maximal radius r_{max} is defined as the mean radius over the largest droplets

$$r_{max} = \frac{1}{n_{max}} \int_{r_0}^{\infty} r\ n(r) dr \tag{4.1}$$

where r_0 is chosen by the condition $\int_{r_0}^{\infty} n(r)dr \stackrel{!}{=} n_{max}$ with n_{max}=0.1 cm^{-3}. This is similar to the approach of (Feingold and Chuang, 2002; Feingold et al., 1999), who propose that a drizzle number concentration of $n_{drizzle}$=10^{-3} cm^{-3} of droplets with radii larger then 20 μm is required for drizzling and eventually raining parcels. A more cautious value for n_{max} is chosen to increase the number of droplets representing the tail of the droplet distribution, which would otherwise lead to strong noise. The standard deviation initially increases due to the nucleation of droplets and then develops according to the applied parametrizations. The subsequent narrowing due to the classical diffusional growth (green and yellow) is followed by broadening due to a subsaturated environment (yellow only). The resulting σ are small ($<$ 1 μm) for all updrafts, because the spread introduced by nucleation, which increases with increasing w, is reduced by the narrowing diffusional growth (regime I in Fig. 3.2). In this case, thermal radiation is acting only on narrow distributions, therefore the differential growth is weak. However, the simulations with turbulence (blue and red) show a larger increase in the standard deviation after nucleation. The time series confirms that turbulence introduces spread most effectively at the beginning of the simulations, when droplets are small. The reason is that the growth of small droplets is more sensitive to saturation fluctuations, which is shown by the diverging growth speeds in Fig. 3.2 for small radii. Consequently, turbulence has a larger impact for small updrafts. Although, after 15 min, the mean droplet size is only about 10 microns for w=0.1 m s^{-1} compared to 18 microns for w=1 m s^{-1} (a consequence of the adiabatic growth assumption), the standard deviation of the size distribution is a factor of 3 larger with lower updraft. Additionally, thermal radiation (red line) complements the turbulent growth by subsaturating the environment, which further supports the growth of large droplets. For both cases, the standard deviation of the droplet size distribution approximately doubles after 15 min,

when radiation is added. Therefore, the largest standard deviations are found for w=0.1 m s^{-1} simulations with the combination of turbulence and radiation. The maximum radius is introduced as a measure for the tail of the distribution, because it may harbor the rain droplet candidates, also known as embryonic drizzle from Hobbs and Rangno (1998). For the base and radiation simulations (green and yellow), the maximum radius r_{max} is similar to the mean radius, because the distribution is sharply peaked and r_{max} is close to $\langle r \rangle$. The turbulent simulations (blue and red) reach similar values for r_{max} after 15 min, for both updraft cases although the mean radius is different by a factor of 2.
The mean radius ($\langle r \rangle$) and the droplet number concentration (n) depend on the updraft and are hardly affected by radiation or turbulence in the w=1 m s^{-1} case. For the low updraft simulations (w=0.1 m s^{-1}), this is only true for the base and radiation only simulations (green and yellow). After nucleation, turbulence causes the evaporation of droplets due to negative saturation fluctuations and leaves the droplets with positive saturation fluctuations. This bias initially subsaturates the environment. However, after a few minutes the environment saturates again, due to additional sign switches of the saturation fluctuations, which remove the bias from the distribution and $S^{*'}$ becomes equally distributed. Simultaneously, small droplets nucleate, which lowers $\langle r \rangle$. The combination of radiation and turbulence (red) is similar in the development, but shows less renucleation of small droplets due to initially negative saturation fluctuations (number concentration in 4.3). The environment stays subsaturated, due to thermal radiation and therefore the critical saturation needed for renucleation is only rarely reached. However, the mean radius decreases, due to the evaporation of droplets at the benefit of a few large ones, which was also found in Guzzi and Rizzi (1980).

4.1.2 Sensitivity to the Radiation Factor

In this section, f is increased from 0 to 1 and investigate the impact on the droplet size distribution. Values for f larger than 0.5, that are not reached in the atmosphere are shaded gray. For estimates of possible f values see the Figure 3.3. The results are shown for simulations with w=1 m s^{-1}, ϵ=50 cm^2 s^{-3} (solid lines) and w=0.1 m s^{-1}, ϵ=10 cm^2 s^{-3} (dotted lines) in Fig. 4.4. The vertical black lines indicate the value f=1/6, which is used in the previous sections for the distributions and time series results. The general impact of higher radiation factors is that the subsaturation of the environment increases and therefore the separation radius becomes larger, which increases σ and r_{max} of the droplet population and decreases the droplet number concentration. All simulations show a decreasing droplet number concentration with increasing f. The droplet number concentration decreases stronger for simulations with turbulence (red) and starts at lower values for simulations with lower w. Therefore, all simulations show increasing mean radii with increasing f. Only the simulations with w=1 m s^{-1} and without turbulence (solid yellow) show a decreasing mean, because small droplets are introduced by passing r_{sep}, but complete evaporation has not yet started. The impact of passing r_{sep} is strongest for sharply peaked droplet distributions with a large number of droplets at once below r_{sep}. σ and r_{max} increase strongly with increasing f, as expected.

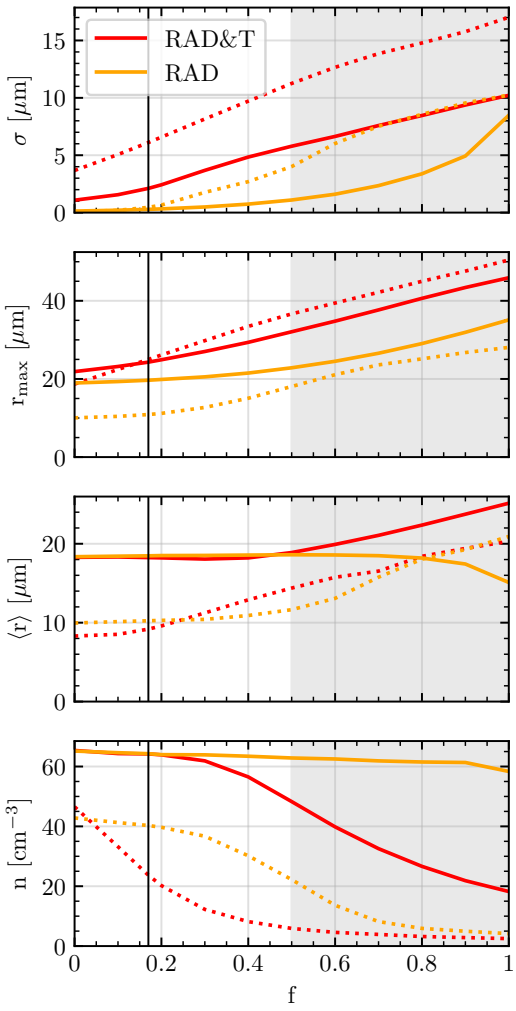

Figure 4.4: A sensitivity study with respect to the radiative factor. The simulations are evaluated after 15 min. The colors and labels represent the combination of radiation and turbulence (red, RAD&T) and the reference simulations including radiation (yellow, RAD). The solid and dotted lines show updraft speeds of 1 and 0.1 m s^{-1} with ϵ=50 cm^2 s^{-3} or ϵ=10 cm^2 s^{-3} if the simulations include turbulence. Additionally, the gray shaded area indicate f values that are not present in the atmosphere. For more information see the caption of Figure 4.5.

4.1.3 Sensitivity to the Updraft Speed

Updraft speeds are varied between 0.01 and 1.5 m s^{-1}, which correspond to slow (synoptic) and shallow convective vertical motions. The simulations are evaluated 15 min after nucleation and result in clouds with vertical extents varying between 10 and 1250 m. Figure 4.5 shows the standard deviation, the maximum radius, the mean radius and the droplet number concentration. The shaded regions (blue and red) connect the range of turbulent dissipation rates from 10 to 50 cm^2 s^{-3}. The two black vertical lines at w=0.1 m s^{-1} and w=1 m s^{-1} highlight the setups for which the time series and histograms were already shown in the previous section. The simulations with classical diffusion only (green) show a small increase of σ with increasing updraft, due to a increasing spread introduced by nucleation. The simulations with radiation (yellow) approximately double the spread from nucleation by subsaturating the environment and entering regime III (Fig. 3.2). For low updrafts, the spread increases stronger, due to evaporating droplets, which are below the separation radius (Eq. 3.11). Nonetheless, the standard deviations for simulations without turbulence are small (< 0.1 μm). For simulations with turbulence (blue and red) the standard deviations are larger ($\sigma \in (1,6)$ μm) and increase with decreasing updrafts. The impact of turbulence and thermal radiation on σ for lower updrafts increases due to diverging growth rates for small droplets.
For the simulations without turbulence (green and yellow), the updraft dependence of the maximum radius is determined by the increase of adiabatic cooling with increasing updraft. r_{max} is nearly identical to $\langle r \rangle$, because the distributions are sharply peaked. The simulations with turbulence only (blue) show larger values of r_{max} with strongest impact for low updrafts, if compared to the base simulations (green). It also reveals an intermediate w range, where w-dependence of r_{max} shows a minimum. The minimum is caused by an increasing r_{max} at high updrafts due to increasing adiabatic cooling, which increases $\langle r \rangle$. However, σ is largest at low updrafts, therefore, r_{max} shows a minimum at intermediate updrafts. The same can be found for the combination of turbulence and radiation (red), resulting in standard deviations of approximately 22.5 μm. The mean radius is determined by adiabatic cooling for simulations with w $>$ 0.5 m s^{-1}. For w $<$ 0.5 m s^{-1}, slightly smaller $\langle r \rangle$ appear in turbulent simulations (blue and red) ($\Delta\langle r \rangle < 2$ μm). The reason is, that the droplets start to evaporate right after nucleation followed by a period of secondary nucleation, which lowers the mean by introducing small droplets into the population. The combination of turbulence and thermal radiation (red) is similar to turbulence only (blue) but with less secondary nucleation due to the subsaturated environment. Furthermore, the parcel with radiation continues to evaporate droplets over time, which also introduces smaller droplets into the population that lower the mean. Additionally, the initial droplet number concentration increases with larger updrafts, according to higher reached peak saturations in the nucleation process. The dependence on the turbulent dissipation rate (blue and red shaded regions) shows smaller impact on σ and r_{max} then the impact of adding radiation (T and RAD&T).

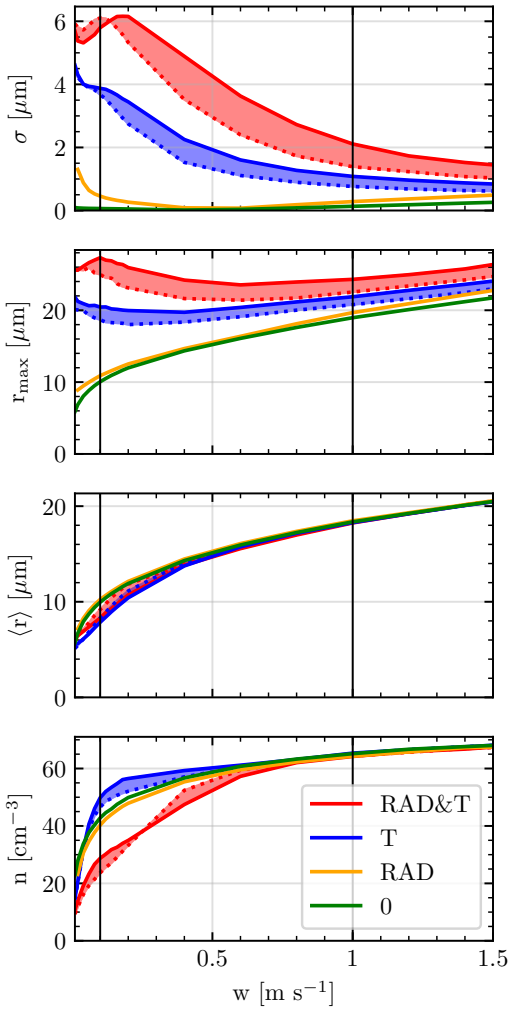

Figure 4.5: A sensitivity study with respect to the updraft velocity. The simulations are evaluated 15 min after condensation onset. Shown are the standard deviation (σ), the mean radius of the largest droplets (r_{max}) (representing a number density of n_{max}=0.1 cm^{-3}), the mean radius ($\langle r \rangle$) and the droplet number density n. The colors and labels represent: (green, 0): the reference simulation without radiation or turbulence, (yellow, RAD): the reference simulation including radiation, (blue, T): the reference simulation including turbulence and (red, RAD&T): the combination of radiation and turbulence. For simulations with turbulence, two dissipation rates are shown: ϵ=50 cm^2 s^{-3} and ϵ=10 cm^2 s^{-3} (solid and dotted lines). Additionally, the blue and red shaded regions mark intermediate values of ϵ. The vertical black lines at w=0.1 m s^{-1} and w=1 m s^{-1} indicate where distributions and time series are evaluated.

4.1.4 Sensitivity to the Simulation Time

Figure 4.6 compares clouds with the same vertical extent of 100 m, which develop under different updraft conditions ranging from w=0.01 m s^{-1} to 1.5 m s^{-1} and therefore in different time intervals (1 to 160 min). For w > 0.5 m s^{-1}, all simulations are approximately parametrization independent and the observed increase in σ and r_{max} with increasing w for simulations without turbulence is due to the increasing spread introduced by nucleation. Additionally, simulations with turbulence shift σ and r_{max} to larger values (< 1μm). For w < 0.5 m s^{-1}, the behavior is influenced by turbulence and radiation and the impact increases with simulation time and therefore decreasing w. The base simulations (green) show less nucleated droplets due to a smaller peak supersaturations reached in the process of nucleation. Therefore, $\langle r \rangle$ and r_{max} increase, because the condensed water is shared among less droplets. The simulations with radiation only (yellow) are similar to the base simulations except for long simulation times corresponding to w <0.2 m s^{-1}, where $\langle r \rangle$, r_{max} and σ strongly increase. The reason is that many droplets from the initially sharply peaked droplet distribution fall at the same time below the separation radius (Eq. 3.11) and start to evaporate until they eventually denucleate (regime III). The turbulent simulations (blue) increase in σ and r_{max} with simulation time. The droplet number concentration does not drop as low as for the base simulations, because droplets with positive saturation fluctuations keep nucleating over time, resulting in an approximately constant mean radius. For simulations with the combination of turbulence and radiation (red) the increasing impact of radiation on σ and r_{max} happens earlier compared to radiation only simulations (yellow), because droplets smaller then the separation radius are introduced early on from saturation fluctuations. The droplet number concentration is smaller then for the base simulations (green) because the droplets that nucleate do not grow in the subsaturated environment. Therefore, thermal radiation acts as an secondary nucleation inhibitor. The shaded regions which indicate dissipation rates between ϵ=10 and 50 cm^2 s^{-3} (blue and red) show only a small impact. Most notably, the standard deviation is reduces, but with a decreasing impact at low updrafts.

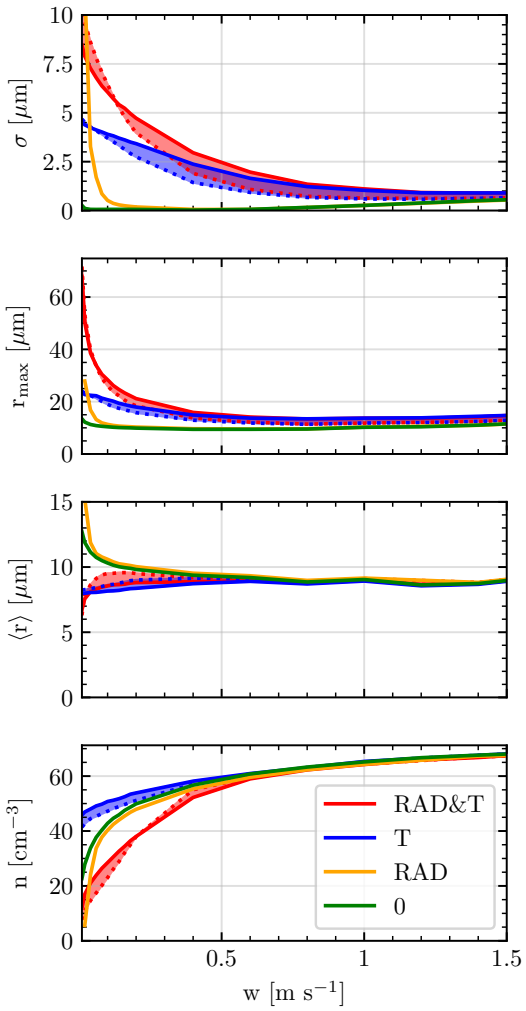

Figure 4.6: The simulations were evaluation after the clouds reached a vertical extent of 100 m under different updraft velocities. Simulations with turbulence show two dissipation rates: ϵ=50 cm^2 s^{-3} and ϵ=10 cm^2 s^{-3} (solid and dotted lines). Additionally, the blue and red shaded regions mark intermediate values of ϵ. For more information see the caption of Fig. 4.5.

4.1.5 Collection Initiation

Following a similar approach as Hartman and Harrington (2005a), the collection initiation timescale τ_{coll} is calculated as the time needed to grow droplets with a number concentration of n_{max}=0.1 cm^{-3} that have a radius larger than $r_{drizzle}$=20 μm. The noise of τ_{coll}, due to a small number of droplets in the tail, decreases with increasing n_{max}, but the timescale itself increases. A trade-off value for n_{max} is chosen to balancing the two impacts. Figure 4.7 shows that turbulence and radiation lower τ_{coll}. Turbulence alone lowers τ_{coll} significantly (blue) while radiation alone has only a small impact (yellow). However, the combination of turbulence and radiation (red) shows significantly shorter timescales for collection initiation than turbulence alone. A interesting feature is the peak of the collection initiation time centered around w=0.2 m s^{-1} (depending on ϵ) for the turbulent simulations (blue) and around w=0.6 m s^{-1} for RAD&T simulations (red). For larger updraft speeds, adiabatic cooling due to w dominates the collision initiation timescale and the differences between parametrizations become small. For turbulent simulations (red and blue) and updrafts below the peak, the additional spread in the droplets populations significantly reduces τ_{coll}. The parameters of the time series in Figure 4.3 are indicated by black vertical lines in the Figure 4.7 and show that both updrafts (0.1 and 1 m s^{-1}) produce drizzle at a similar rate, if turbulence is included (blue and red).

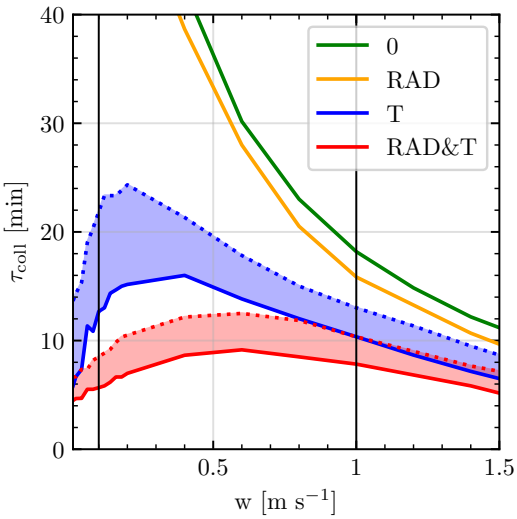

Figure 4.7: A sensitivity study of the collision initiation timescale with respect to the updraft velocity. τ_{coll} is defined as the time needed to have n_{max}=0.1 cm^{-3} with size r>$r_{drizzle}$. Two dissipation rates are shown: ϵ=50 cm^2 s^{-3} and ϵ=10 cm^2 s^{-3} (solid and dotted lines). Additionally, the blue and red shaded regions mark intermediate values of ϵ. The vertical black lines at w=0.1 m s^{-1} and w=1 m s^{-1} mark where the previously shown distributions and time series are evaluated. The label and color convention is the same as in the Figure 4.1.

4.1.6 Sedimentation

This section is intended to quantify the vertical droplet dispersion due to sedimentation in the context of a parcel model of 50 m vertical extent. The sedimentation speed of the droplets can be calculated with a piecewise function of the droplet radius as shown in Equation 4.2 and provided by Rogers and Yau (1996).

$$v(r) = \begin{cases} 1.19 \cdot 10^8 \cdot r^2, & \text{if} \quad r < 40 \cdot 10^{-6} \text{ m} \\ 8 \cdot 10^3 \cdot r, & \text{if} \quad 40 \cdot 10^{-6} < r < 0.6 \cdot 10^{-3} \text{ m} \\ 2.01 \cdot 10^2 \cdot r^{1/2}, & \text{else} \end{cases} \tag{4.2}$$

A spectrum of droplet radii will lead to a spectrum of sedimentation speeds. The sedimentation distance after 15 min for each droplet can be obtained by integrating the sedimentation speeds over time. Figure 4.8 shows the standard deviation of the total sedimentation distances obtained over all droplets. More precisely, 4 times the standard deviation, which states that 95.4 % of the droplets have a relative distance below $4 \cdot \sigma_{dz}$ m, in the approximation of a Gaussian distribution of sedimentation distances. The intermediate updrafts between w=0.2 m s^{-1} and w=0.4 m s^{-1} show the largest spread, with a maximum of 30 m, which is below the assumed vertical parcel length of 50 m.

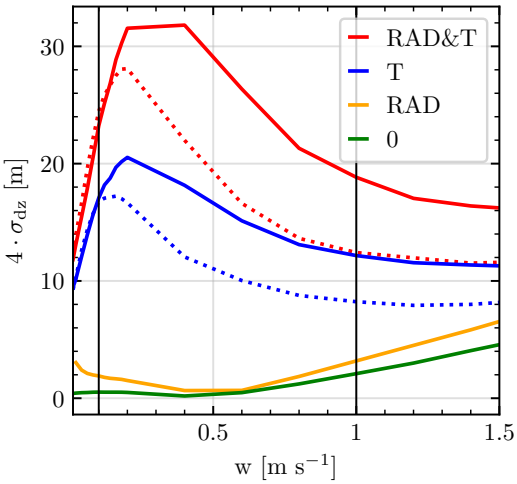

Figure 4.8: A sensitivity study of the relative sedimentation distances evaluated after 15 min. In the Gaussian approximation 95, 45% of the droplets have a relative vertical distance below $4 * \sigma_{dz}$. For simulations with turbulence, two dissipation rates and updrafts are shown: ϵ=50 cm^2 s^{-3} with w=1 m s^{-1} and ϵ=10 cm^2 s^{-3} with w=0.1 m s^{-1} (solid and dotted lines). The vertical black lines at w=0.1 m s^{-1} and w=1 m s^{-1} indicate where previously shown distributions and time series are evaluated. The label and color convention is the same as in the Figure 4.1.

4.1.7 Sensitivity to the Aerosol Distribution

This section is intended to access the impact of the aerosol distribution. In Fig. 4.9 the time series results for simulations with different CCN number concentrations (left panels) and ratios of n_{20}/n_{ccn} (right panel) are shown. n_{20}/n_{ccn}=0 signifies that the CCN are only taken from the larger aerosol mode and n_{20}/n_{ccn}=1 that the CCN are only taken from the smaller aerosol mode, with a constant n_{ccn}=100 cm^{-3}. The standard deviation of the droplet size distribution is influenced by the evolution of the saturation in the nucleation process. A higher and broader peak in saturation gives rise to more diverse saturation growth histories of the droplets and therefore a larger standard deviation. The peak saturation increases with a decreasing droplet number concentration, because less droplets bind less water in short time intervals. The experiments either decrease the droplet number concentration directly by decreasing the CCN number concentration (left panel) or indirect by using smaller CCN sizes which need higher peak saturations to nucleate. Smaller droplet number concentrations also lead to a larger mean radius, because the condensed water is shared among less droplets. Consequently, the increasing mean radius and standard deviation lead to a increasing maximal radius. Figure 4.10 confirms that larger mean radii, standard deviations and maximal radii result from smaller droplet number concentrations in all parametrization combinations.

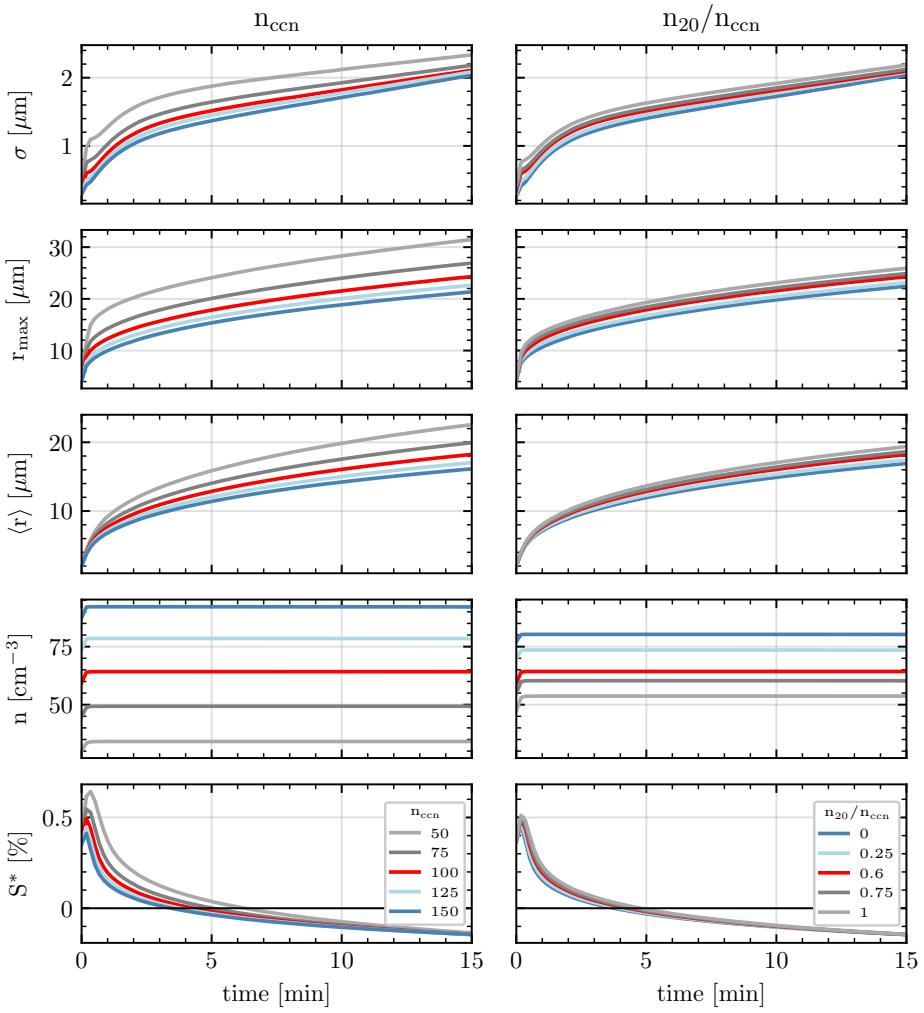

Figure 4.9: The time series are evaluated from the beginning of condensation over 15 min with w=1 m s^{-1}, f=1/6, ϵ=50 cm^2 s^{-3} and with the combination of radiation and turbulence (RAD&T). The red lines represent the reference simulations with n_{ccn}=100 cm^{-3} and n_{20}/n_{ccn}=0.6. The left panel shows a sensitivity study with respect to the CCN number concentration n_{ccn}. The gray colors represent n_{ccn} values below and the blue colors above 100 cm^{-3}. The right panel shows a sensitivity study with respect to the CCN number concentration ratio n_{20}/n_{ccn} with $n_{ccn}=n_{20}+n_{75}$=100 cm^{-3} from the two aerosol modes. The gray colors represent larger ratios and therefore smaller CCN and the blue colors represent smaller ratios and therefore larger CCN compared to the reference ratio of 0.6.

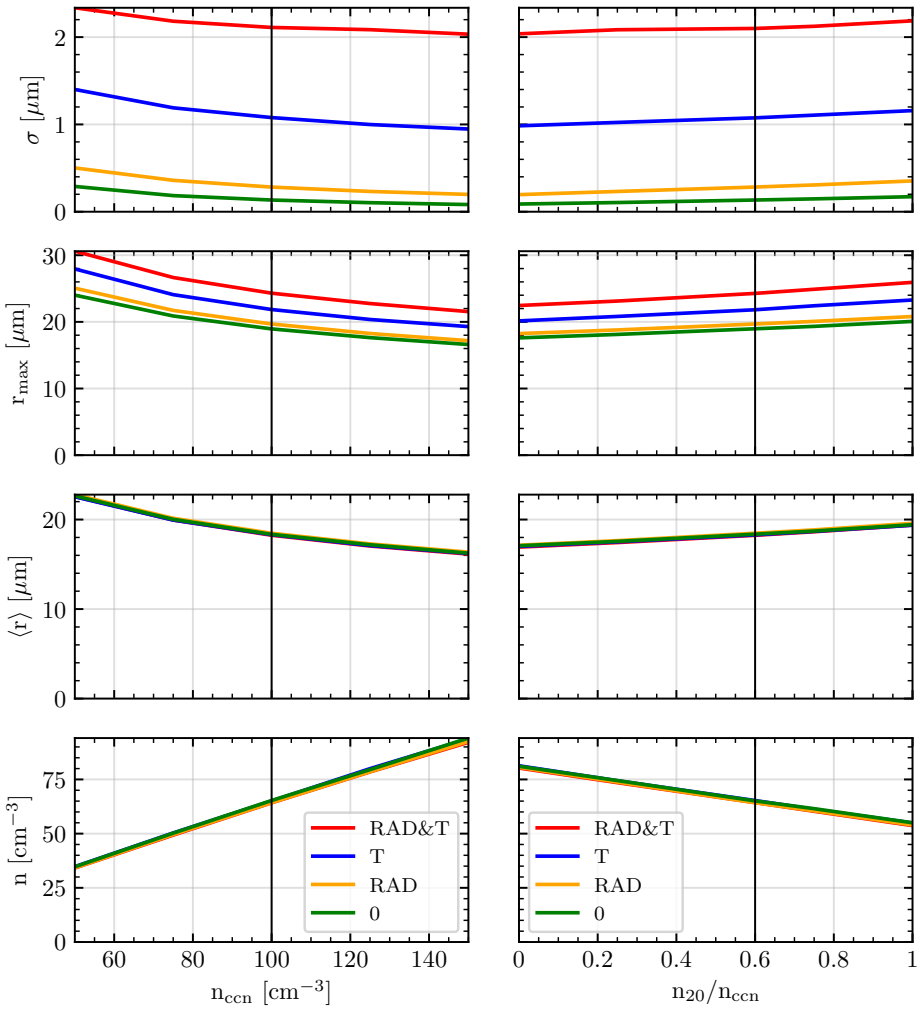

Figure 4.10: The simulations are evaluation after 15 min and run with with w=1 m s^{-1}, f=1/6 and ϵ=50 cm^2 s^{-3}. The left panel shows the sensitivity with respect to the CCN number concentration n_{ccn} and the right panel with respect to the CCN number concentration ratio n_{20}/n_{ccn} with $n_{ccn}=n_{20}+n_{75}$ from the two aerosol modes. The vertical black lines indicate the reference values of n=100 cm^{-3} and n_{20}/n_{ccn}=0.6. For more information see the caption of Figure 4.5.

Chapter 5

Large Eddy Simulations

This chapter starts by presenting the model settings for the atmospheric model: the Parallelized Large-Eddy Simulation Model (PALM) (Raasch and Schröter, 2001; Maronga et al., 2015). Furthermore, a explanation of the used syntax and variables is given, to prepare the reader for the subsequent experiments. Finally, the experiments investigate the convergence of the Lagrangian microphysics and the sensitivity with respect to Radiative enhAnced Diffusional (RAD) growth and the turbulence parametrization. Shown are time series and profile data.

The initial profiles are based on the first nocturnal research flight (RF01) of the Dynamics and Chemistry of Marine Stratocumulus field study (DYCOMS-II), presented in Stevens et al. (2005). The liquid water potential temperature Θ_l and the cloud water mixing ratio q_c are given in Eq. (5.1), with $z_i = 850$ m.

$$\begin{aligned} \Theta_l &= \begin{cases} 289 \text{ K}, & \text{for } z \leq z_i \\ 297.5 + (z - z_i)^{1/3} \text{ K}, & \text{for } z > z_i \end{cases} \\ q_c &= \begin{cases} 9 \quad \text{g kg}^{-1}, & \text{for } z \leq z_i \\ 1.5 \text{ g kg}^{-1}, & \text{for } z > z_i \end{cases} \end{aligned} \tag{5.1}$$

The geostrophic winds are set to $u_g = 7$ and $v_g = -5.5$ m s^{-1}. The domain size in x, y and z direction is set to 400, 400 and 1600 m with a constant grid spacing of 25 m. The total simulation time was set to 1 h, with a time step of 1 s.

The first 30 min are not evaluated and considered the spin up period, in which random disturbances are added to the horizontal velocity field until convection is triggered, with an

amplitude of 0.25 m s^{-1} every 2.5 min. This happens after approximately 10 min. During the spin up period, maximal vertical wind speeds of 7 m s^{-1} are reached, which relax within 25 min to approximately 1.5 m s^{-1}. During this period, dry air is entrained into the stratus cloud deck, which reduces the liquid water content.

The experiments are evaluated with up to $N_{ens} = 20$ ensemble members, which are generated with statistically independent random numbers from different random number seeds. The time series and profiles show the mean over the ensemble, with an error bar according the standard deviation of the mean estimator.

The Schwarzschild radiation routine from the Tenstream software package is called in every model time step. It calculates the optical properties from the Rapid Radiative Transfer Model (RRTMG) Clough et al. (2005). The broadband ground albedo is set constant to 0.06 for long and short wave radiation, which describes an ocean according to Brenguier and Chaumat (2001). The resulting radiative heating rates are feedback to the atmospheric temperature field, if not stated otherwise.

The stratus clouds are represented using a Lagrangian approach (Andrejczuk et al., 2008; Shima et al., 2009; Sölch and Kärcher, 2010; Riechelmann et al., 2012). The processes of nucleation and collisions are excluded. Superdroplets grow freely from a minimal radius of $r_0 = 10^{-8}$. The number concentration is set to 100 cm^{-3}, if not stated otherwise. Superdroplets are coupled to subgrid velocities, which are calculated according to Kim et al. (2005).

The representation of rare, large droplets (drizzle) is improved by the splitting approach, which is evaluated in Schwenkel et al. (2018). The critical splitting radius is set to 15 μm, which is the estimated beginning of the condensation coalescence bottleneck. The critical droplet multiplicity is set to $0.03 \cdot N_i$, below which no splitting is applied. No surface model is used and the surface latent and sensible heat fluxes are set to zero. This simplifies the simulations setup, but becomes increasingly unrealistic with simulation time. Furthermore, droplets that collide with the surface are absorbed.

In general, each time series plot has a corresponding profile plot, which shows the same or closely related quantities in the same order.
The averaged quantities $\langle * \rangle_{*gc}$ are calculated over the total domain for time series and over each horizontal layers in the profile figures. Furthermore, the evaluated grid cell subsets are indicated with the subscript of the square brackets and explained in the Table (5.1).

The capitalized letters correspond to domain integrated quantities, which are calculated

according to:

$$M = \oint_V \rho_0 q_c \, dv \qquad N = \oint_V n \, dv \tag{5.2}$$

The same applies for the total integrated drizzle mass M_{zz} and drizzle number N_{zz}. The profiles show the layer integrated quantities, which can be described according to:

$$\frac{\delta M}{\delta z} = \oint_F \rho_0 q_c \, df \qquad \frac{\delta N}{\delta z} = \oint_F n \, df. \tag{5.3}$$

$F = \Delta x \cdot \Delta y$ is the total LES domain area. The same applies for the layer integrated drizzle mass profile $\frac{\delta M_{zz}}{\delta z}$ and drizzle number profile $\frac{\delta N_{zz}}{\delta z}$.

The normalization, indicated by the wide hat above the quantities, is done with respect to the reference parametrization and time point (e.g. after 30 min). Equation (5.4) shows the normalized cloud water mass as example. The reference simulation parametrization changes over the experiments, which is indicated in the respective figure captions.

$$\widehat{\frac{\delta M}{\delta z}} = \frac{1}{M_{ref}} \frac{\delta M}{\delta z} \tag{5.4}$$

gc	grid cells	all
cgc	cloudy grid cells	$q_c > 10^{-7}$ [kg kg^{-1}]
dgc	drizzle grid cells	$q_{zz} > 0$

Table 5.1: Grid cell subset definitions and their notation

5.1 Results

5.1.1 Superdroplet Convergence Experiment

The key idea in this experiment is that the simulations become more realistic and representative of real clouds by increasing the number of superdroplets. The Lagrangian microphysical parametrization has converged to reality, when each superdroplet is representing only one aerosol particle or droplet. However, a large number of superdroplets lead to slow and memory intensive simulations, which are not feasible at LES scales. Therefore, the first question is:

How many superdroplets are required to represent drizzle formation in a stratus cloud?

The following experiment increases the number of superdroplets per grid cell (N_{sd}) in the stratus cloud simulations until the microphysical properties show convergence. Convergence is measured according to the root mean square (RMS), calculated with Eq. (3.22) over a 5 min period between 55 and 60 min. Table (5.2) summarizes the RMS results for a set simulations with different N_{sd}. In addition to the RMS values, it shows the percentage relative to the reference simulation, the relative RMS. Here, the reference simulation is the one with the largest number of superdroplets $N_{sd} = 2{\cdot}10^4$.

The figures show time series of integrated quantities and the atmospheric profile data, which are separated into cloud (Figures 5.1 and 5.3) and drizzle (Figures 5.2 and 5.4) quantities. In this experiment, N_{sd} is increased from 10 to $2{\cdot}10^4$ in steps each by a factor of 10, with the exception of the largest two simulations, which are only altered by a factor of 2. The 10^3sp simulation additionally runs with activated splitting algorithm for larger droplets. $N_{sd} = 2{\cdot}10^4$ is chosen out of computational limitations. Therefore, it can not be stated that the microphysics has converged for certain. However, the inclusion of the large droplet splitting for the intermediate simulation of 10^3 shows good agreement with the reference simulation $2{\cdot}10^4$, The simulation, which includes the large droplet splitting is called 10^3sp.

cloud quantities

The time series results in Figure 5.1 show, that the total mass of water in the atmosphere to the LES domain surface area (M/F) and the total number of cloud droplets in the atmosphere to the LES domain surface area (N/F) are not sensitive to N_{sd}. The RMS values are around 2% and 1.2%, already for a very low superdroplet number of $N_{sd} = 10^2$. The integrated stratus cloud quantities M/F and N/F are prescribed from the initial profiles and independent from details of the microphysics. For the same reason, the saturation adjustment approach already yields a good representations of M/F in McDonald (1963). In a saturation adjustment simulation the supersaturation is instantaneously brought down to saturation (in one model time step), which turns all the access supersaturation into liquid

water.

The time series of the mean quantities $\langle q_c \rangle_{cgc}$ and $\langle n \rangle_{cgc}$ decrease in value with increasing N_{sd} and reach relative RMS values of 7.8% and 6.5% for $N_{sd} = 10^3$. The profiles in Figure 5.3 show, that those quantities are biased towards larger values at the cloud top and bottom for simulations with a low number of superdroplets $N_{sd} = 10$. Therefore, the cloud edges need a larger number of superdroplets than the cloud center to adequately sample the different saturation conditions. A droplet can experience a wide range of conditions due to the mixing of dry and moist air. The shift towards larger mean values at the cloud edges, is introduced from multiplicity factors that are too large. The number of superdroplets at initialization is too low. As a result, cloud edge conditions are favored to initiate a cloudy cell, if they have larger supersaturations, which result in larger values for mean quantities like $\langle q_c \rangle_{cgc}$ and $\langle n \rangle_{cgc}$.

drizzle quantities

In contrast to the integrated cloud quantities, is the formation of drizzle very sensitive to N_{sd}. This highlights the error of classical one or two moment schemes, which do not explicitly resolve the droplet positions and the droplet number and therefore rely on approximations for the local droplet number concentration. The profiles in Fig. 5.4 show that drizzle is mainly formed at the cloud edges, especially at the cloud top. The formation of drizzle happens in conditions of high supersaturation and low droplet number concentration.

The profiles also reveal, that $N_{sd} = 10$ is not sufficient to represent the formation of drizzle. The low superdroplet number leads to underrepresented drizzle profiles, which is especially pronounced for the mean quantities $\langle q_{zz} \rangle_{dgc}$ and $\langle n_{zz} \rangle_{dgc}$.

The time series reveal, that if the multiplicity is too large, only the rare, high supersaturation conditions actually produce drizzle. Those conditions are less frequent. Therefore, show the integrated quantities like total drizzle water per LES domain area M_{zz}/F and total drizzle droplet number per LES domain area N_{zz}/F smaller values, which increase with increasing N_{sd}. These conditions are rare, but they have the potential to produce larger values for drizzle cloud water and droplet number concentration. Therefore, the mean quantities $\langle q_{zz} \rangle_{dgc}$ and $\langle n_{zz} \rangle_{dgc}$ decrease with increasing N_{sd}. The Table 5.2 summarizes the results, where M_{zz}/F and N_{zz}/F have RMS values of 15.9% and 8.4% and $\langle q_{zz} \rangle_{dgc}$ and $\langle n_{zz} \rangle_{dgc}$ have RMS values of 276.4% and 251.1%. The bad representation is also the reason for the large RMS values in Table 5.2 found for simulations with low superdroplet number.

The representation of mean drizzle quantities can be notably improved by adding the large droplets splitting algorithm to the simulations Schwenkel et al. (2018). The algorithm improves the sampling of drizzle generating conditions by converting a few superdroplets

		$\Delta_{ref}10$	(%)	$\Delta_{ref}10^2$	(%)	$\Delta_{ref}10^3$	(%)	$\Delta_{ref}10^4$	(%)	$\Delta_{ref}10^3$sp	(%)
M/F	[g m^{-2}]	3.16	(4.5)	1.44	(2.0)	1.51	(2.2)	1.7	(2.4)	0.16	(0.2)
N/F	[mm^{-2}]	787.99	(3.1)	297.47	(1.2)	260.26	(1.0)	461.06	(1.8)	350.44	(1.4)
$\langle q_c \rangle_{cgc}$	[mg kg^{-1}]	67.58	(39.6)	39.26	(23.0)	13.27	(7.8)	1.24	(0.7)	2.21	(1.3)
$\langle n \rangle_{cgc}$	[cm^{-3}]	23.35	(37.5)	13.8	(22.2)	4.06	(6.5)	0.52	(0.8)	0.31	(0.5)
$\langle r \rangle_{cgc}$	[μm]	0.16	(2.1)	0.49	(6.2)	0.27	(3.4)	0.13	(1.7)	0.18	(2.3)
$\langle \sigma \rangle_{cgc}$	[μm]	1.2	(39.5)	0.9	(27.4)	0.4	(14.2)	0.2	(6.0)	0.2	(6.8)
M_{zz}/F	[mg m^{-2}]	388.68	(78.6)	284.6	(57.6)	78.65	(15.9)	58.02	(11.7)	80.3	(16.2)
N_{zz}/F	[mm^{-2}]	9.81	(74.1)	6.62	(50.0)	1.11	(8.4)	1.61	(12.2)	1.38	(10.4)
$\langle q_{zz} \rangle_{dgc}$	[mg kg^{-1}]	306.89	(19485.4)	31.49	(1999.7)	4.35	(276.4)	0.41	(26.2)	0.1	(6.6)
$\langle n_{zz} \rangle_{dgc}$	[dm^{-3}]	9992.16	(23673.4)	1002.28	(2374.6)	105.98	(251.1)	11.27	(26.7)	0.88	(2.1)
$\langle r_{zz} \rangle_{dgc}$	[μm]	1.43	(6.5)	1.24	(5.6)	0.03	(0.2)	0.12	(0.5)	0.11	(0.5)
dgc/cgc		0.76	(99.9)	0.74	(97.6)	0.52	(69.1)	0.07	(9.4)	0.06	(8.3)

Table 5.2: The root mean square data with respect to the reference simulation N_{sd}=2·10^4 evaluated over 5 min for t<55 min according to Eq. (3.22). The corresponding Figures are 5.1 and 5.2. The RMS and relative values are calculated with respect to the 2·10^4 simulation.

with high multiplicity to several superdroplets with low multiplicity, with an independent trajectory. As a result, the representation of the mean drizzle quantities $\langle q_{zz} \rangle_{cgc}$ and $\langle n_{zz} \rangle_{cgc}$ is improved to 6.6% and 2.1% for the RMS. The values for the integrated drizzle quantities M_{zz}/F and N_{zz}/F stay with RMS values of 16.2% and 10.4% approximately constant. Furthermore, the ratio of drizzle containing to cloud containing grid cells dgc/cgc, shown in Figures 5.2 and 5.4 reveal that drizzle containing grid cells become increasingly abundant. The frequency increases especially at the cloud top, which are not rare anymore as the $N_{sd} = 10^3$ simulation suggested.

summary

As a result, the subsequent experiments will use a superdroplet number of 10^3 per grid cell in combination with the splitting algorithm. This combines a good representation of cloud quantities with an improved representation of drizzle quantities.

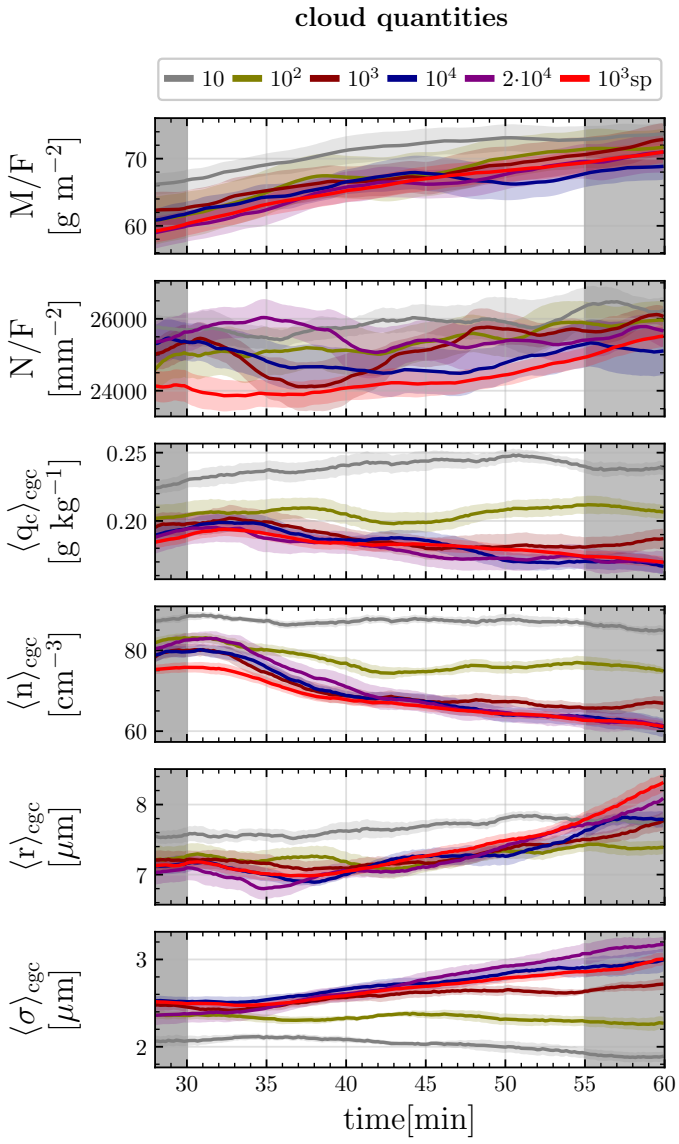

Figure 5.1: The time series data of PALM LES stratus cloud simulations with the RAD&T parametrizations. The RAD and T parametrizations are switched on after 30 min. M/F and N/F show the total water mass and total number of droplets in the atmosphere each over the LES domain surface area F. The superdroplets per grid cell are changed from 10 to $2{\cdot}10^2$ and the splitting algorithm is added in 10^3sp. The averages are evaluated according to the Table (5.1). The time series error shows the standard deviation of the mean estimator function for at least 6 ensemble runs Eq. (3.21). The gray shaded regions <30 and >55 min indicate the spin up period and the evaluation period of the RMS values summarized in the Table (5.2).

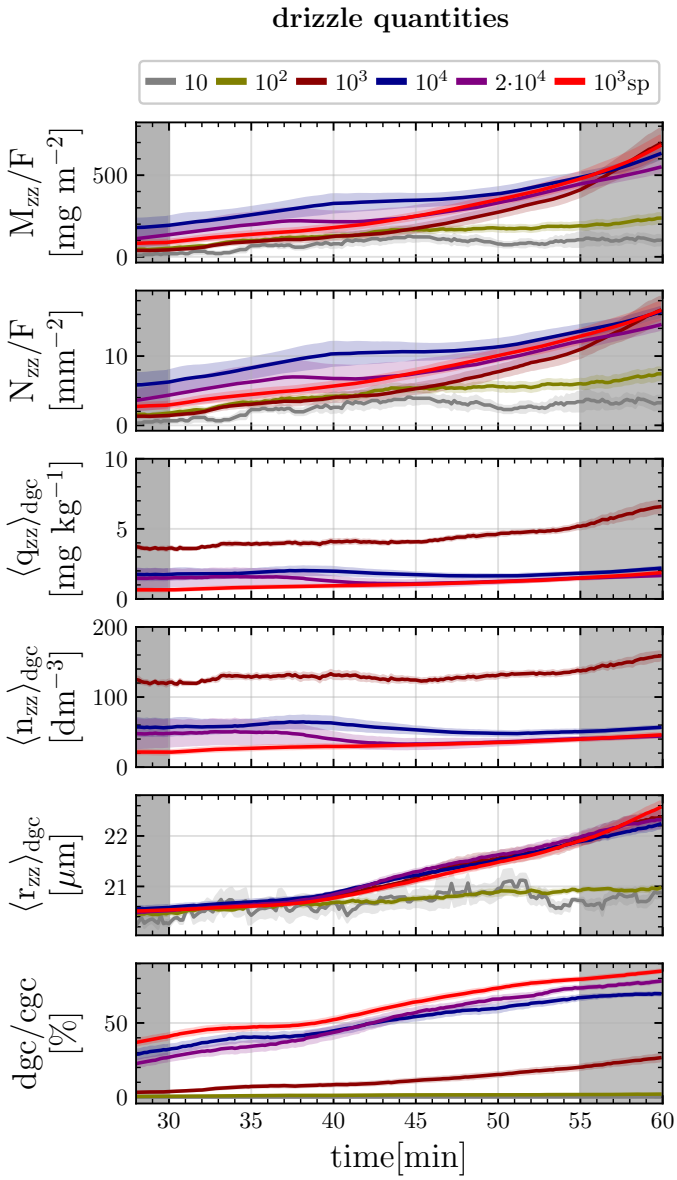

Figure 5.2: The time series data of PALM LES drizzle quantities. M_{zz}/F and N_{zz}/F show the total drizzle mass and total number of drizzle droplets in the atmosphere each over the LES domain surface area F. The results for $N_{sd} < 10^3$ in $\langle q_{zz} \rangle_{dgc}$ and $\langle n_{zz} \rangle_{dgc}$ are neglected, due to their large values. Further information can be found in the caption of Figure 5.1

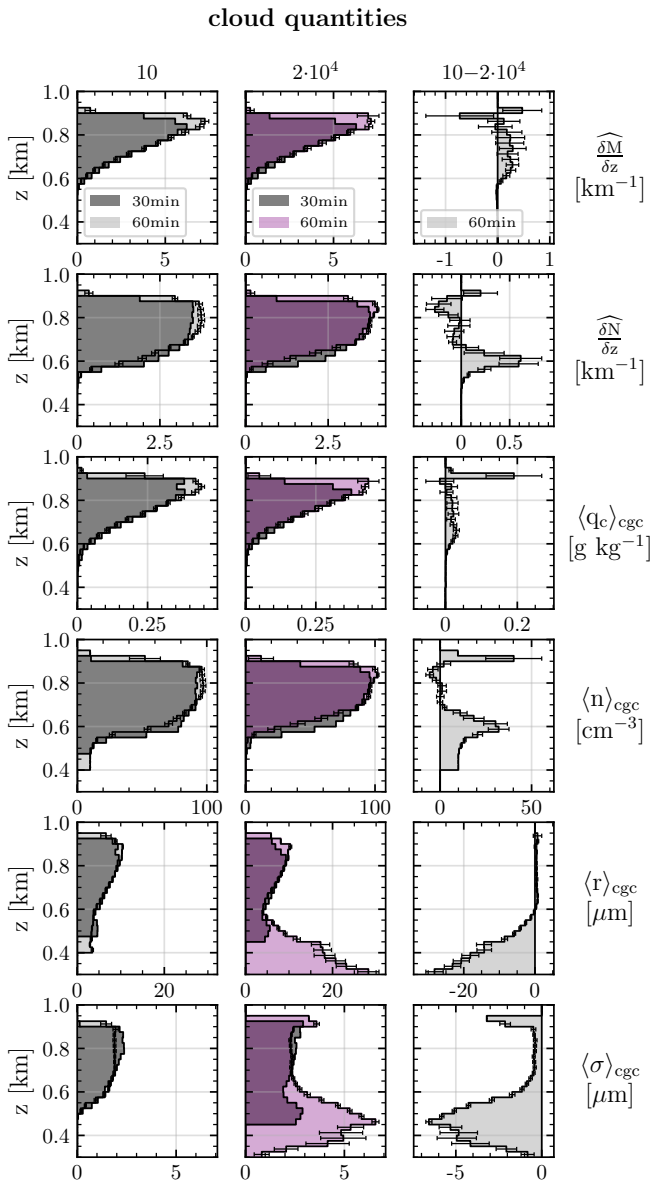

Figure 5.3: The Profiles of cloud quantities from PALM LES stratus simulations, that are averaged over a 2 min interval and ensemble runs. The plots with $\widehat{\delta M}/\delta z$ and $\widehat{\delta N}/\delta z$ show the vertical normalized distribution of the total water mass and cloud droplet number. $\langle q_c \rangle_{cgc}$, $\langle n \rangle_{cgc}$, $\langle r \rangle_{cgc}$ and $\langle \sigma \rangle_{cgc}$ show the average values of the respective quantity for each model layer over cloudy grid cells (cgc). The RAD and T parametrizations are switched on after 30 min. The first two columns highlight the temporal evolution for one setup and the right column shows the difference between parametrizations after 60 min. The error bars show the standard deviation of the mean estimator function for at least 6 ensemble runs Eq. (3.21). Compared are the smallest and the largest tested number of superdroplets 10 and $2{\cdot}10^2$. The integrated quantities are normalized with respect to the $2{\cdot}10^2$ simulation at 30 min according to Eq. (5.4).

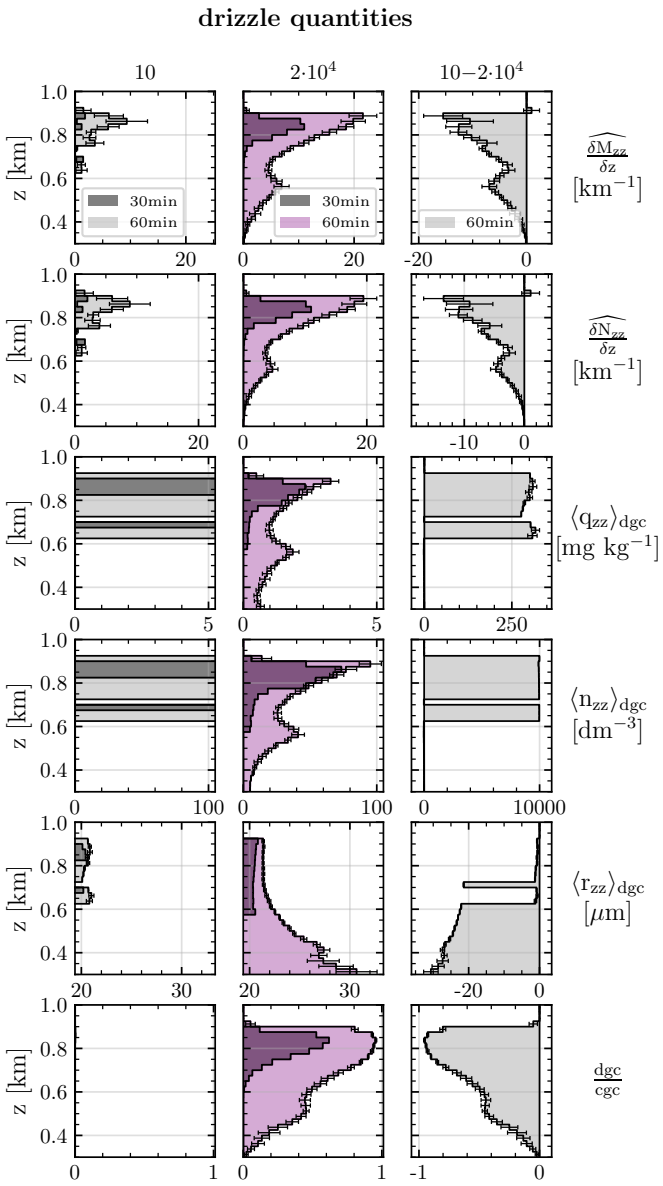

Figure 5.4: The plots with $\widehat{\delta M_{zz}/\delta z}$ and $\widehat{\delta N_{zz}/\delta z}$ show the vertical normalized distribution of the total drizzle mass and drizzle droplet number. $\langle q_{zz}\rangle_{dgc}$, $\langle n_{zz}\rangle_{dgc}$, $\langle r_{zz}\rangle_{dgc}$ and dgc/cgc show the average values of the respective quantity for each model layer over drizzle containing grid cells (dgc). The presented range of $\langle q_{zz}\rangle_{dgc}$ and $\langle n_{zz}\rangle_{dgc}$ are limited due to the large values for the $N_{sd} = 10$ case. Further information can be found in the caption of the Figure 5.3.

5.1.2 Thermal Cooling Experiment

The thermal cooling experiment aims to answer the question:

> ***What is the impact of thermal radiation, when (only) acting on the temperature field?***

This experiment may serve as a interpretation basis on the importance of the here tested parametrizations. Furthermore, it is an interesting experiment in itself. Here, the radiation routine is switched off after 30 minutes and the simulations continue for another 30 minutes. The experimental setup chosen this way, because all subsequent experiments evolve starting from a spin up period with radiation, which is changing the temperature field. In following, the reference simulation is denoted 0. It applies thermal radiation to the temperature field, but does not include the turbulence or RAD growth parametrizations.

environment quantities

The Figure 5.9 shows the Profiles of selected environment variables. The layer averaged thermal cooling rates $\langle \dot{h}_{rad} \rangle_{cgc}$ are calculated only for the reference simulation (0). The profiles show that the reference simulations sustains the subgrid-scale kinetic energy (e) over the whole cloud, in contrast to the NoHeat simulation. Thermal radiative cooling introduces turbulent motions. As a result, e appears to be approximately constant with $e = 0.005\ m^2\ s^{-2}$ over the cloud and peaks at the cloud edges. Furthermore, the cloudy grid cell integrated saturation profiles ($\widehat{\frac{\delta S^*_{tot}}{\delta z}}_{cgc}$) show that mixing of subsaturated air into the cloud strongly decreases at the cloud edges for the NoHeat simulation. At the same time, the changes in the averaged saturation profile ($\langle S^* \rangle_{cgc}$) are small. Therefore, the distribution of saturation conditions stays constant, but the total subsaturation increases, due to more subsaturated grid cells. Furthermore, the normalized liquid water profile in subsaturated conditions ($\widehat{\frac{\delta M_{S^*<0}}{\delta z}}$) is increasing across the cloud for the sedimentation dominated and evaporating NoHeat stratus simulation.

The sharply defined cloud top is due to the presence of a strong inversion above the cloud. In contrast to the more spread out cloud bottom from the indifferent initial potential temperature profile below the cloud top. The whole cloud, especially the cloud edges, are in a constant state of development and dissolution. For the simulations with radiation (0), condensation is stronger than evaporation. In contrast, without radiation (NoHeat), evaporation is stronger than condensation. The cloud top cooling of the 0 simulations is moving upwards due to additional condensation from the cloud top cooling and the cloud bottom moves upward due to the evaporation from cloud bottom warming.

cloud quantities

The time series data in Figure 5.5 show for the simulations with radiation (0) that M/F and N/F increases over time by 16.6% and 7.2% respectively. The profiles in Figure 5.7 of $\widehat{\frac{\delta M}{\delta z}}$ and $\widehat{\frac{\delta N}{\delta z}}$ show, that the increase is due to the additional droplets at the cloud top from radiative cooling induced condensation. The droplet evaporation at the cloud bottom is due to the radiative warming and the condensation at cloud top from radiative cooling. Without radiation (NoHeat), the integrated quantities, M/F decreases by 21.8% and N/F increases by 1.9% compared to 0. Sedimentation of droplets from the cloud top, where the most liquid water is located, increases $\frac{\delta M}{\delta z}$ and $\frac{\delta N}{\delta z}$ at the cloud center. This leads to an overall increase of N/F for 0 and NoRad. The profiles of $\widehat{\frac{\delta M}{\delta z}}$ and $\widehat{\frac{\delta N}{\delta z}}$ from Figure 5.7 show the increase at the cloud center. This may be a direct remnant of neglecting the nucleation process in the LES simulations. The process of nucleation imposes a critical supersaturation S_{crit}, that has to be reached and a critical droplet radius r_{cri} that has to be surpassed in order for the droplets to nucleate or renucleate. Nucleated droplets grow freely from the surrounding supersaturation. The presented temporal development of the integrated and mean quantities is qualitatively similar, which indicates that the shape of the distribution for the respective quantities has not changed. The profile of the mean droplet radius increases with height with a global maximum at cloud top and a local maximum at the cloud base. Furthermore, the droplet size standard deviation for the simulations with radiation is closely centered around 2 μm over the cloud with pronounced peaks at the cloud edges.

drizzle quantities

The drizzle droplets have radii larger then 20 μm and initiate collisions and therefore the formation of rain. The time series in Figure 5.6 show, that M_{zz}/F and N_{zz}/F increase by 75.3% and 68% over time for simulations with radiation (0). This is due, to the drizzle droplets introduced at the cloud top by thermal radiation, as the profiles in Figure 5.8 suggest. For simulations without radiation (NoHeat), M_{zz}/F and N_{zz}/F decrease by 65.4% and 64.1% with respect to 0. The averaged quantities $\langle q_{zz}\rangle_{dgc}$ and $\langle n_{zz}\rangle_{dgc}$ show a similar qualitative behavior as the integrated quantities. Not all cloudy grid cells contain drizzle yet, as shown in the dgc/cgc profile. For the simulations with radiation (0), the dgc/cgc ratio increases over time by 58.8% and it increases by 19.2% compared to the simulation without radiation (NoHeat).

summary

Thermal radiation already has a significant impact on drizzle formation, if (only) coupled to the temperature field. The total amount of drizzle water and drizzle droplet decrease by approximately 2/3, with the largest difference at the cloud top.

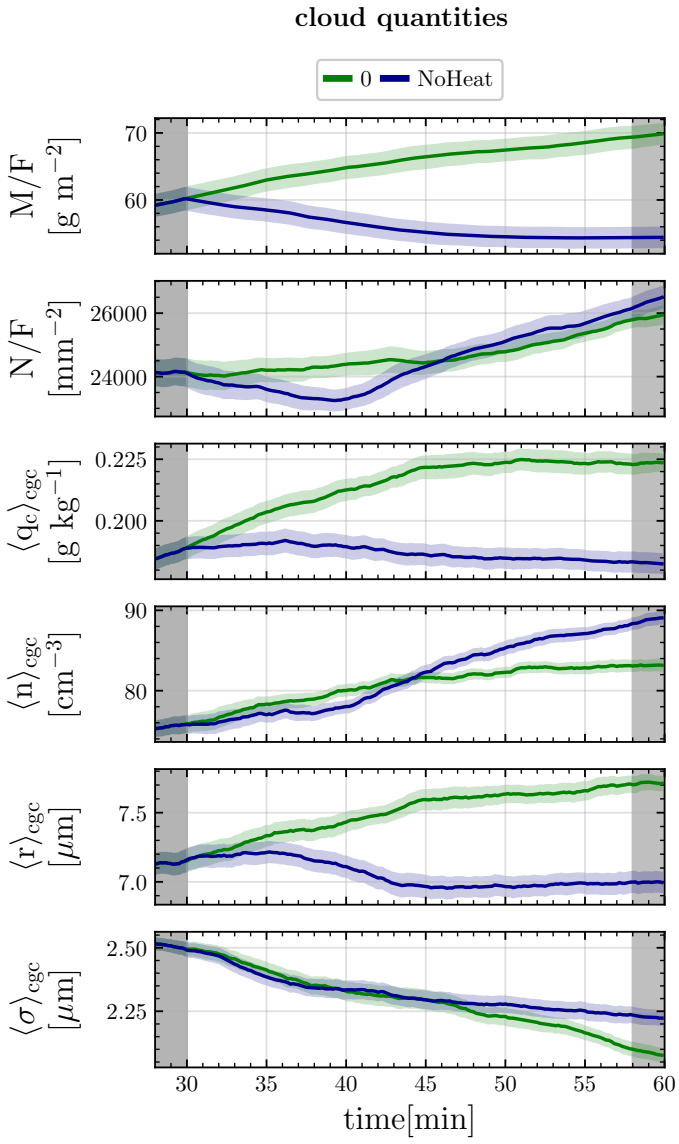

Figure 5.5: The time series data of PALM LES stratus cloud simulations with (0) and without (NoHeat) radiation coupled to the temperature field. The radiation is switched off after 30 min. M/F and N/F show the total water mass and total number of droplets in the atmosphere each over the LES domain surface area F. The superdroplets per grid cell are set to $N_{sd} = 10^3$ with large droplet splitting. The averages are evaluated according to the Table (5.1). The time series error shows the standard deviation of the mean estimator function for at least 20 ensemble runs Eq. (3.21). The gray shaded regions <30 and >58 min indicate the spin up period and the 2 min evaluation period of the mean values are summarized in Table (5.3).

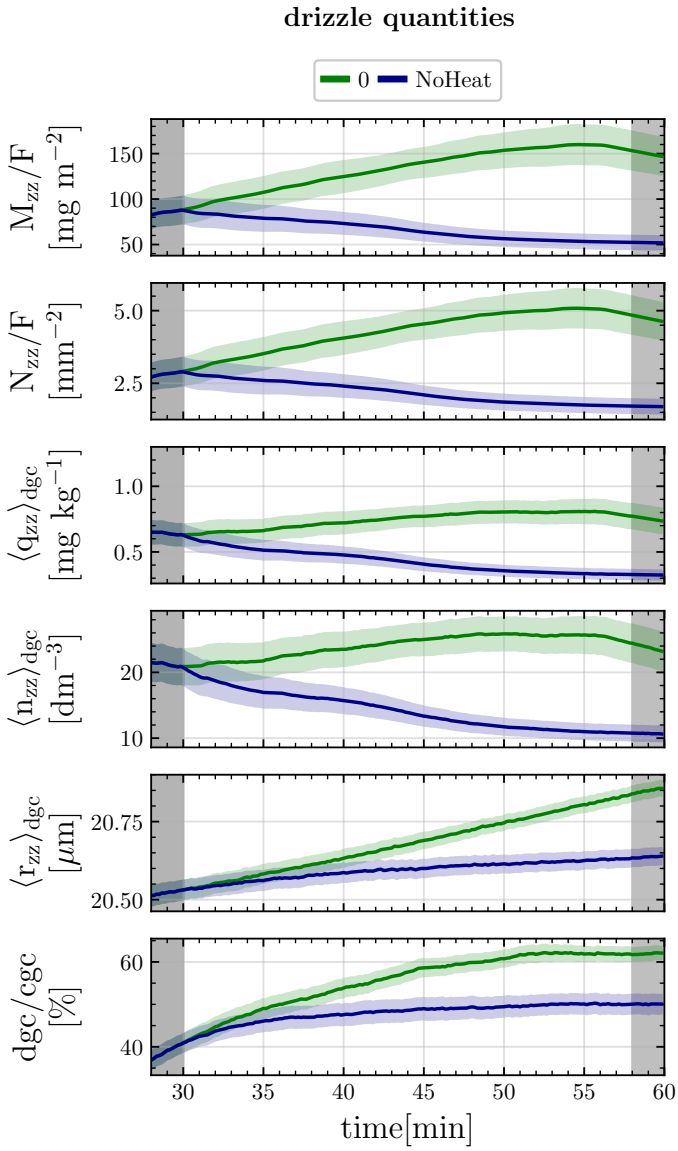

Figure 5.6: M_{zz}/F and N_{zz}/F show the total drizzle mass and total number of drizzle droplets in the atmosphere each over the LES domain surface area F. For further information take a look at the caption of the Figure 5.5.

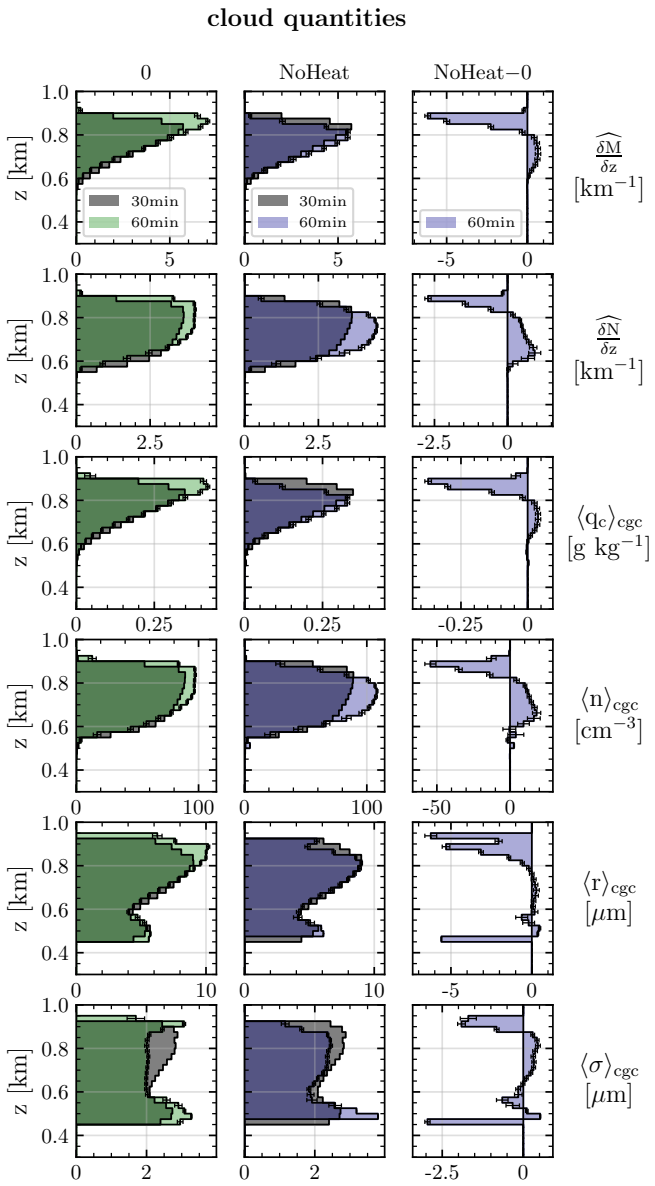

Figure 5.7: The profiles of cloud quantities from PALM LES stratus simulations are averaged over a 2 min interval and ensemble runs. The plots with $\widehat{\delta M}/\delta z$ and $\widehat{\delta N}/\delta z$ show the vertical normalized distribution of the total water mass and cloud droplet number. $\langle q_c \rangle_{cgc}$, $\langle n \rangle_{cgc}$, $\langle r \rangle_{cgc}$ and $\langle \sigma \rangle_{cgc}$ show the average values of the respective quantity for each model layer over cloudy grid cells (cgc). The panels that show two snapshots of the profiles at 30 and 60 min highlight the temporal evolution for one setup and the panels that show the profiles only at 60 min highlight the difference between parametrizations. The error bars show the standard deviation of the mean estimator function for at least 6 ensemble runs Eq. (3.21). Compared are simulations with (0) and without (NoHeat) radiation coupled to the atmospheric temperature. The radiation is switched off after 30 min. The integrated quantities are normalized with respect to the reference simulation (0) at 30 min according to Eq. (5.4).

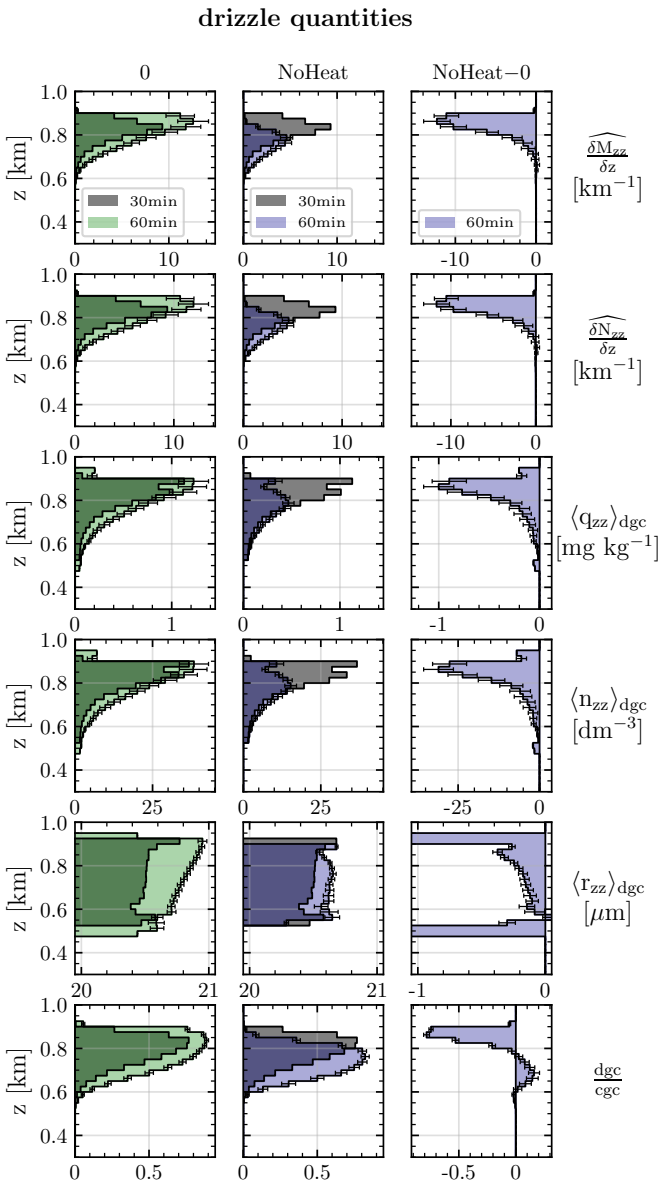

Figure 5.8: The profiles of drizzle quantities from PALM LES stratus simulations. The plots with $\widehat{\delta M_{zz}/\delta z}$ and $\widehat{\delta N_{zz}/\delta z}$ show the vertical normalized distribution of the total drizzle mass and drizzle droplet number. $\langle q_{zz} \rangle_{dgc}$, $\langle n_{zz} \rangle_{dgc}$, $\langle r_{zz} \rangle_{dgc}$ and dgc/cgc show the average values of the respective quantity for each model layer over drizzle containing grid cells (dgc). For further information see the caption of the Figure 5.7.

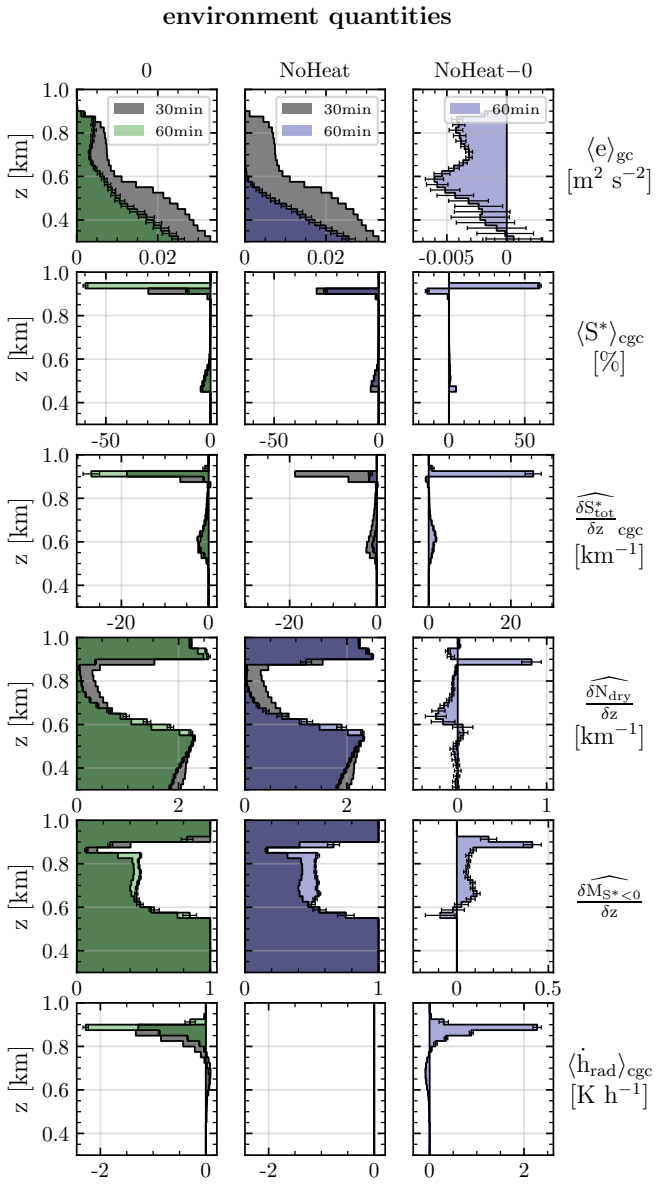

Figure 5.9: The profiles of environment quantities from PALM LES stratus simulations. For further information see the caption of the Figure 5.7.

		$\Delta_t 0$	(%)	Δ_tNoHeat	(%)	NoHeat-0	(%)
M/F	[g m^{-2}]	9.91	(16.6)	-5.29	(-8.9)	-15.2	(-21.8)
N/F	[mm^{-2}]	1725.96	(7.2)	2209.75	(9.2)	481.35	(1.9)
$\langle q_c \rangle_{cgc}$	[mg kg^{-1}]	36.69	(19.6)	-3.75	(-2.0)	-40.46	(-18.1)
$\langle n \rangle_{cgc}$	[cm^{-3}]	7.57	(10.0)	13.18	(17.4)	5.61	(6.7)
$\langle r \rangle_{cgc}$	[μm]	0.58	(8.1)	-0.14	(-2.0)	-0.72	(-9.3)
$\langle \sigma \rangle_{cgc}$	[μm]	-0.42	(-16.7)	-0.28	(-11.1)	0.14	(6.7)
M_{zz}/F	[mg m^{-2}]	64.54	(75.3)	-33.6	(-39.2)	-98.2	(-65.4)
N_{zz}/F	[mm^{-2}]	1.92	(68.0)	-1.12	(-39.6)	-3.04	(-64.1)
$\langle q_{zz} \rangle_{dgc}$	[mg kg^{-1}]	0.11	(17.8)	-0.31	(-49.0)	-0.43	(-56.8)
$\langle n_{zz} \rangle_{dgc}$	[dm^{-3}]	2.66	(12.6)	-10.46	(-49.4)	-13.13	(-55.1)
$\langle r_{zz} \rangle_{dgc}$	[μm]	0.33	(1.6)	0.11	(0.6)	-0.21	(-1.0)
dgc/cgc		0.23	(58.8)	0.11	(28.4)	-0.12	(-19.2)

Table 5.3: The summary table of time series data. The data is averaged over a 2 min time interval after 30 and 60 min and the temporal differences are shown the Δ_t columns. The NoHeat-0 column shows the difference between the parametrizations after 60 min. The relative values in percent for the time differences Δ_t are calculated with respect to the reference simulation (0) after 30 min and for the parametrization differences after 60 min.

5.1.3 Turbulence Experiment

The Turbulence Experiment compares the simulation results with (T) and without (0) the turbulence parametrization for PALM LES stratus simulations. The same parametrizations are used in the parcel simulations and the same colors highlighting and notation is applied. The Figures 5.10 and 5.11 show times series results for the simulations with and without turbulence, but also for with RAD growth with and without turbulence. The RAD growth timeseries are discussed the in section 5.1.4. In contrast, the profile Figures 5.12 and 5.13 compare only the 0 and T parametrizations. The research question of the section is:

How much drizzle is produced by adding the turbulence parametrization?

cloud quantities

The integrated quantities M/F and N/F are only weakly affected by saturation fluctuations. All saturation fluctuations add up to zero, but they change the droplet size distribution. Therefore the speed changes at which water condensates at the droplets. The time series in Figure 5.10 shows an increase in M/F by 10.37 g m^{-2} (17.4%) over time and only by 0.35 g m^{-2} (0.5%) due to turbulence. N/F increases by 1269.4 mm^{-2} (5.2%) over time and decreases by 403.37 mm^{-2} (1.7%) due to turbulence. The profiles in the Figure 5.12 show, that turbulence increases $\delta M/\delta z$ at the cloud bottom and below the cloud. $\delta N/\delta z$ decreases at the cloud bottom and slightly increases below the cloud. Furthermore, $\delta\widehat{N_{dry}}/\delta z$ in Figure A.1 show the evaporation of cloud droplets at the cloud base.

The time series of the mean quantities $\langle q_c \rangle_{cgc}$ decrease over time by –17.15 mg kg^{-1} (–9.2%) and by –53.88 mg kg^{-1} (-24.1%) due to turbulence. $\langle n \rangle_{cgc}$ decrease over time by 14.06 cm^{-3} (–18.5%) and by 21.35 cm^{-3} (–25.7%) due to turbulence.

The profiles show that $\langle q_c \rangle_{cgc}$ is decreased at the cloud bottom and increased below the cloud due to turbulence. It introduces grid cells with low liquid water content at the cloud bottom and below the cloud, which contributes to a decreasing the mean values. Those grid cells would be dry without turbulence and therefore are not included in the cloud quantity calculations. $\langle n \rangle_{cgc}$ is decreased at cloud bottom and slightly increased below cloud. Both changes contribute to a lower mean value.

drizzle quantities

The Figures 5.11 and 5.13 focus on the drizzle development and show that drizzle formation is strongly increased by turbulence. The time series of M_{zz}/F shows an increase by 487.44 mg m^{-2} (563.3%) over time and by 424 mg m^{-2} (282.7%) due to turbulence. Furthermore, N_{zz}/F increases by 11.08 mm^{-2} (388.4%) over time and by 9.19 mm^{-2} (194.2%) due to turbulence.

The profiles reveal, that the increased formation of drizzle droplets happens over the total

		Δ_t0	(%)	Δ_tT	(%)	T-0	(%)
M/F	[g m^{-2}]	10.04	(16.8)	10.37	(17.4)	0.35	(0.5)
N/F	[mm^{-2}]	1779.54	(7.4)	1269.4	(5.2)	-403.37	(-1.6)
$\langle q_c \rangle_{cgc}$	[mg kg^{-1}]	37.02	(19.9)	-17.15	(-9.2)	-53.88	(-24.1)
$\langle n \rangle_{cgc}$	[cm^{-3}]	7.71	(10.2)	-14.06	(-18.5)	-21.35	(-25.7)
$\langle r \rangle_{cgc}$	[μm]	0.59	(8.2)	1.05	(14.7)	0.47	(6.0)
$\langle \sigma \rangle_{cgc}$	[μm]	-0.43	(-17.2)	0.47	(18.8)	0.91	(43.7)
M_{zz}/F	[mg m^{-2}]	65.4	(77.3)	487.44	(563.3)	424	(282.7)
N_{zz}/F	[mm^{-2}]	1.95	(69.8)	11.08	(388.4)	9.19	(194.2)
$\langle q_{zz} \rangle_{dgc}$	[mg kg^{-1}]	0.12	(19.0)	0.99	(153.2)	0.88	(116.0)
$\langle n_{zz} \rangle_{dgc}$	[dm^{-3}]	2.85	(13.6)	18.68	(87.8)	16.13	(67.7)
$\langle r_{zz} \rangle_{dgc}$	[μm]	0.33	(1.6)	1.9	(9.3)	1.58	(7.6)
dgc/cgc		0.23	(59.0)	0.43	(110.5)	0.21	(34.1)

Table 5.4: The summary table of time series data for the comparison of simulations with (T) and without (0) turbulence parametrization. The data is averaged over a 2 min time interval after 30 and 60 min and the temporal differences are shown in the Δ_t columns. The T-0 column shows the difference between the parametrizations after 60 min. The relative values in percent for the time differences Δ_t are calculated with respect to the reference simulation (0) after 30 min and for the parametrization differences after 60 min.

cloud. It is especially pronounced at the cloud bottom. Furthermore, the impact of the additional small droplets and drizzle droplets introduced from saturation fluctuations, can be seen in the time series of $\langle r \rangle_{cgc}$. It first decreases due to the immediate creation of additional small droplets and then increases again, with the onset of drizzle formation. The time series of $\langle r \rangle_{cgc}$ increases by 1.05 μm (14.7%) over time and by 0.47 μm (6%) due to turbulence.

summary

The addition of saturation fluctuations, drastically increases the formation of drizzle. The increase is on the order of 500%. It impacts not only the cloud top, but also the cloud bottom. This is highlighting the role of both cloud edges in the formation of drizzle and eventually rain.

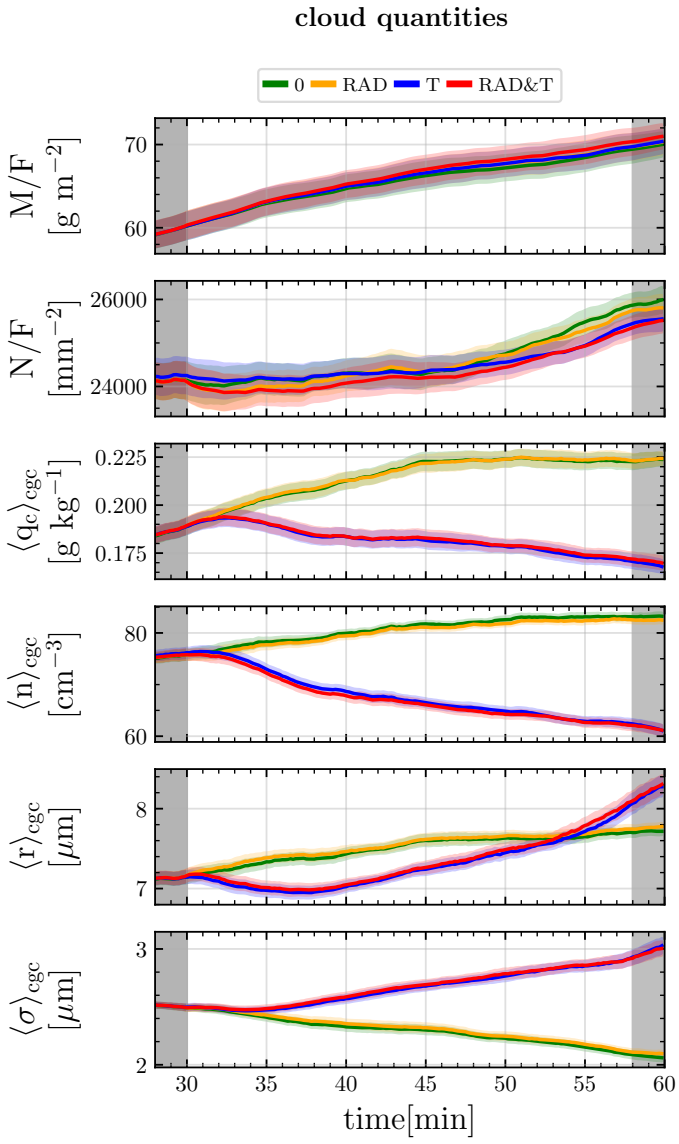

Figure 5.10: The time series data of PALM LES stratus cloud simulations, which compare the 0, RAD, T and RAD&T parametrizations, that consider turbulence and/or radiation in the diffusional growth Eq. (3.8). The parametrizations are switched on after 30 min. M/F and N/F show the total water mass and total number of droplets in the atmosphere each over the LES domain surface area F. The superdroplets per grid cell are set to $N_{sd} = 10^3$ with large droplet splitting. The averages are evaluated according to the Table (5.1). The time series error shows the standard deviation of the mean estimator function for at least 20 ensemble runs Eq. (3.21). The gray shaded regions <30 and >58 min indicate the spin up period and the 2 min evaluation period of the mean values summarized in the Tables (5.4) and (5.5).

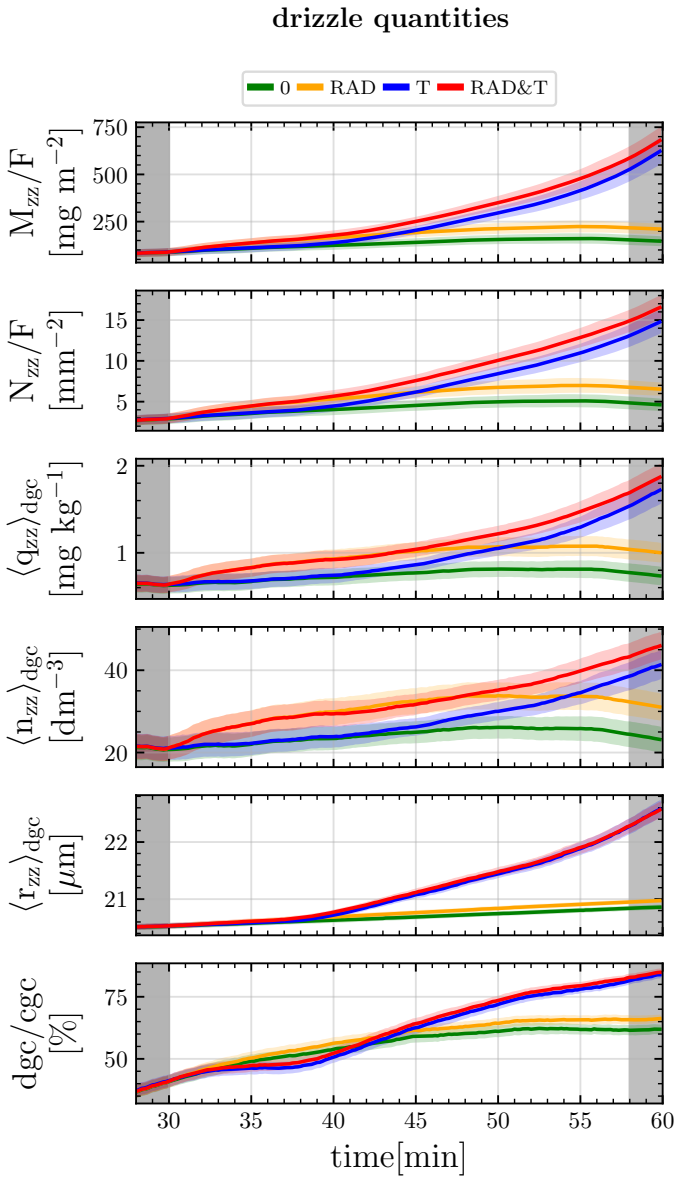

Figure 5.11: M_{zz}/F and N_{zz}/F show the total drizzle mass and total number of drizzle droplets in the atmosphere each over the LES domain surface area F. For further information take a look at the caption of the Figure 5.10.

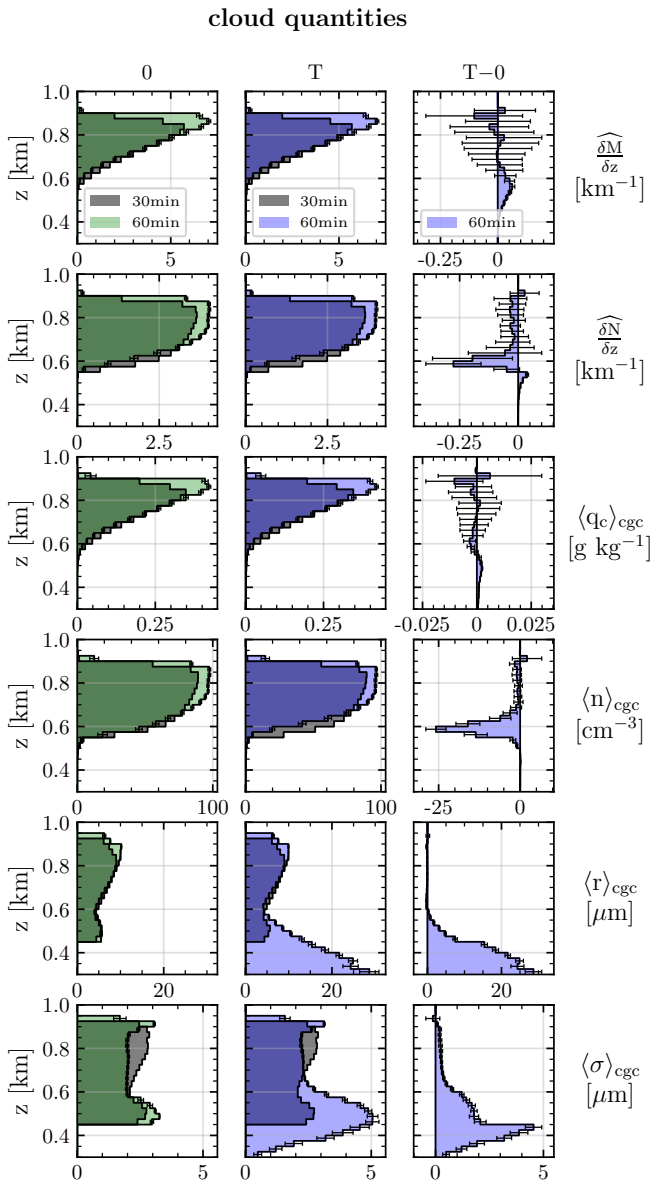

Figure 5.12: The profiles of cloud quantities from PALM LES stratus simulations, that are averaged over a 2 min interval and ensemble runs. The plots with $\widehat{\delta M/\delta z}$ and $\widehat{\delta N/\delta z}$ show the vertical normalized distribution of the total water mass and cloud droplet number. $\langle q_c \rangle_{cgc}$, $\langle n \rangle_{cgc}$, $\langle r \rangle_{cgc}$ and $\langle \sigma \rangle_{cgc}$ show the average values of the respective quantity for each model layer over cloudy grid cells (cgc). The panels that show two snapshots of the profiles at 30 and 60 min highlight the temporal evolution for one setup and the panels that show the profiles only at 60 min highlight the difference between parametrizations. The error bars show the standard deviation of the mean estimator function for at least 6 ensemble runs Eq. (3.21). Compared are the simulations with (T) and without (0) the turbulence parametrization. The turbulence is switched on after 30 min. The integrated quantities are normalized with respect to the reference simulation (0) at 30 min according to Eq. (5.4).

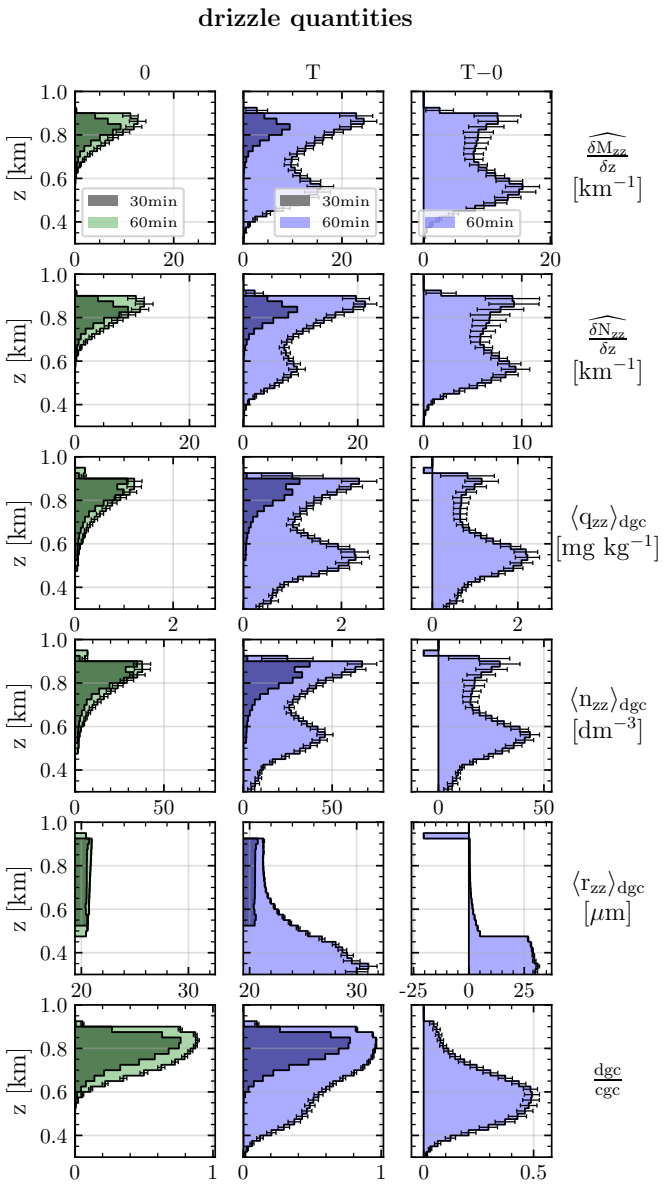

Figure 5.13: The plots with $\widehat{\delta M_{zz}/\delta z}$ and $\widehat{\delta N_{zz}/\delta z}$ show the vertical normalized distribution of the total drizzle mass and drizzle droplet number. $\langle q_{zz}\rangle_{dgc}$, $\langle n_{zz}\rangle_{dgc}$, $\langle r_{zz}\rangle_{dgc}$ and dgc/cgc show the average values of the respective quantity for each model layer over drizzle containing grid cells (dgc). For further information take a look at the caption of the Figure 5.12.

5.1.4 RAD Growth Experiment

The RAD Growth Experiment compares simulations with (RAD) and without (0) the radiative enhanced diffusional growth. The Figures 5.10 and 5.11 show time series results for simulations with and without RAD growth. They also show simulations with and without turbulence, which where discussed in Section 5.1.3. In contrast, the profile Figures 5.14 and 5.15 compare only the 0 and T parametrizations. The research question of the current section is:

> ***What has the larger impact on drizzle formation, turbulence or RAD growth?***

cloud quantities

The time series and profiles in Figure 5.10 and 5.14 for M/F and $\langle q_c \rangle_{cgc}$ show no significant impact from thermal radiation. Only a tendency towards larger values in the cloud center can be made out. The time series for N/F is decreasing by 138.17 mm^{-2} (0.5%) due to radiation. The profiles show, that the decrease is located at the cloud top, with an associated increase in $\delta\widetilde{N_{dry}}/\delta z$ at the cloud top. The same evolution is shown by $\langle n \rangle_{cgc}$, which decreases by -0.7 cm^{-3} (-0.8%) due to radiation. It decreases over the cloud, especially at the cloud top. $\langle r \rangle_{cgc}$ increases by 0.05 μm (0.6%). The profiles show that the increase appears at the cloud top and bottom. In Figure A.2, the quantity $\delta M_{S^*<0}/\delta z$ shows a significant increase of liquid water in subsaturated conditions. The RAD growth allows large droplets at the cloud top to keep growing in subsaturated environments. In this conditions small droplets already start to evaporate. Additionally, the droplets grow to larger sizes and it takes longer to evaporate large droplets due to mixing of dry air into the cloud.

drizzle quantities

The impact on drizzle quantities is stronger than on cloud quantities and the profiles reveal, that the increase in drizzle is located at the cloud top. The time series of M_{zz}/F increases by 128.22 mg m^{-2} (149.4%) over time and by 64.05 mg m^{-2} (42.7%) due to radiation. N_{zz}/F increases by 3.82 mm^{-2} (135.1%) over time and by 1.91 mm^{-2} (40.4%) due to radiation. Similarly, the time series of $\langle q_{zz} \rangle_{dgc}$ increase by 0.38 mg kg^{-1} (59.3%) over time and by 0.27 mg kg^{-1} (35.4%) due to radiation. $\langle n_{zz} \rangle_{dgc}$ increase by 10.52 dm^{-3} (49.6%) over time and by 7.89 dm^{-3} (33.1%) due to radiation.

summary

Simulations with RAD growth show an increase of 50% in drizzle liquid water and drizzle droplet number. This on the order of the impact of the Thermal Cooling Experiment. Therefore, RAD growth can not be neglected, but the increase is smaller then from the turbulence parametrization.

		$\Delta_t 0$	(%)	Δ_tRAD	(%)	RAD-0	(%)
M/F	[g m^{-2}]	10.04	(16.8)	10.3	(17.2)	0.31	(0.4)
N/F	[mm^{-2}]	1779.54	(7.4)	1645.89	(6.8)	-138.17	(-0.5)
$\langle q_c \rangle_{cgc}$	[mg kg^{-1}]	37.02	(19.9)	36.87	(19.7)	0.26	(0.1)
$\langle n \rangle_{cgc}$	[cm^{-3}]	7.71	(10.2)	6.91	(9.2)	-0.7	(-0.8)
$\langle r \rangle_{cgc}$	[μm]	0.59	(8.2)	0.62	(8.7)	0.05	(0.6)
$\langle \sigma \rangle_{cgc}$	[μm]	-0.43	(-17.2)	-0.4	(-16.1)	0.03	(1.4)
M_{zz}/F	[mg m^{-2}]	65.4	(77.3)	128.22	(149.4)	64.05	(42.7)
N_{zz}/F	[mm^{-2}]	1.95	(69.8)	3.82	(135.1)	1.91	(40.4)
$\langle q_{zz} \rangle_{dgc}$	[mg kg^{-1}]	0.12	(19.0)	0.38	(59.3)	0.27	(35.4)
$\langle n_{zz} \rangle_{dgc}$	[dm^{-3}]	2.85	(13.6)	10.52	(49.6)	7.89	(33.1)
$\langle r_{zz} \rangle_{dgc}$	[μm]	0.33	(1.6)	0.44	(2.1)	0.11	(0.5)
dgc/cgc		0.23	(59.0)	0.27	(69.0)	0.04	(6.8)

Table 5.5: The summary table of time series data for the comparison of simulations with and without (RAD and 0) the RAD parametrization. The data is averaged over a 2 min time interval after 30 and 60 min and the temporal differences are shown in the Δ_t columns. The RAD-0 column shows the difference between the parametrizations after 60 min. The relative values in percent for the time differences Δ_t are calculated with respect to the reference simulation (0) after 30 min and for the parametrization differences after 60 min.

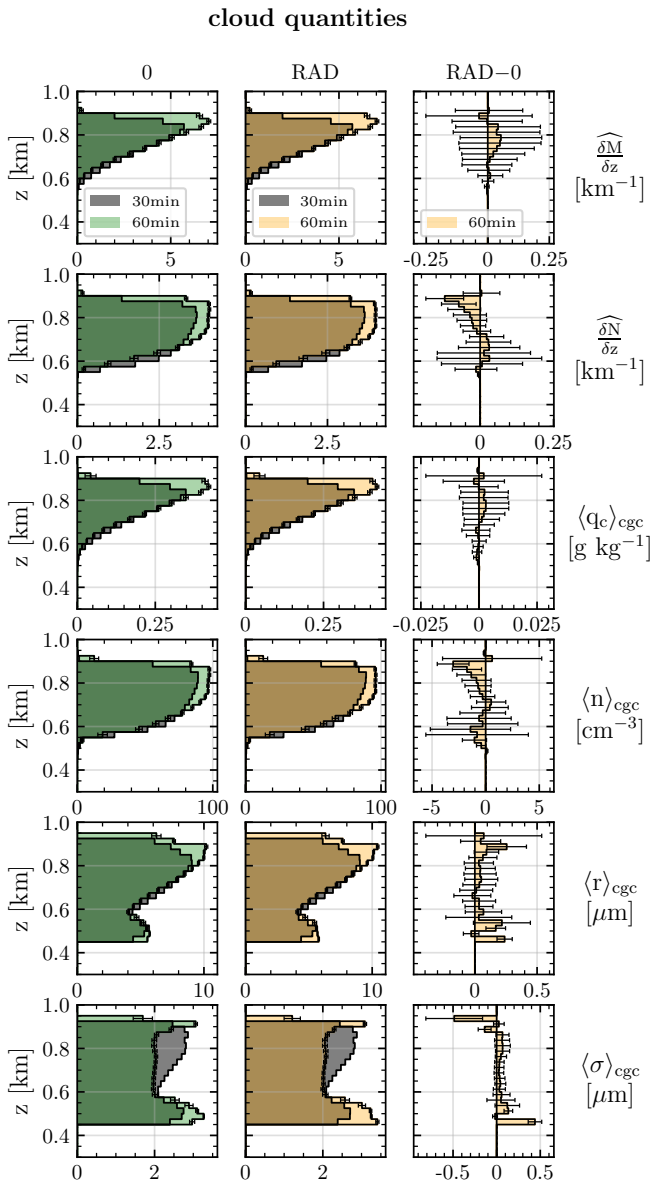

Figure 5.14: The profiles of cloud quantities from PALM LES stratus simulations, that are averaged over a 2 min interval and ensemble runs. The plots with $\widehat{\delta M}/\delta z$ and $\widehat{\delta N}/\delta z$ show the vertical normalized distribution of the total water mass and cloud droplet number. $\langle q_c \rangle_{cgc}$, $\langle n \rangle_{cgc}$, $\langle r \rangle_{cgc}$ and $\langle \sigma \rangle_{cgc}$ show the average values of the respective quantity for each model layer over cloudy grid cells (cgc). The panels that show two snapshots of the profiles at 30 and 60 min highlight the temporal evolution for one setup and the panels that show the profiles only at 60 min highlight the difference between parametrizations. The error bars show the standard deviation of the mean estimator function for at least 6 ensemble runs Eq. (3.21). Compared are the simulations with (RAD) and without (0) the RAD parametrization. The RAD is switched on after 30 min. The integrated quantities are normalized with respect to the reference simulation (0) at 30 min according to Eq. (5.4).

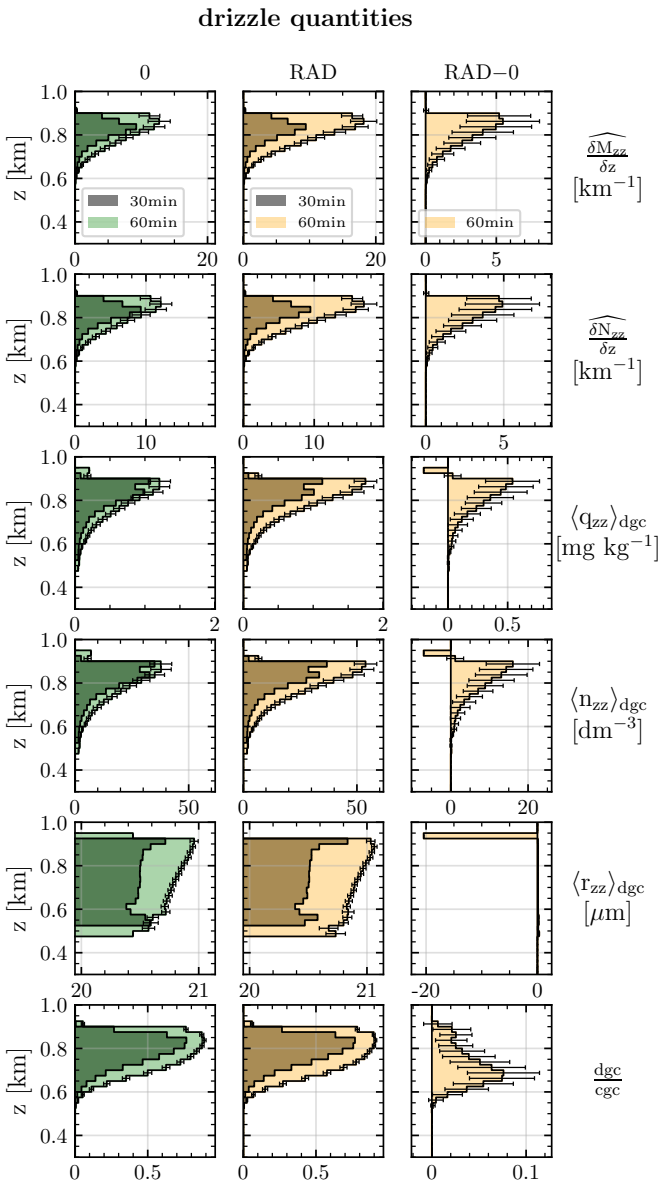

Figure 5.15: The plots with $\widehat{\delta M_{zz}/\delta z}$ and $\widehat{\delta N_{zz}/\delta z}$ show the vertical normalized distribution of the total drizzle mass and drizzle droplet number. $\langle q_{zz}\rangle_{dgc}$, $\langle n_{zz}\rangle_{dgc}$, $\langle r_{zz}\rangle_{dgc}$ and dgc/cgc show the average values of the respective quantity for each model layer over drizzle containing grid cells (dgc). For further information take a look at the caption of the Figure 5.14.

5.1.5 RAD&T Experiment

In this section the combination RAD&T is investigated and compared to T only simulations. Furthermore, the strength of radiation is increased by an arbitrary factor of 3 for the 3RAD&T simulations. The research question in this section is:

Does turbulence increase the impact of RAD growth in LES simulations?

cloud quantities

M/F and N/F show no significant qualitative change in the time series, when comparing RAD&T and T simulations. In general the results are the same as in the RAD section, and changes e.g. a decrease in the droplet number concentration at the cloud top, become only visible for the simulation with 3 times increased thermal radiation strength.

drizzle quantities

The drizzle quantities change for the RAD&T simulation according to: $\frac{M_{zz}}{F}$ increases by 697.5% over time and by 15.1% due to radiation. $\frac{N_{zz}}{F}$ increases by 499.2% over time and by 17.4% due to radiation. $\langle q_{zz} \rangle_{dgc}$ increases by 179.3% over time and by 10% due to radiation. $\langle n_{zz} \rangle_{dgc}$ increases by 110.5% over time and by 11.18% due to radiation.

The drizzle quantities increase for the 3RAD&T simulation according to: $\frac{M_{zz}}{F}$ increases by 1116.6% over time and by 76% due to radiation. $\frac{N_{zz}}{F}$ increases by 863.5% over time and by 89.3% due to radiation. $\langle q_{zz} \rangle_{dgc}$ increases by 321.4% over time and by 66.5% due to radiation. $\langle n_{zz} \rangle_{dgc}$ increases by 234.1% over time and by 77.9% due to radiation.

summary

The increase in drizzle water content from RAD growth is 86.43 with and 64.05 mg m^{-2} without turbulence. Therefore, the turbulence increases the impact of thermal radiation by 35 %. However, the impact of the combination is smaller then in the parcel model simulations.

		Δ_tT	(%)	Δ_tRAD&T	(%)	RAD&T-T	(%)	Δ_t3RAD&T	(%)	3RAD&T-T	(%)
M/F	[g m^{-2}]	10.37	(17.4)	9.8	(16.5)	-0.78	(-1.1)	10.79	(18.1)	0.22	(0.3)
N/F	[mm^{-2}]	1269.4	(5.2)	1222.99	(5.1)	-132.73	(-0.5)	886.29	(3.7)	-472.28	(-1.9)
$\langle q_c \rangle_{cgc}$	[mg kg^{-1}]	-17.15	(-9.2)	-21.98	(-11.8)	-4.83	(-2.9)	-19.43	(-10.4)	-2.26	(-1.3)
$\langle n \rangle_{cgc}$	[cm^{-3}]	-14.06	(-18.5)	-15.39	(-20.3)	-1.24	(-2.0)	-16.11	(-21.2)	-1.98	(-3.2)
$\langle r \rangle_{cgc}$	[μm]	1.05	(14.7)	1.11	(15.6)	0.05	(0.6)	1.07	(15.1)	0.02	(0.2)
$\langle \sigma \rangle_{cgc}$	[μm]	0.47	(18.8)	0.53	(21.2)	0.07	(2.2)	0.54	(21.6)	0.08	(2.5)
M_{zz}/F	[mg m^{-2}]	487.44	(563.3)	577.6	(697.5)	86.43	(15.1)	927.37	(1116.6)	436.45	(76.0)
N_{zz}/F	[mm^{-2}]	11.08	(388.4)	13.62	(499.2)	2.42	(17.4)	23.63	(863.5)	12.44	(89.3)
$\langle q_{zz} \rangle_{dgc}$	[mg kg^{-1}]	0.99	(153.2)	1.15	(179.3)	0.16	(10.0)	2.07	(321.4)	1.08	(66.5)
$\langle n_{zz} \rangle_{dgc}$	[dm^{-3}]	18.68	(87.8)	23.45	(110.5)	4.71	(11.8)	49.81	(234.1)	31.13	(77.9)
$\langle r_{zz} \rangle_{dgc}$	[μm]	1.9	(9.3)	2.02	(9.8)	0.1	(0.4)	1.97	(9.6)	0.05	(0.2)
dgc/cgc		0.43	(110.5)	0.46	(117.8)	0.02	(2.3)	0.48	(123.8)	0.04	(5.2)

Table 5.6: Summary of differences for 2 minutes averaged values between the time points at 30 and 60 minutes (indicated by Δ_t) and between parametrizations at 60 minutes (else). The turbulent simulation T is taken as the reference. See the corresponding Figures 5.16 and 5.17.

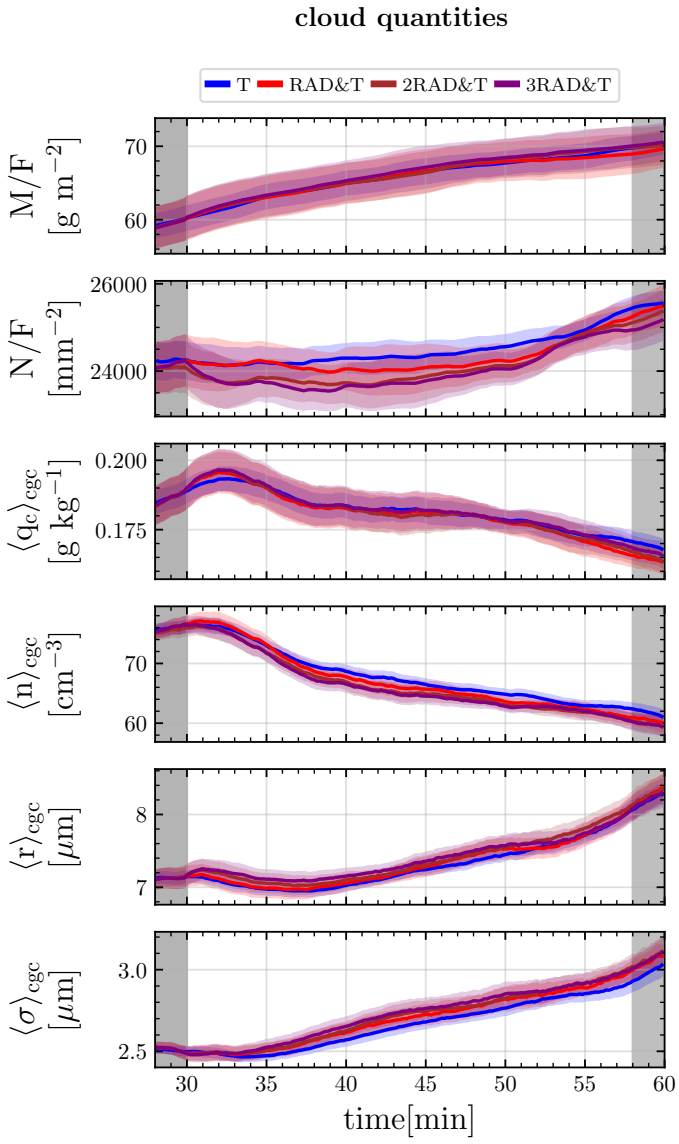

Figure 5.16: Time series of cloud quantities of PALM LES stratus simulations, which compare the T, RAD&T, 2RAD&T and 3RAD&T parametrizations, that consider turbulence and a increasing strength of radiation (by a factor of 2 and 3) in the diffusional growth Eq. (3.8). The parametrizations are switched on after a spin up period of 30 minutes. M/F and N/F show the total water mass and total number of droplets in the atmosphere each over the LES domain surface area F. The averages are evaluated according to the Table (5.1). The uncertainties to the data points shows the standard deviation of the mean estimator function for at least 10 ensemble runs Eq. (3.21). The gray shaded regions at t<30 and >55 minutes indicate the 2 minutes period, over which the results of the Table (5.6) are calculated.

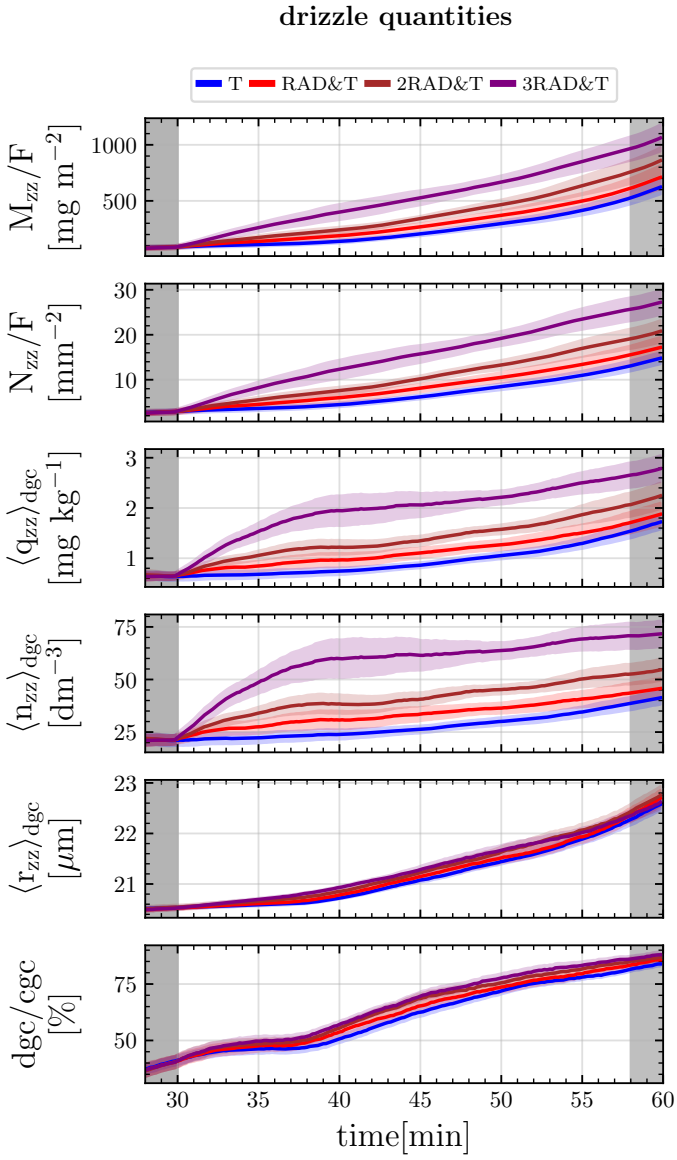

Figure 5.17: M_{zz}/F and N_{zz}/F show the total drizzle mass and total number of drizzle droplets in the atmosphere each over the LES domain surface area F. See the caption of the Figure 5.17.

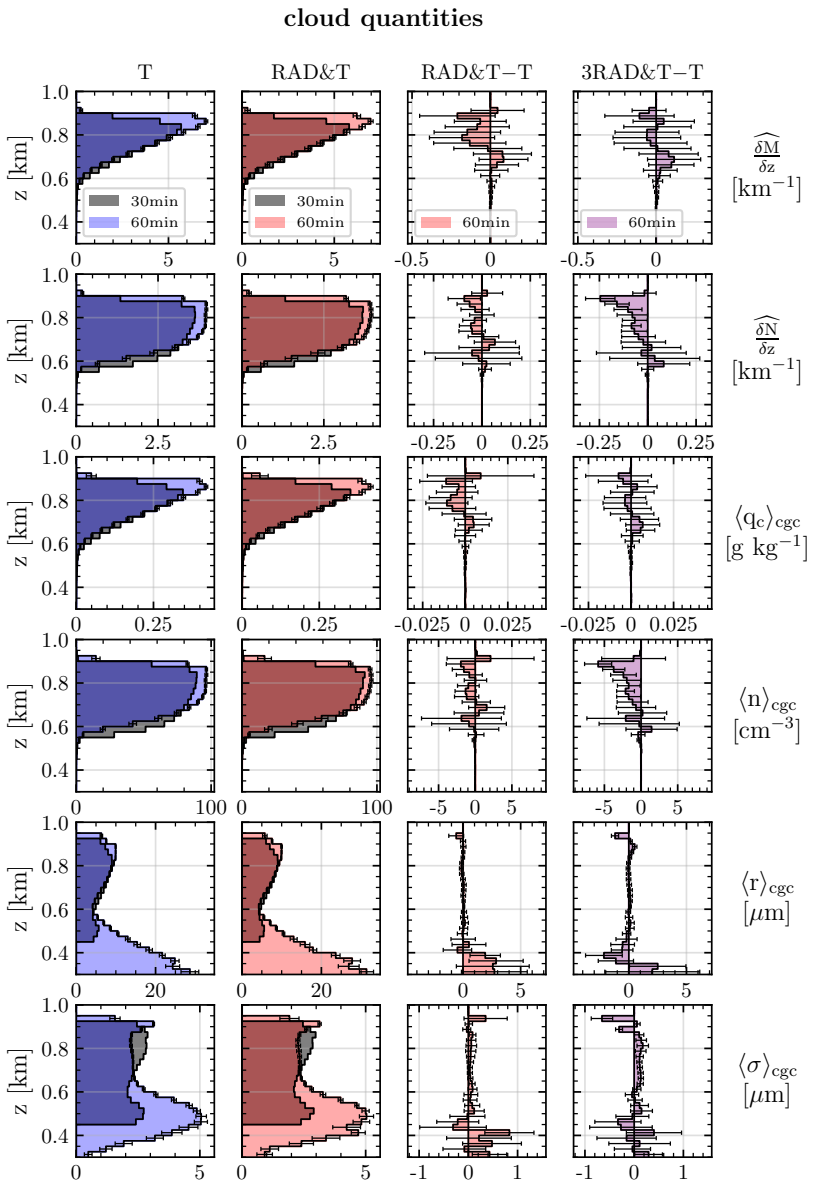

Figure 5.18: Cloud quantity profiles, that compare between two time points (left) and between parametrizations (right). The plots with $\widehat{\delta M}/\delta z$ and $\widehat{\delta N}/\delta z$ show the vertical normalized distribution of the total water mass and cloud droplet number. $\langle q_c \rangle_{cgc}$, $\langle n \rangle_{cgc}$, $\langle r \rangle_{cgc}$ and $\langle \sigma \rangle_{cgc}$ show the average values of the respective quantity for each model layer over cloudy grid cells (cgc). The integrated quantities are normalized to the T simulation after 30 minutes. See the caption of the Figure 5.16.

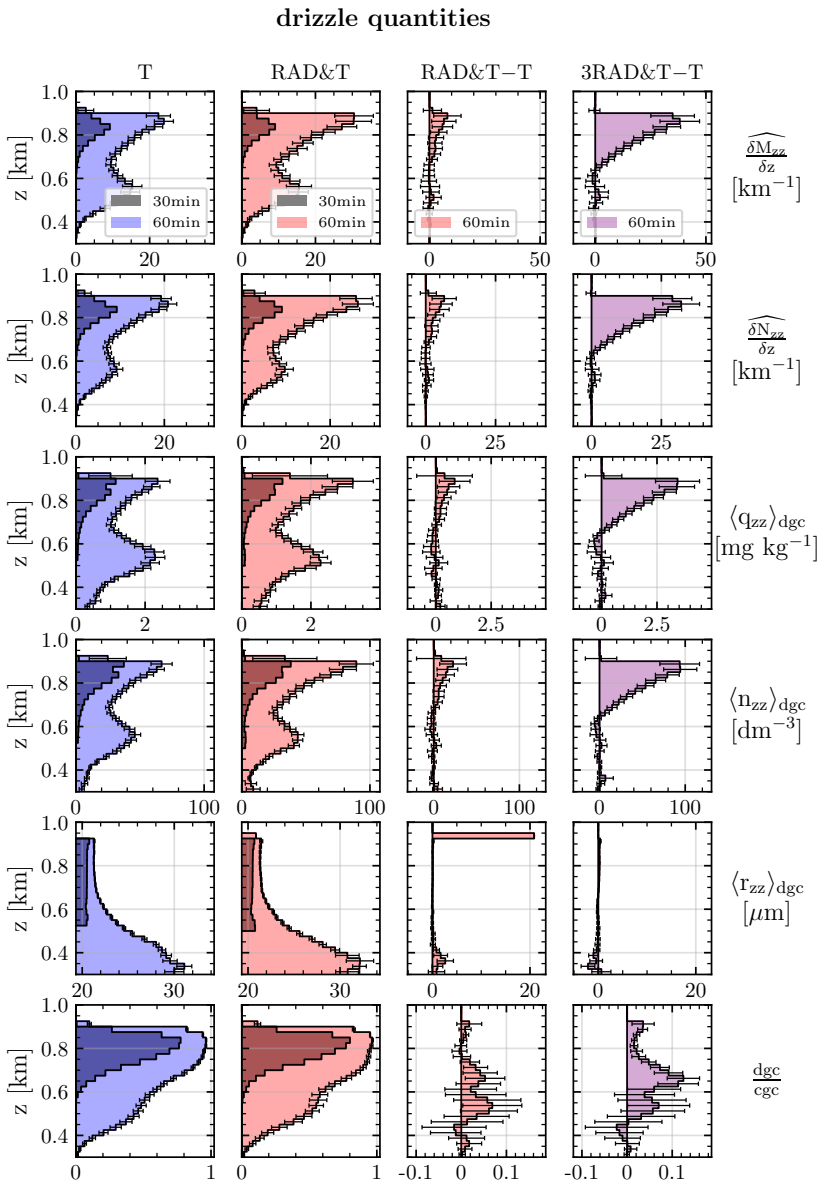

Figure 5.19: The plots with $\widehat{\delta M_{zz}/\delta z}$ and $\widehat{\delta N_{zz}/\delta z}$ show the vertical normalized distribution of the total drizzle mass and drizzle droplet number. $\langle q_{zz}\rangle_{dgc}$, $\langle n_{zz}\rangle_{dgc}$, $\langle r_{zz}\rangle_{dgc}$ and dgc/cgc show the average values of the respective quantity for each model layer over drizzle containing grid cells (dgc). See the caption of the Figure 5.16 and 5.18.

Chapter 6

Discussion

6.1 Parcel Model

The discussion of the parcel model is published in Barekzai and Mayer (2020).

The investigation of the turbulent parcel model shows the following results: Cooling by the emission of thermal radiation can cause a doubling of the droplet size standard deviation, with particularly strong effects in combination with turbulence (Fig. 4.3). The updraft sensitivity shows that turbulence and RAD are more important at small updraft speeds with approximately equal contributions to the standard deviation (Fig. 4.5). Furthermore, the longer the radiation can operate, the larger the impact. It even becomes the dominant contributor to the droplet size standard deviation, for slowly developing clouds with w=0.01 m s^{-1} (Fig. 4.6). Radiation acts as a secondary nucleation inhibitor, due to the subsaturated environment, which suppresses the nucleation of cloud droplets.
Finally, the results for the collision initiation timescale suggest that thermal radiation may play a role in bridging the Condensation Coalescence Bottleneck by increasing the droplet size standard deviation and accelerating the creation of larger droplets.
The simple parcel model allows fast studies which illustrate the dependencies of a number of parameters. In comparison, LES simulations are more expensive and introduce complexity, which requires additional statistical analysis. Nevertheless, the simplistic approach comes with limitations and in the following some possible issues are highlighted and an outlook on subsequent work is given.
Sedimentation is not included. All droplets stay in the parcel, if they do not completely evaporate. An estimate of droplet fall speeds using Stokes approximation shows that droplets with radius of 10 and 20 μm would have fallen 10 and 50 m in 15 min. This is suggesting that sedimentation can be neglected for the time period of 15 min, but longer simulations may become increasingly unrealistic without sedimentation. The sedimentation analysis of the parcel simulations can be found in the section 4.1.6. Additionally, the secondary nucleation process depends on RAD and turbulence, which has the most impact

for low updraft speeds. The dependence is not separately evaluated here, but details can be found in Marquis and Harrington (2005). Furthermore, the statistics of the turbulence parametrization is kept constant while changing the updraft speed from 0.01 m s^{-1} to 1.5 m s^{-1}. The saturation and corresponding updraft fluctuations for ϵ=10 cm^2 s^{-3} and ϵ=50 cm^2 s^{-3} are based on stratocumulus cloud top and shallow cumulus core cases. de Lozar and Mellado (2015a) showed that cloud top regions of stratiform clouds have updraft speed fluctuations similar to those of a shallow cumulus cloud base. There are uncertainties with respect to turbulence which may be due to unresolved scale interactions or dependence on atmospheric composition. Furthermore, turbulent mixing of moist and dry air is neglected, even though it is a very important process at the cloud edges. The correlation of dry downdrafts and wet updrafts may result in even larger saturation fluctuations. Finally, the parcel position is kept at cloud top, which might be unrealistic, but serves as a maximal impact scenario for thermal radiation. The current simple approach can be investigated without explicitly solving the radiative transfer equation and serves as a baseline for more complicated scenarios. The next step will be to run RAD and the turbulence parametrization in LES simulations with resolved radiation. In a LES, the saturation fluctuations can be calculated with the prognostic subgrid turbulent kinetic energy. The positions of the droplets inside the scene will be resolved, as well the cloud edges with realistic radiative cooling rates (e.g. Jakub and Mayer (2015)). Alternatively, it would be interesting to investigate the impact of radiative cooling on ice clouds, because turbulence decreases with height and thermal radiation is transmitted more effectively to space.

6.2 LES Model

The Superdroplet Convergence Experiment 5.1.1 shows the improvement of the drizzle representation due to the addition of a droplet splitting algorithm. Simulations can be run with only 10^3 superdroplets per grid cell and still give a accurate representation of microphysical. The profiles show, that the cloud edges are the sensitive cloud regions with respect to the number of superdroplets, concerning the correct representation of the formation of drizzle droplets. The results confirm the importance of the splitting approach as stated in Schwenkel et al. (2018)

The Radiative Heat Experiment 5.1.2 removes the thermal radiative feedback on the temperature field. Therefore, the liquid cloud water content decreases, due to the lack of radiative cooling driven condensation at the cloud top. The drizzle water content for simulations without radiation decreases by 98.2 mg m^{-2} (65.4%), mostly at the cloud top. The profiles show that, the subgrid kinetic energy reduces with height for simulations without thermal radiation and vanishes over the extent of the cloud. Cloud top entrainment driven by evaporative and radiative cooling is an important process investigated in many studies (Stevens et al., 2005; de Lozar and Mellado, 2015b; Mellado, 2017). In the current analysis, the direct impact of radiative driven cloud top entrainment is measured with the impact on cloud top drizzle production, which has not been shown yet.

The Turbulence Experiment 5.1.3 reveals that saturation fluctuations increase the drizzle production significantly by 424 mg m^{-2} (282.7%). Additionally to the cloud top, drizzle is produced in significant quantity at the cloud bottom. This highlights the role of all cloud edges in the process of forming drizzle. In general, the impact of turbulence should decrease with height, as the atmosphere becomes more stable. The SGS kinetic energy, a prognostic variable of the LES, enters the saturation fluctuations parametrization and decreases with height as shown in A.1. This may also influence the creation of drizzle at the cloud bottom. The results are in accordance with previous studies (Grabowski and Abade, 2017b; Abade et al., 2018), that show an significant broadening of the droplet distribution due to turbulence. The quantitative results on the drizzle mass and the potentially importance of the cloud bottom have not been shown yet. Further theoretical and experimental investigations may validate the role of the cloud bottom in the drizzle production.

The RAD Experiment 5.1.4 shows that RAD growth further increases drizzle formation at the cloud top by 64.05 mg m^{-2} (42.7%).

The RAD&T Experiment 5.1.5 shows, that for the combination of thermal radiation and turbulence, the drizzle formation increases by 86.43 mg m^{-2} (15.1%). In contrast to the other experiments, here, the turbulent simulation is taken as reference. The absolute increase in drizzle water content from adding RAD is similar to that from the coupling of the radiative heating rates to the temperature field. Furthermore, with a radiative cooling that is increased by a factor of 3, the drizzle water content increases by 436.45 mg m^{-2} (76%), which is similar in magnitude to the increase from the turbulence parametrization. The role of radiative cooling on the drizzle production has been investigated in Klinger et al. (2019). The study could not establish statistical significance in the radiative feedback, which is done in the present analysis by investigating a set of up to 20 ensemble simulations for each profile and time series.

The RAD growth parametrization increases the drizzle formation. The impact further increases if combined with saturation fluctuations. Furthermore, the impact of RAD on the drizzle water content is with 64 mg m^{-2} in magnitude similar to the coupling of thermal radiation heating rates to the temperature field with 98 mg m^{-2}. In comparison to the impact of saturation fluctuations on the drizzle water content is with 424 mg m^{-2} much larger. The increase due to RAD growth becomes similar in magnitude to the increase from the turbulence parametrization, if thermal radiation is increased by a factor of 3 (3RAD&T) leading to an increase of 436 mg m^{-2}.

6.3 Conclusion and Outlook

The starting point for the conclusions should be the initially stated research question:

> ***Can thermal radiation in combination with unresolved turbulence explain the formation of rain in ice free clouds?***

The parcel and the LES simulations show, that thermal radiation and unresolved turbulence have an significant impact on the droplet distribution and accelerate the drizzle creation timescale. Therefore, both can not be neglected. In comparison, the increased drizzle production due to unresolved turbulence is stronger then from thermal radiation, in both experimental setups. The LES simulations with turbulence also show a significant amount of drizzle at the cloud bottom. In parcel simulations, thermal radiation leads to slightly subsaturated atmospheric conditions. As a result, smaller droplets start to evaporate. This reduces the droplet number and supports the creation of drizzle. The impact is amplified by including the moisture fluctuations from the unresolved turbulence. However, in dynamic LES simulations, the impact due to the intaraction of both parametrizations is smaller. The moisture field and the droplet trajectories are less stronly coupled. Finally, drizzle is not yet rain and to eliminate any uncertainty, simulations with explicit collision parametrization should be carried out. The resulting rain timescales should be compared to observations. Furthermore, to provide a more general answer to this question, simulations for different cloud types must be evaluated and compared, to estimate the impact of cloud sides and the dynamical state of the atmosphere.

In the current setup, the ground fluxes of sensible and latent heat are set to zero to reduce complexity. The evolution of the clouds is therefore decoupled from the ground. More elaborated and realistic simulations should apply adequate ground fluxes, which will increase the spin up period and therefore overall simulation time.

In general, high resolution simulations depend on the time stepping approach Barrett et al. (2019). In the current setup, a fixed time step of 1 s is used, but to put the results on stronger grounds a time step convergence study could be carried out. A possible side effect of a large superdroplet number may be a faster convergence with respect to the time step.

In stratus simulations, the cloud droplets are continuously activating and deactivating, especially at the cloud center. However, the current setup neglects droplet activation as recommended by Hoffmann et al. (2015). One could argue, that the role of the activation process may be important in the current study due to the frequent renucleation of droplets. Furthermore, the stratus cloud will change the aerosol distribution by the process of nucleation and denucleation and also by collisions. An interesting question is: How might an explicit nucleation approach used in Abade et al. (2018) might change the cloud and aerosol evolution? Here, also longer simulations seem more interesting.

Furthermore, solar radiation should be included and combined with thermal simulations. Also, longer simulation times should be investigated to further evaluate the stratocumu-

lus cloud systems. A more realistic approach to radiation may include a diurnal cycle in the solar irradiance. Furthermore, 3D radiation should be investigated, as it takes into account of the cloud sides. Changes in the background profiles may facilitate the comparison to previous studies of Harrington et al. (2000), which investigate summer time arctic stratus clouds, presented in Curry (1986). The described profiles, show a similar measured inversion structure as the used DYCOMS-II case, but with different water vapor and temperatures levels.

A broader understanding of the simulations could be achieved by sensitivity studies with respect to the initial aerosol number concentration or the vertical resolution. Although (Stevens et al., 2005) propose a vertical grid spacing of 5 m it is still unclear, if the process of cloud top entrainment has converged. (Hartman and Harrington, 2005b) show that the results may also strongly depend on the droplet number concentration. The simulation setup might be changed to investigate the development of cumulus clouds. As a first step, cumulus clouds should be initialized with ideal and reproducible warm bubble simulations and after that with free evolving simulations from cumulus cases like RICO or BOMEX (Rauber et al., 2007; Jiang and Cotton, 2000). Furthermore, the impact of thermal radiation on the development of the cloud should increase with cloud height, as shown in Fig. 3.3. Therefore, cirrus clouds should be studied, which implies the usage of a more complex and uncertain ice microphysics. For those high clouds, the atmosphere is also more stable, reducing the impact of turbulence.

A sophisticated analysis of drizzle droplet trajectories might bring light in the details of the process and help interpreting the current results. An attempt was made in Klinger et al. (2019) by following parcel trajectories based on the parcels time spend at cloud top and sides, but the superdroplet approach allows to specifically focus on the droplet trajectories that result in drizzle droplets. Lagrangian microphysics will become very expensive, if collisions are included. Depending on the paradigm, the number of superdroplets may increase drastically and each superdroplet must be aware of its nearest neighbors. To circumvent the challenges of explicit collisions in the LES, the profiles can be used with a external collision model to post process the impact on rain formation timescale.

Furthermore, the radiative solver may be coupled to the resolved droplet distribution and not the averaged grid cell quantities and the coupling of RAD growth to the droplets may be calculated with Mie theory, compared to the current geometrical optics approach.

symbol	description	symbol	description
A&D	parameter of Eq. (3.8)	ρ_w	density of water with 10^3 kg m^{-3}
a_1	constant from Squires (1952) with $3 \cdot 10^{-4}$ m^{-1}	ρ_{NaCl}	density of sodium chloride with 2160 kg m^{-3}
B(λ, T)	Planck's function	q_v	water vapor mixing ratio in kg kg^{-1}
c_p	specific heat of air at const. pressure 1003.5 J kg^{-1} K^{-1}	$\mathcal{R}$	net radiative flux per droplet surface area in W m^{-2}
C_1&C_2	parameter of Eq. (3.5), defined by Eq. (3.6)	r_0	radius to distinguish the droplet distribution tail
D_w	water vapor in air diffusion constant $2.82 \cdot 10^{-5}$ m^2 s^{-1}	r_{cr}	critical radius of nucleation
E	turbulent kinetic energy (Schumann (1991))	r_{dry}	dry radius in μm
ϵ	turbulent dissipation rate in cm^2 s^{-3}	$r_{drizzle}$	embryonic drizzle radius 20 μm
e_s	saturation vapor pressure over flat water surface in Pa	r_i	radius of ith superdroplet in μm
f	radiation modulation factor	r_{sep}	separation radius for which dr/dt=0 in μm
g	gravitational acceleration with 9.81 m s^{-2}	$\langle r \rangle$	mean radius of droplet distribution in μm
γ	surface tension of water at 293 K with 0.0727 N m^{-1}	r_{max}	mean radius of the largest droplets, representing n_{max}
κ	thermal conductivity of air with 0.0243 W m^{-1} K^{-1}	R_v	specific gas constant of water vapor 461.401 J kg^{-1} K^{-1}
L	parcel length scale in m	S^*	supersaturation of the environment
L_v	latent heat of vaporization with $2.257 \cdot 10^6$ J kg^{-1}	S^*_{eq}	equilibrium supersaturation at the droplet surface from Koehler theory
M_w	molar mass of water 0.018 kg mol^{-1}	S^*_{cr}	critical supersaturation for nucleation
M_{NaCl}	molar mass of sodium chloride 0.058 kg mol^{-1}	$S^{*'}_i$	supersaturation fluctuation of the i-th superdroplet
n	droplet number concentration cm^{-3}	σ	standard deviation of the droplet distribution
n_{20} & n_{75}	CCN number concentration of aerosol modes in cm^{-3}	σ_{sb}	Stefan Boltzmann constant with $5.67 \cdot 10^{-8}$ W m^{-2} K^{-4}
n_{ccn}	CCN number concentration cm^{-3}	t&dt	simulation time and time step of 0.2 in s
$n_{drizzle}$	embryonic drizzle number concentration 10^{-3} cm^{-3} (Feingold and Chuang (2002))	T	environment temperature in Kelvin
n_{max}	used embryonic drizzle number concentration 10^{-1} cm^{-3}	T_{drop}	droplet temperature in Kelvin
N_i	represented number density per superdroplet: 10^3 m^{-3}	τ_{relax}	relaxation time scale of q_v due to the droplet distribution in s from Squires (1952)
N_{sd}	number of superdroplets per parcel 10^5	τ	turbulent time scale (Schumann (1991))
p	pressure in Pa	w & w'_i	vertical wind and fluctuations in m s^{-1}
ρ_0	air density 1 kg m^{-3} (shallow convection approx.)	χ	normal distributed random variable

Table 6.1: Used symbols and descriptions for variables and constants.

symbol	description
α_λ	absorbtivity of radiation from a body
B(T)	Planck's law
β_{sca}, β_{abs}, β_{ext}	scatterting, absorption and extinction coefficient
E_{up}, E_{dn}, E_{net}	up, downwards and netto irradiance
E_e	irradiance
$E(r, r')$	collision efficiencies of the hall kernel
E_ν	photon energy of frequency ν
ϵ_λ	emissivity of radiation from a body
∇E_{cld}, ∇E_{atm}	radiative flux divergence from the cloud and atmosphere
h	Planck's constant $h = 6.626 \cdot 10^{-34}$ J s
$K(r, r')$	hall collision kernel
L_e	radiance
lwc, lwp	liquid water content and path
μ	viscosity
μ_θ	cosine of zenith angle
P_e	scattering phase function of the atmosphere
P_k	power of turbulent motion with wavenumber k
Φ	zenith angle
Φ_e	the radiant flux
R_d	specific gas constant for air 287 J kg^{-1} K^{-1}
$\overline{\rho}$	mean density
σ_{sca}, σ_{abs}	scattering and absorption cross section
θ	azimut angle
τ	optical thickness
$\vec{u}$	fluid velocity field
$\vec{\omega}$	vector of earths angular velocity
Ω	solid angle

Table 6.2: Additional symbols and descriptions for variables and constants.

Appendix A

Appendix

Additional figures from the Section 5 showing environment quantities for the Turbulence and the RAD Growth Experiment.

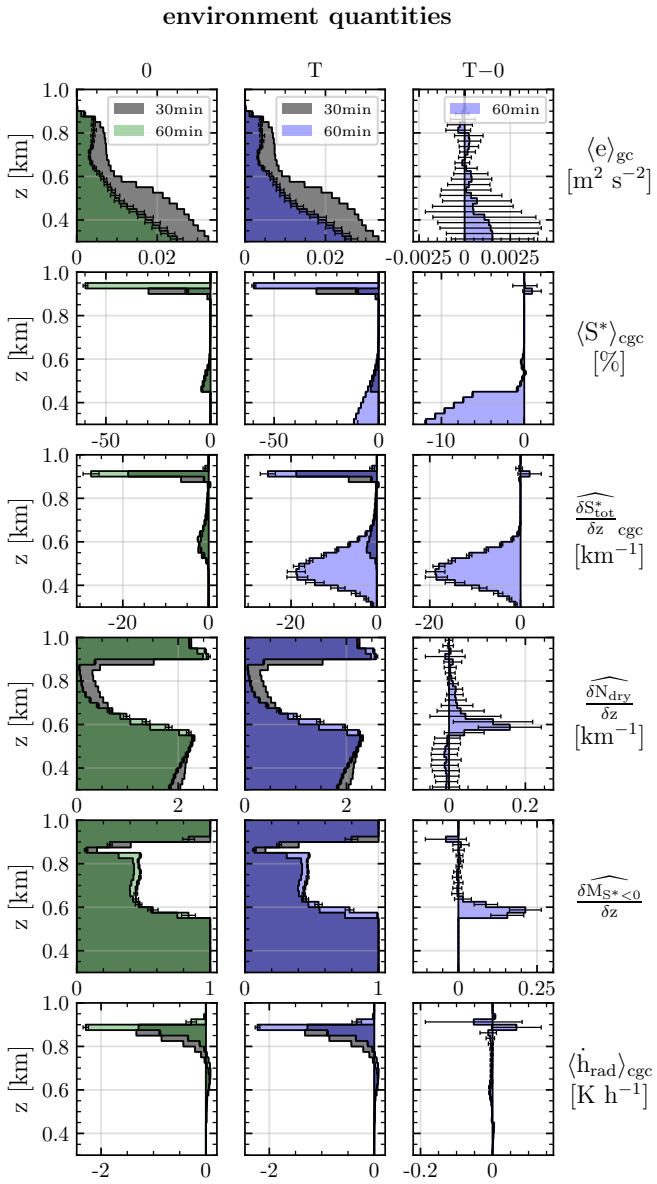

Figure A.1: The profiles of environment quantities. For further information take a look at the caption of the Figure 5.12.

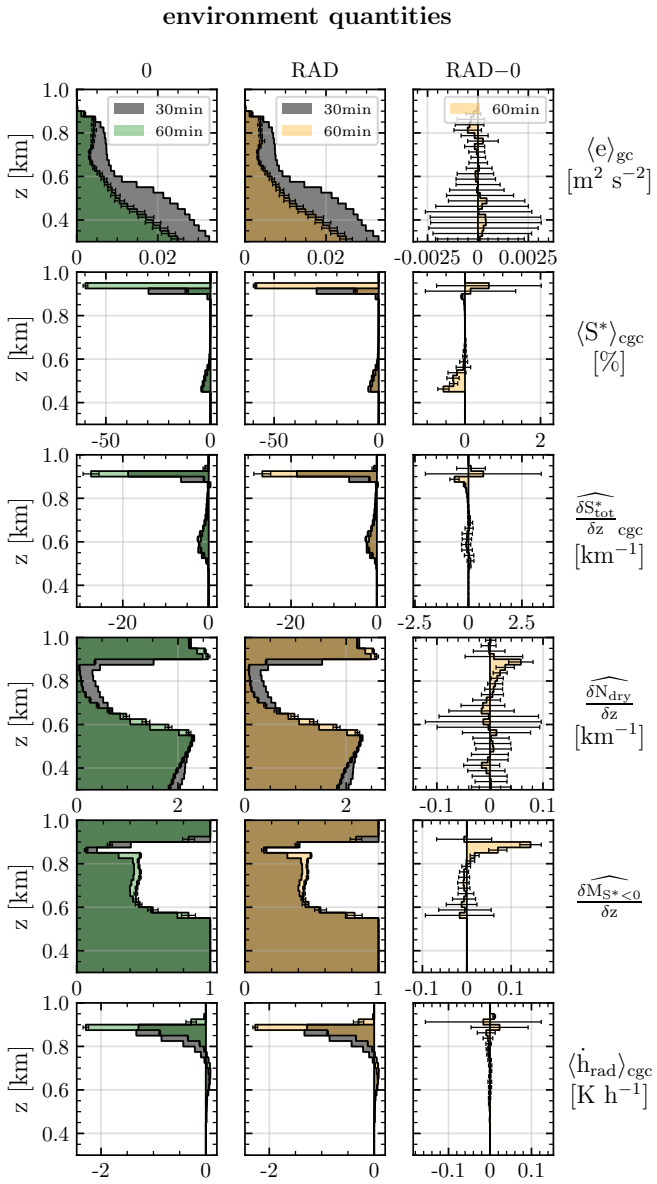

Figure A.2: The profiles of environment quantities. For further information take a look at the caption of the Figure 5.14.

Bibliography

(1950). Radiative transfer. by s. chandrasekhar. london (oxford university press) 1950. 8vo. pp. 393, 35 figures. 35s. *Quarterly Journal of the Royal Meteorological Society*, 76(330):498–498.

Abade, G. C., Grabowski, W. W., and Pawlowska, H. (2018). Broadening of cloud droplet spectra through eddy hopping: Turbulent entraining parcel simulations. *Journal of the Atmospheric Sciences*, 75(10):3365–3379.

Alduchov, O. A. and Eskridge, R. E. (1996). Improved magnus form approximation of saturation vapor pressure. *Journal of applied meteorology*, 35(4):601–609.

Anderson, G. P., Clough, S. A., Kneizys, F. X., Chetwynd, J. H., and Shettle, E. P. (1986). Afgl atmospheric constituent profiles (0.120km). *Air Force Geophysics Laboratory*.

Andreae, M. and Rosenfeld, D. (2008). Aerosol–cloud–precipitation interactions. part 1. the nature and sources of cloud-active aerosols. *Earth-Science Reviews*, 89(1-2):13–41.

Andrejczuk, M., Reisner, J. M., Henson, B., Dubey, M. K., and Jeffery, C. A. (2008). The potential impacts of pollution on a nondrizzling stratus deck: Does aerosol number matter more than type? *Journal of Geophysical Research: Atmospheres*, 113(D19).

Barekzai, M. and Mayer, B. (2020). Broadening of the cloud droplet size distribution due to thermal radiative cooling: Turbulent parcel simulations. *Journal of the Atmospheric Sciences*, 77(6):1993–2010.

Barrett, A. I., Wellmann, C., Seifert, A., Hoose, C., Vogel, B., and Kunz, M. (2019). One step at a time: How model time step significantly affects convection-permitting simulations. *Journal of Advances in Modeling Earth Systems*, 11(3):641–658.

Beard, K. V. and Ochs III, H. T. (1993). Warm-rain initiation: An overview of microphysical mechanisms. *Journal of Applied Meteorology*, 32(4):608–625.

Beer, A. (1852). Bestimmung der absorption des rothen lichts in farbigen flussigkeiten. *Ann. Physik*, 162:78–88.

Betts, A. (1973). Non-precipitating cumulus convection and its parameterization. *Quarterly Journal of the Royal Meteorological Society*, 99(419):178–196.

Bouguer, P. (1729). *Essai d'optique sur la gradation de la lumière*. chez Claude Jombert, ruë S. Jacques, au coin de la ruë des Mathurins, à l ....

Brenguier, J.-L. and Chaumat, L. (2000). Droplet spectra broadening in cumulus clouds. part i: Broadening in adiabatic cores. *Journal of the Atmospheric Sciences*, 58(6):628–641.

Brenguier, J.-L. and Chaumat, L. (2001). Droplet spectra broadening in cumulus clouds. part i: Broadening in adiabatic cores. *Journal of the atmospheric sciences*, 58(6):628–641.

Brewster, M. (2015). Evaporation and condensation of water mist/cloud droplets with thermal radiation. *International Journal of Heat and Mass Transfer*, 88:695 – 712.

Brown, R. and Roach, W. T. (1975). The physics of radiation fog: Ii – a numerical study. *Quarterly Journal of the Royal Meteorological Society*, 102(432):335–354.

Clough, S., Shephard, M., Mlawer, E., Delamere, J., Iacono, M., Cady-Pereira, K., Boukabara, S., and Brown, P. (2005). Atmospheric radiative transfer modeling: a summary of the aer codes. *Journal of Quantitative Spectroscopy and Radiative Transfer*, 91(2):233 – 244.

Cooper, W. A., Lasher-Trapp, S. G., and Blyth, A. M. (2013). The influence of entrainment and mixing on the initial formation of rain in a warm cumulus cloud. *Journal of the Atmospheric Sciences*, 70(6):1727–1743.

Curry, J. A. (1986). Interactions among turbulence, radiation and microphysics in arctic stratus clouds. *Journal of the Atmospheric Sciences*, 43(1):90–106.

de Lozar, A. and Mellado, J. P. (2015a). Mixing driven by radiative and evaporative cooling at the stratocumulus top. *Journal of the Atmospheric Sciences*, 72(12):4681–4700.

de Lozar, A. and Mellado, J. P. (2015b). Mixing driven by radiative and evaporative cooling at the stratocumulus top. *Journal of the Atmospheric Sciences*, 72(12):4681–4700.

Deardorff, J. W. (1973). The Use of Subgrid Transport Equations in a Three-Dimensional Model of Atmospheric Turbulence. *Journal of Fluids Engineering*, 95(3):429–438.

Deardorff, J. W. (1974). Three-dimensional numerical study of the height and mean structure of a heated planetary boundary layer. *Boundary-Layer Meteorology*, pages 1573–1472.

Deardorff, J. W. (1980). Stratocumulus-capped mixed layers derived from a three-dimensional model. *Boundary-Layer Meteorology*, 18(4):495–527.

Duynkerke, P. G. (1991). Radiation fog: A comparison of model simulation with detailed observations. *Monthly Weather Review*, 119(2):324–341.

Einstein, A. (1905). Über einem die erzeugung und verwandlung des lichtes betreffenden heuristischen gesichtspunkt. *Annalen der physik*, 4.

Emde, C., Buras-Schnell, R., Kylling, A., Mayer, B., Gasteiger, J., Hamann, U., Kylling, J., Richter, B., Pause, C., Dowling, T., and Bugliaro, L. (2016). The libradtran software package for radiative transfer calculations (version 2.0.1). *Geoscientific Model Development*, 9(5):1647–1672.

Fan, J., Wang, Y., Rosenfeld, D., and Liu, X. (2016). Review of aerosol–cloud interactions: Mechanisms, significance, and challenges. *Journal of the Atmospheric Sciences*, 73(11):4221–4252.

Feingold, G. and Chuang, P. Y. (2002). Analysis of the influence of film-forming compounds on droplet growth: Implications for cloud microphysical processes and climate. *Journal of the Atmospheric Sciences*, 59(12):2006–2018.

Feingold, G., Cotton, W. R., Kreidenweis, S. M., and Davis, J. T. (1999). The impact of giant cloud condensation nuclei on drizzle formation in stratocumulus: Implications for cloud radiative properties. *Journal of the Atmospheric Sciences*, 56(24):4100–4117.

Fouxon, G. F. A. and Stepanov, M. G. (2002). Acceleration of rain initiation by cloud turbulence. *Nature*, 419.

Franklin, C. N., Vaillancourt, P. A., Yau, M., and Bartello, P. (2005). Collision rates of cloud droplets in turbulent flow. *Journal of the Atmospheric Sciences*, 62(7):2451–2466.

Fu, Q. and Liou, K. N. (1992). On the correlated k-distribution method for radiative transfer in nonhomogeneous atmospheres. *Journal of the Atmospheric Sciences*, 49(22):2139–2156.

Grabowski, W. W. and Abade, G. C. (2017a). Broadening of cloud droplet spectra through eddy hopping: Turbulent adiabatic parcel simulations. *Journal of the Atmospheric Sciences*, 74(5):1485–1493.

Grabowski, W. W. and Abade, G. C. (2017b). Broadening of cloud droplet spectra through eddy hopping: Turbulent adiabatic parcel simulations. *Journal of the Atmospheric Sciences*, 74(5):1485–1493.

Grabowski, W. W., Andrejczuk, M., and Wang, L.-P. (2011). Droplet growth in a bin warm-rain scheme with twomey ccn activation. *Atmospheric Research*, 99(2):290 – 301.

Grabowski, W. W. and Wang, L.-P. (2009). Diffusional and accretional growth of water drops in a rising adiabatic parcel: effects of the turbulent collision kernel. *Atmospheric Chemistry and Physics*, 9(7):2335–2353.

Grabowski, W. W. and Wang, L.-P. (2013). Growth of cloud droplets in a turbulent environment. *Annual Review of Fluid Mechanics*, 45(1):293–324.

Grant, P. W. (2004). A first course in atmospheric radiation. *Madison WI USA: Sundog Publishing*, pages 62–66.

Guzzi, R. and Rizzi, R. (1980). The effect of radiative exchange on the growth by condensation of a population of droplets. *Betr. Phys. Atmos*, 53:351–365.

Hall, W. D. (1980). A detailed microphysical model within a two-dimensional dynamic framework: Model description and preliminary results. *Journal of the Atmospheric Sciences*, 37(11):2486–2507.

Harrington, J. Y., Feingold, G., and Cotton, W. R. (2000). Radiative impacts on the growth of a population of drops within simulated summertime arctic stratus. *Journal of the Atmospheric Sciences*, 57(5):766–785.

Hartman, C. M. and Harrington, J. Y. (2005a). Radiative impacts on the growth of drops within simulated marine stratocumulus. part i: Maximum solar heating. *Journal of the Atmospheric Sciences*, 62:2323–2338.

Hartman, C. M. and Harrington, J. Y. (2005b). Radiative impacts on the growth of drops within simulated marine stratocumulus. part ii: Solar zenith angle variations. *Journal of the Atmospheric Sciences*, 62(7):2339–2351.

Hobbs, P. V. and Rangno, A. L. (1998). Microstructures of low and middle-level clouds over the beaufort sea. *Quarterly Journal of the Royal Meteorological Society*, 124(550):2035–2071.

Hoffmann, F., Noh, Y., and Raasch, S. (2017). The route to raindrop formation in a shallow cumulus cloud simulated by a lagrangian cloud model. *Journal of the Atmospheric Sciences*, 74(7):2125–2142.

Hoffmann, F., Raasch, S., and Noh, Y. (2015). Entrainment of aerosols and their activation in a shallow cumulus cloud studied with a coupled lcm–les approach. *Atmospheric Research*, 156:43 – 57.

Hou, A. Y., Kakar, R. K., Neeck, S., Azarbarzin, A. A., Kummerow, C. D., Kojima, M., Oki, R., Nakamura, K., and Iguchi, T. (2014). The global precipitation measurement mission. *Bulletin of the American Meteorological Society*, 95(5):701–722.

Houghton, H. G. (1938). Problems connected with the condensation and precipitation processes in the atmosphere. *Bulletin of the American Meteorological Society*, 19(4):152–159.

Hudson, J. G. and Yum, S. S. (2001). Maritime–continental drizzle contrasts in small cumuli. *Journal of the Atmospheric Sciences*, 58(8):915–926.

Illingworth, A. J. (1988). The formation of rain in convective clouds. *Nature*, 336.

IPCC (2013). *Climate Change 2013: The Physical Science Basis. Contribution of Working Group I to the Fifth Assessment Report of the Intergovernmental Panel on Climate Change*. Cambridge University Press, Cambridge, United Kingdom and New York, NY, USA.

Jakub, F. and Mayer, B. (2015). A three-dimensional parallel radiative transfer model for atmospheric heating rates for use in cloud resolving models—the tenstream solver. *Journal of Quantitative Spectroscopy and Radiative Transfer*, 163:63 – 71.

Jiang, H. and Cotton, W. R. (2000). Large eddy simulation of shallow cumulus convection during bomex: Sensitivity to microphysics and radiation. *Journal of the Atmospheric Sciences*, 57(4):582–594.

Johnson, D. B. (1982). The role of giant and ultragiant aerosol particles in warm rain initiation. *Journal of the Atmospheric Sciences*, 39(2):448–460.

Jonas, P. (1996). Turbulence and cloud microphysics. *Atmospheric Research*, 40(2):283 – 306. Trophospheric turbulence.

Kim, S.-W., Moeng, C.-H., Weil, J. C., and Barth, M. C. (2005). Lagrangian particle dispersion modeling of the fumigation process using large-eddy simulation. *Journal of the Atmospheric Sciences*, 62(6):1932–1946.

Klinger, C., Feingold, G., and Yamaguchi, T. (2019). Cloud droplet growth in shallow cumulus clouds considering 1-d and 3-d thermal radiative effects. *Atmospheric Chemistry and Physics*, 19(9):6295–6313.

Klinger, C. and Mayer, B. (2016). The neighboring column approximation (nca) – a fast approach for the calculation of 3d thermal heating rates in cloud resolving models. *Journal of Quantitative Spectroscopy and Radiative Transfer*, 168:17 – 28.

Laird, N. F., III, H. T. O., Rauber, R. M., and Miller, L. J. (2000). Initial precipitation formation in warm florida cumulus. *Journal of the Atmospheric Sciences*, 57(22):3740–3751.

Lambert, J. H. (1760). *Photometria sive de mensura et gradibus luminis, colorum et umbrae*. Klett.

Lasher-Trapp, S. G., Cooper, W. A., and Blyth, A. M. (2005). Broadening of droplet size distributions from entrainment and mixing in a cumulus cloud. *Quarterly Journal of the Royal Meteorological Society*, 131(605):195–220.

Lau, K. M. and Wu, H. T. (2003). Warm rain processes over tropical oceans and climate implications. *Geophysical Research Letters*, 30(24):2290.

Lebo, Z. J., Johnson, N. C., and Harrington, J. Y. (2008). Radiative influences on ice crystal and droplet growth within mixed-phase stratus clouds. *Journal of Geophysical Research: Atmospheres*, 113(D9).

Liou, K.-N. (1973). A numerical experiment on chandrasekhar's discrete-ordinate method for radiative transfer: Applications to cloudy and hazy atmospheres. *Journal of the Atmospheric Sciences*, 30(7):1303–1326.

Liu, C. and Zipser, E. J. (2009). "warm rain" in the tropics: Seasonal and regional distributions based on 9 yr of trmm data. *Journal of Climate*, 22(3):767–779.

Maronga, B., Gryschka, M., Heinze, R., Hoffmann, F., Kanani-Sühring, F., Keck, M., Ketelsen, K., Letzel, M. O., Sühring, M., and Raasch, S. (2015). The parallelized large-eddy simulation model (palm) version 4.0 for atmospheric and oceanic flows: model formulation, recent developments, and future perspectives. *Geoscientific Model Development*, 8(8):2515–2551.

Marquis, J. and Harrington, J. Y. (2005). Radiative influences on drop and cloud condensation nuclei equilibrium in stratocumulus. *Journal of Geophysical Research: Atmospheres*, 110(D10):205.

Maxwell, J. C. (1890). On the dynamical theory of gases [1866]. *Maxwell, 77k*, pages 26–78.

Maxwell, J. C. (1996). *A dynamical theory of the electromagnetic field*. Wipf and Stock Publishers.

Mayer, B. and Kylling, A. (2005). Technical note: The libradtran software package for radiative transfer calculations - description and examples of use. *Atmospheric Chemistry and Physics*, 5(7):1855–1877.

McDonald, J. E. (1963). The saturation adjustment in numerical modelling of fog. *Journal of the Atmospheric Sciences*, 20(5):476–478.

Mellado, J. P. (2017). Cloud-top entrainment in stratocumulus clouds. *Annual Review of Fluid Mechanics*, 49:145–169.

Mie, G. (1908). Beitraege zur optik trueber medien, speziell kolloidaler metalloesungen. *Annalen der Physik*, 330(3):377–445.

Moeng, C.-H., Cotton, W. R., Bretherton, C., Chlond, A., Khairoutdinov, M., Krueger, S., Lewellen, W. S., MacVean, M. K., Pasquier, J. R. M., Rand, H. A., Siebesma, A. P., Stevens, B., and Sykes, R. I. (1996). Simulation of a stratocumulus-topped planetary boundary layer: Intercomparison among different numerical codes. *Bulletin of the American Meteorological Society*, 77(2):261–278.

Moeng, C.-H. and Wyngaard, J. C. (1988). Spectral analysis of large-eddy simulations of the convective boundary layer. *Journal of the Atmospheric Sciences*, 45(23):3573–3587.

Ouro, P. (2017). *Large-Eddy Simulation of Tidal Turbines*.

Pinsky, M. and Khain, A. (1997). Turbulence effects on droplet growth and size distribution in clouds—a review. *Journal of Aerosol Science*, 28(7):1177 – 1214.

Planck, M. (1901). On the law of distribution of energy in the normal spectrum. *Annalen der physik*, 4(553):1.

Raasch, S. and Schröter, M. (2001). Palm a large-eddy simulation model performing on massively parallel computers. *Meteorologische Zeitschrift*, 10(5):363–372.

Rasmussen, R. M., Geresdi, I., Thompson, G., Manning, K., and Karplus, E. (2002). Freezing drizzle formation in stably stratified layer clouds: The role of radiative cooling of cloud droplets, cloud condensation nuclei, and ice initiation. *Journal of the Atmospheric Sciences*, 59(4):837–860.

Rauber, R. M., Stevens, B., Ochs, H. T., Knight, C., Albrecht, B. A., Blyth, A. M., Fairall, C. W., Jensen, J. B., Lasher-Trapp, S. G., Mayol-Bracero, O. L., Vali, G., Anderson, J. R., Baker, B. A., Bandy, A. R., Burnet, E., Brenguier, J.-L., Brewer, W. A., Brown, P. R. A., Chuang, R., Cotton, W. R., Di Girolamo, L., Geerts, B., Gerber, H., Göke, S., Gomes, L., Heikes, B. G., Hudson, J. G., Kollias, P., Lawson, R. R., Krueger, S. K., Lenschow, D. H., Nuijens, L., O'Sullivan, D. W., Rilling, R. A., Rogers, D. C., Siebesma, A. P., Snodgrass, E., Stith, J. L., Thornton, D. C., Tucker, S., Twohy, C. H., and Zuidema, P. (2007). Rain in shallow cumulus over the ocean: The rico campaign. *Bulletin of the American Meteorological Society*, 88(12):1912–1928.

Riechelmann, T., Noh, Y., and Raasch, S. (2012). A new method for large-eddy simulations of clouds with lagrangian droplets including the effects of turbulent collision. *New Journal of Physics*, 14(6):065008.

Roach, W. T. (1976). On the effect of radiative exchange on the growth by condensation of a cloud or fog droplet. *Quarterly Journal of the Royal Meteorological Society*, 102(432):361–372.

Roach, W. T., Brown, R., Caughey, S. J., Garland, J. A., and Readings, C. J. (1976). The physics of radiation fog: I – a field study. *Quarterly Journal of the Royal Meteorological Society*, 102(432):313–333.

Rogers, R. and Yau, M. (1996). *A Short Course in Cloud Physics, Third Edition*. Eslevier.

Schumann, U. (1975). Subgrid scale model for finite difference simulations of turbulent flows in plane channels and annuli. *Journal of Computational Physics*, 18:376–404.

Schumann, U. (1991). Subgrid length-scales for large-eddy simulation of stratified turbulence. *Theoretical and Computational Fluid Dynamics*, 2(5):279–290.

Schwenkel, J., Hoffmann, F., and Raasch, S. (2018). Improving collisional growth in lagrangian cloud models: development and verification of a new splitting algorithm. *Geoscientific Model Development*, 11(9):3929–3944.

Shima, S., Kusano, K., Kawano, A., Sugiyama, T., and Kawahara, S. (2009). The super-droplet method for the numerical simulation of clouds and precipitation: a particle-based and probabilistic microphysics model coupled with a non-hydrostatic model. *Quarterly Journal of the Royal Meteorological Society*, 135(642):1307–1320.

Squires, P. (1952). The Growth of Cloud Drops by Condensation. II. The Formation of Large Cloud Drops. *Australian Journal of Scientific Research A Physical Sciences*, 5:473.

Stevens, B., Moeng, C.-H., Ackerman, A. S., Bretherton, C. S., Chlond, A., de Roode, S., Edwards, J., Golaz, J.-C., Jiang, H., Khairoutdinov, M., Kirkpatrick, M. P., Lewellen, D. C., Lock, A., Müller, F., Stevens, D. E., Whelan, E., and Zhu, P. (2005). Evaluation of large-eddy simulations via observations of nocturnal marine stratocumulus. *Monthly Weather Review*, 133(6):1443–1462.

Sölch, I. and Kärcher, B. (2010). A large-eddy model for cirrus clouds with explicit aerosol and ice microphysics and lagrangian ice particle tracking. *Quarterly Journal of the Royal Meteorological Society*, 136(653):2074–2093.

Vaillancourt, P. A., Yau, M. K., Bartello, P., and Grabowski, W. W. (2002). Microscopic approach to cloud droplet growth by condensation. part ii: Turbulence, clustering, and condensational growth. *Journal of the Atmospheric Sciences*, 59(24):3421–3435.

Wang, L.-P. and Grabowski, W. W. (2009). The role of air turbulence in warm rain initiation. *Atmospheric Science Letters*, 10(1):1–8.

Warner, J. (1969a). The microstructure of cumulus cloud. part i. general features of the droplet spectrum. *Journal of the Atmospheric Sciences*, 26(5):1049–1059.

Warner, J. (1969b). The microstructure of cumulus cloud. part ii. the effect on droplet size distribution of the cloud nucleus spectrum and updraft velocity. *Journal of the Atmospheric Sciences*, 26(6):1272–1282.

WEF (2019). The global risk report.

Yin, Y., Levin, Z., Reisin, T. G., and Tzivion, S. (2000). The effects of giant cloud condensation nuclei on the development of precipitation in convective clouds — a numerical study. *Atmospheric Research*, 53(1):91 – 116.

Acknowledgement

I would like to thank my love and best friend Katja for always being there for me, no matter what.

Furthermore, I would like to thank the people at the Meteorological Institut for doing such great work.

Finally, I would like to thank Bernhard Mayer for giving me this great opportunity.